

This is an Open Access document downloaded from ORCA, Cardiff University's institutional repository: <https://orca.cardiff.ac.uk/id/eprint/142171/>

This is the author's version of a work that was submitted to / accepted for publication.

Citation for final published version:

Chi Fru, Ernest , Bankole, Olabode, Chraik, Ibtissam, Youb, Nassreddine, Millet, Marc-Alban , Rouxel, Olivier, El Albani, Abderrazzak and Bouougr, El Hafid 2021. Early Neoproterozoic oxygenation dynamics along the northern margin of the West African Craton, Anti-Atlas Mountains, Morocco. Chemical Geology 581 , 120404. 10.1016/j.chemgeo.2021.120404

Publishers page: <http://dx.doi.org/10.1016/j.chemgeo.2021.120404>

Please note:

Changes made as a result of publishing processes such as copy-editing, formatting and page numbers may not be reflected in this version. For the definitive version of this publication, please refer to the published source. You are advised to consult the publisher's version if you wish to cite this paper.

This version is being made available in accordance with publisher policies. See <http://orca.cf.ac.uk/policies.html> for usage policies. Copyright and moral rights for publications made available in ORCA are retained by the copyright holders.



1 Early Neoproterozoic oxygenation dynamics along the northern margin  
2 of the West African Craton, Anti-Atlas Mountains, Morocco

3  
4 Ernest Chi Fru<sup>a\*</sup>, Olabode Bankole<sup>b</sup>, Ibtissam Chraiki<sup>c</sup>, Nassrddine Youbi<sup>c</sup>,  
5 Marc-Alban Millet<sup>a</sup>, Olivier Rouxel<sup>d</sup>, Abderrazzak El Albani<sup>b</sup>, El Hafid  
6 Bouougri<sup>c</sup>

7  
8 <sup>a</sup>School of Earth and Ocean Sciences, Centre for Geobiology and  
9 Geochemistry, Cardiff University, Cardiff CF10 3AT, Wales, UK

10 <sup>b</sup>University of Poitiers, CNRS IC2MP UMR 7285, Poitiers, France.

11 <sup>c</sup>DLGR, Department of Geology, Faculty of Sciences-Semlalia, Cadi Ayyad  
12 University, Marrakesh, Morocco.

13 <sup>d</sup>Unité de Géosciences Marines, IFREMER, Z.I. Pointe du diable, BP 70, 29280  
14 Plouzané, France.

15  
16  
17  
18 \*ChiFruE@Cardiff.ac.uk  
19  
20  
21  
22  
23  
24  
25  
26  
27  
28  
29  
30  
31  
32  
33



## ABSTRACT

Emerging evidence suggests widespread ferruginous marine conditions promoted global seawater phosphate depletion and the maintenance of a low oxygen world at the start of the Neoproterozoic Era. However, the large-scale deposition of marine sedimentary Fe formations, as observed in the Paleoproterozoic, is rare in the early Neoproterozoic Era. We show that at the start of the Neoproterozoic, tidal flat and shallow marine environments along the northern passive margin of the West African Craton (WAC) were fully oxygenated and low in reactive Fe content, until an abrupt and prolonged episode of deep-sea hydrothermal activity overwhelmed the WAC margin with strongly reducing Fe-rich hydrothermal fluids. This unique incident is recorded in meter-thick and kilometer-wide shallow marine siliciclastic platform rocks estimated to be ~883 Ma old and containing average bulk Fe content >22 wt.% in the Wanimzi Formation in the Moroccan Anti-Atlas Mountains. The abrupt and conformable contact of the Fe-rich succession with the Fe-poor lower and upper transition boundaries, together with geochemical data, suggest rapid initiation and termination of seawater fertilization by the hydrothermal fluids that formed the unmetamorphosed hematite-rich ironstones. Rare Earth Element (REE) and Fe-based redox reconstruction point to an aftermath coincident with a return to shallow siliciclastic marine habitats characterized by a low reactive Fe content and negligible hydrothermal intrusion, where aerobic microbial communities flourished in well-oxygenated waters. We propose that the early Neoproterozoic tectonic initiation of the breakup of the supercontinent Rodinia supplied large volumes of deep sea hydrothermal Fe, trace metals, and toxic metalloids like arsenic to shallow marine habitats along the WAC, resulting in rapid seawater deoxygenation.

Keywords: Siliciclastic iron formation; Tonian period; Ironstones; Hydrothermal activity; Rodinia supercontinent.

## 1. Introduction

It is widely accepted that Precambrian seawater Fe concentrations exerted a major control on early ocean chemistry, oxygenation of the atmosphere, climate, and the evolution of global biogeochemical cycles (e.g., Frei et al., 2008; Planavsky et al., 2010; Heimann et al., 2010; Halverson et al., 2011; Lyons et al., 2014; Brock et al., 2017; Hoffman et al., 2017; Reinhard et al., 2017; Song et al., 2017; Guilbaud et al., 2020; Heard and Dauphas, 2020). For instance, Fe mineral precipitation modulates the concentration of dissolved species in seawater, including macro- and micro-nutrient content (e.g., Dymek and Klein, 1988; Konhauser et al., 2002; Fischer and Knoll, 2009; Zegeye et al., 2012; Chi Fru et al., 2012, 2013, 2015a-b, 2016a-b; Large et al., 2015; Hugaard et al., 2016; Hoffman et al., 2017; Konhauser et al., 2017; Hemmingsson et al., 2018; Keyser et al., 2018; Mukherjee et al., 2019; Robbins et al., 2019; Heard and Dauphas, 2020).

As a consequence, throughout the Archean and for most of the Paleoproterozoic eon, considerable quantities of ferrous Fe oxidized out of seawater to form sizable Algoma type Fe formations containing >15 wt.% Fe in deep sea Archean volcanic centers and Superior type banded iron formations (BIF) on passive Paleoproterozoic sea margins (see Bekker et al., 2010 for a review). A systematic reduction in the deposition of Fe formations has been linked to the permanent appearance of free molecular oxygen in the atmosphere during the so called Great Oxidation Event (GOE) (Bekker et al., 2010; Lyons et al., 2014). This is thought to be the result of enhanced biotic and abiotic oxidation of soluble ferrous Fe to insoluble ferric Fe minerals using molecular oxygen as an efficient electron acceptor (Emerson et al., 2010; Chi Fru et al., 2012), accelerated precipitation of pyrite because of the intensification of microbial sulfate reduction as a result of GOE-induced rise in seawater sulfate concentrations and progressive weakening of hydrothermal activity through Earth history (e.g., Canfield, 1998; Bekker et al., 2010; Poulton and Canfield, 2011; Lyons et al., 2014).

Following the GOE, the oceanic redox structure differentiated into oxygen-rich shallow surface waters, mid-depth continental margin sulfide-rich (euxinic) waters, and deep ferruginous waters (e.g., Canfield, 1998; Rouxel et al., 2005; Poulton et al., 2011; Reinhard et al., 2013; Lyons et al., 2014; Dauphas et al.,

2016; Mukherjee et al., 2019). Pyrite precipitated in the euxinic settings, while the upwelling and the mixing of the deep ocean ferruginous waters with the oxygenated chemocline and surface waters, shuttled silica and ferric Fe to the sea floor (Canfield, 1998; Fischer and Knoll, 2009; Poulton and Canfield, 2011; Reinhard et al., 2013).

Because of the high affinity of both pyrite and ferric Fe for trace elements, these important Fe minerals controlled the mobility and availability of trace elements in seawater through co-precipitation and adsorption reactions (e.g., Reinhard et al., 2013; Large et al., 2015; Mukherjee et al., 2019; Robbins et al., 2019). For example, the enrichment of Mo and As in euxinic marine sediments correlate with pyrite accumulation (Reinhard et al., 2013; Chi Fru et al., 2019) while rapid trace element removal from seawater by ferric Fe is observed in oxygenated environments where biological and abiological oxidation of ferrous Fe with oxygen occurs (Konhauser et al., 2002; Chi Fru et al., 2012; Emerson et al., 2010) and in anoxic settings where phototrophic oxidation of ferrous Fe is prevalent (Thompson et al., 2019).

The ferric Fe particles can be reduced in the deep anoxic ocean and sediments by the dissimilatory Fe-reducing bacteria (DIR) using organic carbon and nitrate (Weber et al., 2006) and/or by sulfide (Poulton and Canfield, 2011) to recycle ferrous Fe and bound trace elements and nutrients back to seawater (e.g., Guilbaud et al., 2020). Consequently, Fe carbonates in ancient Fe formations are thought to record the respiratory activities of the DIR (e.g., Severmann et al., 2008; Heimann et al., 2010; Craddock and Dauphas, 2011). Because of the strong coupling between the oxidation state of Fe and seawater redox, the speciation of Fe mineral phases in primary marine chemical sediments has gained widespread application in the reconstruction of past seawater redox state from sedimentary rocks (Poulton and Canfield, 2005; Poulton et al., 2011; Sperling et al., 2015; Raiswell et al., 2018).

This study describes an early Neoproterozoic siliciclastic Fe formation deposited as part of a shallow marine environment along the northern margin of the West African Craton (WAC) in the Anti-Atlas belt of Morocco. We unravel how Fe was sourced from a deep-marine oxygen-starved, hydrothermally active ocean and mixed with oxygenated coastal shoreline waters to form the siliciclastic Wanimzi ironstones. We propose that this incident is linked to

136 tectonic events that initiated the breakup of the supercontinent Rodinia and that  
137 this event had severe consequences for life and the oxygenation of affected  
138 shallow seawater masses along the WAC coast.

## 140 **2. Geological setting**

141 The Proterozoic basement of the Anti-Atlas constitutes the northern margin of  
142 the WAC. It is overprinted by Pan-African-Cadomian events and bounded by  
143 two tectonic fault zones, represented by the Anti-Atlas major Fault (AAMF) and  
144 the High-Atlas South Fault (e.g. Leblanc & Lancelot, 1980; Saquaque et al.,  
145 1989; Bouougri, 2003; Ennih & Liegeois, 2008). The AAMF (e.g. Choubert,  
146 1947; Leblanc and Lancelot, 1980; Saquaque et al., 1989) is a tectonic  
147 boundary separating the cratonic margin to the south from the ~770-700 Ma  
148 island arc-related terrane to the north that was accreted onto the margin during  
149 Pan-African collisional events ~663-640 Ma (e.g. Leblanc et Lancelot, 1980;  
150 Saquaque et al., 1989; Bouougri, 2003; El Hadi et al., 2010; Thomas et al, 2004;  
151 Inglis et al., 2005; Triantafyllou et al., 2016; Fig. 1a).

152 The post-Eburnean craton margin strata of the Anti-Atlas, comprising of  
153 a volcano-sedimentary succession up to 2 km thick spanning the Upper  
154 Paleoproterozoic to Early Neoproterozoic time, crops out along the AAMF (Figs  
155 1b). Based on radiometric data, the successions unconformably overlying the  
156 Eburnean basement (~2000-1800 Ma) is subdivided according to new  
157 radiometric data into three main tectono-sedimentary sequences spanning the  
158 Columbia and Rodinia supercontinent cycles (Letsch, 2018; Bouougri et al.,  
159 2020). The complete section is well exposed in the central part of the Anti-Atlas  
160 along the AAMF, with a tripartite subdivision into a Lower sedimentary  
161 ensemble, a Middle volcanic unit and an Upper sedimentary sequence  
162 (Bouougri and Saquaque, 2004). In previous works, and considering mainly the  
163 Pan-African tectonic features and the lack of any evidence for a  
164 Mesoproterozoic Grenvillian tectono-thermal event in the Anti-Atlas and in the  
165 WAC, the whole succession was assigned to the Neoproterozoic and to the  
166 Pan-African rifted-margin of the Anti-Atlas (Leblanc et Lancelot, 1980;  
167 Saquaque et al., 1989; Leblanc and Moussine-Pouchkine, 1994), formally  
168 named the Tizi n'Taghatine Group in its stratotype area (Bouougri and  
169 Saquaque, 2004). However, revised stratigraphic framework as well as new



radiometric ages obtained from interbedded volcanic occurrences, mafic sills cross-cutting the lowermost part of the succession, and U-Pb ages from detrital zircons, provide evidence for two tectono-stratigraphic cycles of Upper Paleoproterozoic to possibly Mesoproterozoic pre-Pan-African and the Neoproterozoic Pan-African cycle (Letsch, 2018; Bouougri et al., 2020). The first cycle extends from the bottom to the Tasserda, Taghdout and Oumoula Formations. This is succeeded by the Neoproterozoic, subdivided into Tonian strata (~883 Ma) and the ~700 Ma Cryogenian Bleïda Formation, interpreted as rift-related and pre-collisional foreland basin successions, respectively (Bouougri et al., 2020).

The 883 Ma age is obtained from pyroclastic material lying directly above the Imi n-Tizi Formation (Bouougri et al, 2020; Fig. 2a). Gradual emergence of volcanic activity and transition into the deposition of the mainly volcanic rocks in the Tachdamt Formation from the underlying Wanimzi Formation is indicated by the placement of interbedded pyroclastic flow beds in the underlying platform deposits. This kind of transition as well as evidence of feeder dykes cutting through the platform deposits, collectively suggest a Tonian age close to ~883 Ma. Moreover, by considering the maximum 500 m thickness of the platform deposits, low sedimentation rates of  $0.06 \text{ cm year}^{-1}$ , the lack of evidence for a time gap, and a high rate of compaction, deposition of the entire succession could not have exceeded a duration of ~5 million years (Bouougri et al., 2020). The platform deposits, including the Wanimzi Formation, are part of the start of a global Neoproterozoic cycle that triggered the breakup of the Rodinia supercontinent ~900 Ma (Bouougri et al., 2020).

In the studied area along the southern margin of the Siroua Inlier (Fig. 1b), the Pan-African rift-related succession of Tonian age is well exposed in the Agoumy section (Fig. 1b). The pre-rift sedimentary strata (Fig. 2a) in ascending order, include the Ifarkhs n'Tirsal, Wanimzi, Tamgarda, Agoumy and Imi n-Tizi Formations (Bouougri and Saquaque, 2004). This mixed siliciclastic-carbonate succession of shallow marine origin, is overlain by the syn-rift volcanic Tachdamt Formation. A new minimum age of ~883 Ma has been recently suggested for the pre-rift shallow marine mixed siliciclastic-carbonate deposits (Bouougri et al., 2020). Transition from the above shallow platform marine siliciclastic deposits to the overlying volcanic Tachdamt

Formation shows no evidence of an erosional unconformity or time gap. Instead, a sharp contact characterized by remnants of pyroclastic occurrences atop of the Imi n'Tizi Formation, indicate stratigraphic continuity (Bouougri et al., 2020). The age of the platform deposit is thus considered very close to ~883 Ma and not older than ~900 Ma even when low sedimentation rates are considered for the platform wedge estimated to be ~500 m thick in the studied section. These shallow near-continental margin sedimentary rocks are thought to record a stable craton margin, which underwent major rifting and magmatic events that led to the breakup of Rodinia (Bouougri et al., 2020).

The lithology of the basal Paleoproterozoic Taghdout Formation in the studied section is dominated by carbonates and mixed siliciclastic-carbonate rocks, while the early Neoproterozoic Wanimzi and Imi n'Tizi formations present fine-grained siliciclastic and heterolithic rhythmic beds, rich in sedimentary structures interpreted as reflecting a shallow shelf setting and the activities of ancient microbial mats (e.g., Bouougri and Saquaque, 2004; Bouougri and Porada, 2002). The heterolithic beds contain biolaminitic thin multilayered packages that formed on sand and as cm-thick planar laminated layers frequently disturbed by shrinkage cracks. A variety of mat-related structures previously identified in these heterolithic layers, in both the Wanimzi and Imi n'Tizi Formations, tend to be associated with reticulate patterns and microbial shrinkage cracks (Bouougri and Porada, 2002).

The studied Fe oxide-bearing Wanimzi Formation is a ~120 m thick siliciclastic unit dominated by heterolithic deposits showing an overall coarsening and shallowing upward trend (Fig. 2). Sedimentary features indicate a depositional setting in a storm and wave dominated shallow marine ramp (Bouougri and Saquaque, 2004). According to sand-mud ratio and facies features, three parts can be distinguished within this formation. These consist of (i) a lower mudstone and fine grained siltstone deposited below storm wave base (SWB), (ii) a middle heterolithic deposit including beds with hummocky cross stratification (HCS) indicating deposition above SWB in an outer offshore transition zone, and (iii) an Upper sand dominated sequence with amalgamated sandstone beds containing HCS and swaley cross-stratification (SCS), indicating deposition in the inner part of the offshore transition to a lower

shoreface zone. The middle part contrasts clearly with other deposits and shows a dense red color related to Fe enrichment.

### **3. Methods**

#### *3.1. Sampling and sample preparation*

In the Agoumy area (Fig. 2b), fresh unweathered samples were collected at two key stratigraphic units from the Wanimzi Formation, with focus on the undescribed Wanimzi ironstones (Fig. 3) and reference microbial laminated samples from the overlying Imi n'Tizi Formations (Fig. 4). The Wanimzi Formation was sampled at 5-10 cm intervals at 30°30'0.58"N, 7°41'51.47"W and 30°29'57.84"N, 7°41'48.08"W (Fig. 3a-b&d). These well-exposed outcrops (Fig. 3a-d) can be seen using satellite imagery to be laterally exposed for at least ~4 km.

Three reference carbonate samples were also collected from outcrops of the underlying older Paleoproterozoic (>1640 Ma) Eburnean basement at the Taghdout Formation and four from the well preserved stromatolite-rich siliciclastic rocks of the uppermost Imi n'Tizi Formation (Fig. 4a) described in Bouougri et al. (2002, 2007). The Taghdout carbonates and the Imi n'Tizi silicate rocks were sampled to provide Fe-poor references for comparison with the Fe-rich lithologies and to enable the interpretation of the transitional events that led to the onset and termination of the deposition of the Wanimzi ironstones. Representative stromatolitic units sampled from the Imi n'Tizi Formation consist of twisted biolaminations (S1), horizontal beds with no laminations (S2), consistent millimeter-thick bands (S3) and flat visible horizontal biolaminations (S4). Samples were collected for redox reconstruction, thin-section petrography, mineralogy, trace element (TE) and rare earth element (REE) analyses, C and Fe isotope measurements.

#### *3.2. Petrography and mineralogy*

Before analysis, samples were shaved with a saw and exposed surfaces in contact with the atmosphere discarded. Polished thin-sections were prepared using standard rock-polishing laboratory procedures in the School of Earth and Ocean Sciences, Cardiff University. Portions of identical shaved thin-sectioned rock pieces were pulverized to a fine powder for geochemical analysis using a

jaw crusher and by disc milling. Polished thin-sections for representative samples were examined for mineralogy and textural relationships under reflected and transmitted light microscopy using a Nikon ECLIPSE E600 POL microscope equipped with a Nikon Digital Sight DS-U1 camera at the University of Poitiers, France. Whole rock X-ray diffraction (XRD) mineral analyses were performed on powdered samples with a Bruker D8 ADVANCE diffractometer using CuK $\alpha$  radiation operating at 40 Kv and 40 mA and step size of 0.025/s between 2-65 °2 $\theta$  angular ranges.

### *3.3. Trace and Rare Earth Element analysis*

Bureau Veritas® (Vancouver, Canada) procedure code LF100-EXT was used to measure the concentration of 45 TEs and REEs in 0.2 g powdered samples. The samples were digested by lithium borate (LiBO<sub>2</sub>/Li<sub>2</sub>B<sub>4</sub>O<sub>7</sub>) fusion and solutions analyzed by Inductively Coupled-Mass Spectrometry (ICP-MS). Lithium borate fusion is an aggressive chemical digestion process that effectively dissolves most refractory and resistant mineral phases, ensuring complete dissolution of powdered samples. Total Fe was measured by UV-Vis spectrometry using Stokey's ferrozine test as part of the Fe speciation protocol described in Poulton and Canfield (2004) and in section 3.4. Post Archean Australian Shale (PAAS) was used for REE+Y normalization (McLennan, 1989) and REE+Y anomalies are calculated as described previously (Bau and Dulski et al., 1996; Planavsky et al., 2010).

### *3.4. Fe-based redox reconstruction*

Redox reconstruction was obtained by application of the widely used Fe-based methodology for the reconstruction of bottom water redox conditions in modern and ancient siliciclastic and carbonate depositional environments habitats (Poulton and Canfield, 2005; Clarkson et al., 2014; Raiswell et al., 2018). This method allows the allocation of the Fe mineral phases into seven operational pools, divided into highly reactive ferric Fe and pyrite Fe phases (Fe<sub>HR</sub>), poorly reactive sheet silicate Fe and Fe in unreactive silicate (Poulton and Canfield, 2005). Samples were screened to contain >0.5 wt% Fe – a minimum threshold recommended to correct for variations in sedimentary Fe concentrations and



dilution by detrital materials (Poulton and Canfield, 2005; Clarkson et al., 2014; Raiswell et al., 2018).

### 3.5. Carbon and oxygen isotopes

Organic carbon ( $C_{org}$ ), carbonate carbon ( $C_{carbonate}$ ) and carbonate O isotopes ( $O_{carbonate}$ ) were co-measured on a Thermo Delta V Advantage mass spectrometer. The instrument is connected to a Thermo gasbench II for headspace sampling ( $C_{carbonates}$ ), while a Thermo Flash EA with ConFlo III allows for the combustion of organic samples. The  $\delta^{13}C$  and  $\delta^{18}O$  are reported in the delta notation using the Vienna-Pee Dee Belemnite (VPDB) standard. The  $C_{org}$  and inorganic carbon content was estimated from a regression equation for signal intensity against the amount that was established for standard materials with known composition. Powdered samples were weighed into septum vials flushed with helium, acidified with 99 % orthophosphoric acid, and left to react for 24 hours at 60 °C to ensure complete reaction of dolomite. The long-term precision of an in-house Carrara marble standard has been estimated to 0.05 ‰ for both  $\delta^{18}O$  and  $\delta^{13}C$  (1sd). To eliminate inorganic carbon, prior to measuring  $C_{org}$  concentrations and  $\delta^{13}C_{org}$  isotopic distribution, samples were acidified in 10 % HCl and reaction left for two days. Residual acids was removed by washing the treated samples three times with ultrapure double distilled water. Sixty to eighty mg of samples were analysed for  $C_{org}$ . The total  $C_{org}$  analysed was as low as 10 µg because of low  $C_{org}$  content. Three standards were used to calibrate the accuracy of these small sample concentrations: IAEA-CH6 [ $\delta^{13}C=-10.449$  ‰], IAEA-600 [ $\delta^{13}C=-27.771$  ‰], and an in-house caffeine [ $\delta^{13}C=-33.30$  ‰] and were dissolved in de-ionised water to improve homogeneity and to allow accurate dosing of small aliquots using a micropipette. Results for IAEA-CH6 and the in-house caffeine were used to estimate a correction function for sample size and size-dependent 2-point normalisation, which was applied to IAEA-600 as the independent standard. The resultant precision is dependent on sample size. The long-term precision for  $\delta^{13}C$  was 0.09 ‰ (1sd) for routine samples containing  $\geq 100$  µg C. However, the standard deviation increases with decreasing sample size, to 0.38 ‰ for aliquots with 10 - 30 µg C as measured for the present study (IAEA-600, N=15).

### 3.6. *Fe isotopes*

Samples were dissolved by standard acid digestion using concentrated HF, HNO<sub>3</sub>, and hotplates in acid washed Teflon beakers, and purified through polypropylene pipette tips chromatographic columns containing a 500 µl AG1-X4 anion exchange resin (Millet et al., 2012). Fe isotopes were measured at IFREMER, France, on a Thermo Scientific Neptune MC-ICP-MS set on medium or high-resolution mode as described in Rouxel et al. (2018). Analysis included sample-standard bracketing and internal normalization using Ni with a known isotope ratio and an internal precision of 0.04-0.09‰ (2sd) for 100 ng of recovered Fe (Rouxel et al., 2018). Data are reported as  $\delta^{56}\text{Fe}$  and  $\delta^{57}\text{Fe}$  ratios in parts per thousand deviations from the IRMM-014 standard. More than 50 replicates of the Hawaiian basalt internal standards BHVO-1 and BHVO-2 using this method yielded average  $\delta^{56}\text{Fe}$  values of  $0.09 \pm 0.07\text{‰}$  (Rouxel, 2018).

## 4. Results

### 4.1. *Field observations and sedimentary features*

The Fe-rich layers in the Wanimzi Formation often occur as oxidized red to purple cm-thick beds alternating with heterolithes and thin storm beds with HCS (Fig. 3a-c). In the lower part of Wanimzi Formation (Fig. 2b, 3d), several isolated decimeter-thick storm beds of Fe-rich sandstones were observed, some of which preserve artisanal digging trenches running parallel to the mineralized layers. The heterolithic beds are composed of silt, sand, and microbial biolaminated layers similar to the overlying Fe-poor Imi n'Tizi Formation (Fig. 4), indicating deposition of both successions above a storm wave base, in a shallow marine setting. Well-developed and previously described siliciclastic stromatolites, marked by prominent flat to large domal shaped morphologies (Bouougri and Porada, 2011), appear in the Imi n'Tizi fine-grained siliciclastic Formation (Fig 4g-h).

Several mat-related structures dominated by Kinneyia-type wrinkled structures, ripples, spindle-shaped and sinusoidal cracks, and sandstone chips were recognized within the heterolithic facies in the Wanimzi and Imi n'Tizi Formations (Fig. 4). The Kinneyia-type wrinkled structures in both formations occur on the upper surfaces of sandstone beds, and are characterized by mm-thick structures twisted into flat-top crests separated by round bottom troughs

and pits that are comparable in size (Fig. 4c). Ripple marks on the top of several sandstone beds (Fig. 4a-b) are colonized and stabilized by thin or thick microbial mat layers (Bouougri and Porada, 2002). Spindle-shaped and sinusoidal cracks (Fig. 4d), equally abundant in the Wanimzi and Imi n'Tizi Formations, were associated with mm-laminated argillite, sandstones and silty sandstones that are sometimes formed on the upper surfaces of sandstone beds free of mud trappings (Fig. 4e). These structures present a great variety in size and shape, including sub-circular, crescent-shaped and sinusoidal cracks observed on the upper bedding surfaces of fine-grained quartzite and siltstone layers. Structures related to microbial mat colonization and upper veneer stabilization of sand bedding surfaces occur as current deformation features and flat microbial sand clasts (Fig. 4e-f). The association of these features with large ripple slabs made up of sandstone confirms the deposition of the Imi n'Tizi Formation in a shallow marine environment. Horizons with sandstone chips and characterized by well-rounded to ellipsoidal flat-shaped features appear abundantly in the basal units of the medium to fine-grained quartzite layers.

Beginning with the microbial mat-rich Imi n'Tizi Formation that marks the top of the studied package, the layers are composed of two distinct sediment types, typified by sharp coarse and fine-sediment layers (Fig. 5a-b). The siliciclastic stromatolites consist of mat-growth structures made up predominantly of moderately compacted and well-sorted quartz-dominated silty-sandstone layers alternating thin mud/shale laminae, consisting of micas and dominated by muscovite and illite (Fig. 5a-b; Table 1; Appendix A-B). The quartz coarse grains are detrital, while the fine-grained layers have been suggested to be fossil remains of ancient microbial mat layers according to several mat-related features preserved on bedding surfaces (Bouougri and Porada, 2002). This simple repetitive architecture of coarse siliciclastic layers alternating with thinner fine-grained siliciclastic beds was observed on all sections investigated. Well-sorted, rounded, angular to sub-angular, silt-sand-sized quartz grains cemented in an Fe-rich matrix, are a unique characteristic and distinguishing hallmark of the Wanimzi Formation (Fig. 5c-f).

#### *4.2. Mineralogical characterization*

Thin section analysis of the Fe-rich lithologies in the Wanimzi Formation (Fig. 5) is consistent with the mainly siliciclastic composition of near continental margin Neoproterozoic deposits in the Moroccan Anti-Atlas Mountains. Although hematite and quartz are present in all lithologies, their predominant character is restricted to the Wanimzi ironstones (Appendix C-E & H-J), while quartz predominates the stromatolitic lithologies of the Imi n'Tizi Formation (Appendix A-N). The Taghdout Formation consists primarily of ooid-peloid grainstone cemented in a mainly quartz-carbonate matrix composed of calcite, dolomite, minute hematite concentrations, feldspars, and illite/mica clays (Fig. 5g-i; Appendix F,G, L). The ooids are made of microcrystalline calcitic laminae with radially arranged calcite crystals and dark Fe enriched thinner laminae. Relics of oolites were identified showing the dissolution of the original structure and its replacement by drusy calcite crystals, indicating a neomorphism process (Fig. 5g-i; Appendix F,G, L).

#### *4.3. Trace element (TE) geochemistry*

Out of the 45 elements analyzed, Fe is the most enriched across all lithologies (Fig. 6; Table 2). Co, V, U, As, Sb are pronounced in the ironstones which record varying Cu enrichment and Mo depletion, compared to average concentrations in the siliciclastic stromatolitic and carbonate-rich rocks (Table 2; Fig. 6a-d). Cd was below the detection limit of 0.1 ppm in both the siliciclastic stromatolitic and hematite-rich rocks while averaging 0.37 ppm in the underlying carbonate-rich facies. Average As concentrations in the Wanimzi ironstones were 18.2, 8.8, and 19.4 times in excess of those measured in the overlying siliciclastic facies, the underlying siliciclastic carbonates and average upper continental crust values, respectively. These values were much lower for the siliciclastic and carbonate lithologies relative to the upper continental crust by a factor of 1.1 and 2.2, respectively. As and Sb expressed similar curves in all samples (Fig. 6a&d). Fe concentrations of up to 61.7%, averaging 22.4% (n=18) (Table 2) qualify the Wanimzi ironstones as an Fe formation based on the definition of a chemical sedimentary sequence containing >15% Fe (see for example Bekker et al., 2010).

The average Fe content in the ironstone lithologies are up to a factor of 34, 21, and 64 in excess of the average concentrations in the representative



samples from the reference siliciclastic stromatolite-rich Imi n'Tizi Formation, the Taghdout siliciclastic carbonate facies, and the upper continental crust average reported by McLennan (2001), respectively (Table 2). Moreover, Fe and quartz are often inversely related in the Fe-rich rocks (Fig. 6e), but Fe remained generally below 1.0 wt.% in the stromatolitic and carbonate-rich layers. Zn/Co ratios largely decreased from the carbonates through to the overlying Neoproterozoic siliciclastic stromatolitic succession (Fig. 6f). Mo/W ratios are generally low (Fig. 6g). Th/U ratios are relatively low in the Fe-rich sequences compared to the reference overlying and underlying Fe-poor samples (Fig. 6h).

#### 4.4. Carbon content, and carbon and oxygen isotope distribution

C<sub>org</sub> concentrations are generally low, ranging from 0.01 to 0.06 wt% across the sequence, with the highest values associated with the Taghdout carbonates (Fig. 6i; Table 3). The average value of C<sub>org</sub> is 0.02±0.0008 wt%, 0.05±0.012 wt%, and 0.01±0.004 wt% in the ironstones, carbonates, and stromatolitic mats, respectively. The isotopic distribution of  $\delta^{13}\text{C}_{\text{org}}$  range from -33.03‰ to -22.93‰, averaging -29.8±2.22‰, -27.42±0.99‰, and -29.49±1.85‰ in the Fe-rich, the carbonates, and the stromatolitic lithologies, respectively. The lowest and highest single  $\delta^{13}\text{C}_{\text{org}}$  values are recorded in the Fe-rich rocks (Fig. 6j; Table 3), while the rare occurrence of carbonates in the Fe-rich rocks is consistent with XRD data, except for sample AG14 with a carbonate concentration of 0.21 wt% and associated  $\delta^{13}\text{C}_{\text{carbonate}}$  and  $\delta^{18}\text{O}_{\text{carbonate}}$  values of -8.72‰ and -12.79‰, respectively, (Table 3). The carbonate-rich lithologies have high carbonate concentrations between 50 and 75 wt%, with measured  $\delta^{13}\text{C}_{\text{carbonates}}$  and  $\delta^{18}\text{O}_{\text{carbonate}}$  values ranging from -0.77‰ to 0.11‰ (average = -0.28±0.45‰) and -14.5 to -13.28‰ (average = -14.03±0.65‰), respectively (Table 3).

#### 4.5. Rare Earth Elements (REEs)

Post Archean Australian Shale (PAAS) normalized REE patterns are generally similar for the siliciclastic biolaminites and Taghdout carbonate lithologies, but largely different for the Wanimzi ironstones (Fig. 7a-c). The three facies types show pronounced seawater influences consistent with LREE depletion, strong

Ce depletion and sporadic Y enrichment (Table 4; Fig. 7). There is pronounced enrichment of Nd, Sm, Eu, Gd, Tb, and Dy relative to Ho and Tm depletion in some of the ironstone lithologies that distinguishes the ironstone deposits from the underlying and overlying Fe-poor rocks (Fig. 7). REE cross plots, including Zr and Th, show selective enrichment patterns that may be related to provenance (Fig. 8).

PAAS normalized Eu anomalies corrected for anomalously high sedimentary Gd concentrations,  $(Eu/Eu^*)_{SN1}$ , averaged ( $\pm$ standard deviation from the mean)  $1.13 \pm 0.09$ ,  $1.24 \pm 0.08$ , and  $1.04 \pm 0.03$  for the Taghdout carbonate facies, the ironstones, and the siliciclastic stromatolitic rocks, respectively (Fig. 9a). When corrected for elevated Tb,  $(Eu/Eu^*)_{SN2}$  averaged  $1.14 \pm 0.08$ ,  $1.16 \pm 0.09$ , and  $1.09 \pm 0.08$  for the ironstones, the siliciclastic stromatolitic and Taghdout carbonate facies, respectively, with corresponding averaged LREE/HREE ratios of  $3.37 \pm 0.59$ ,  $2.12 \pm 1.23$ , and  $3.96 \pm 0.90$ , respectively. The average Y/Ho ratios for the ironstones, the siliciclastic biolaminites, and Taghdout carbonate facies are  $27.45 \pm 1.14$ ,  $28.40 \pm 2.80$ , and  $27.50 \pm 1.78$ , respectively (Fig. 9b), which are relatively close to a typical crustal and clastic sediment molar ratio of 28, suggesting a strong siliciclastic detrital influence on the REE composition of the sediments. The average Y/Ho ratios reflect lowered reactivity of Y by the presence of siliciclastic material, which as expected, tends to be lower compared to non-siliciclastic deposits (McLennan, 1989; Bau et al., 1997; Planavsky et al., 2010; Halverson et al., 2011).

$La_{SN}$  anomalies  $(La/Yb)_{SN}$  are typically positive with average values of  $1.07 \pm 0.27$ ,  $0.85 \pm 0.62$ , and  $0.95 \pm 0.26$  for the Taghdout carbonates, the Fe-rich deposit and the siliciclastic mats, respectively (Fig. 9c), compared to Precambrian Fe formation values that are typically vary between 0.10 and 0.89 (Planavsky et al., 2010).  $(Tb/Yb)_{SN}$  average values are  $0.96 \pm 0.10$ ,  $1.68 \pm 0.67$ , and  $0.79 \pm 0.09$  whereas  $(Pr/Yb)_{SN}$  have averages of  $0.90 \pm 0.20$ ,  $0.84 \pm 0.51$ , and  $0.91 \pm 0.24$  for the Taghdout carbonates, the Fe-rich deposit and the siliciclastic mats, respectively (Fig. 9d). The  $(Sm/Yb)_{SN}$  ratios averaged  $0.98 \pm 0.096$ ,  $1.18 \pm 0.31$ , and  $0.77 \pm 0.14$  for the Taghdout carbonates, the Fe-rich deposits and the siliciclastic biolaminites, respectively (Fig. 9e), while the  $(Eu/Sm)_{SN}$  averages for the Taghdout carbonates, the Wanimzi ironstones and the siliciclastic biolaminites are  $0.96 \pm 0.096$ ,  $1.14 \pm 0.31$ ,  $1.06 \pm 0.06$  respectively (Fig.

9f).  $Gd_{SN}$  anomalies  $[(Gd/Gd^*)_{SN} = Gd_{SN}/(0.33Sm_{SN} + 0.67Tb_{SN})]$  have average values of  $0.92 \pm 0.02$ ,  $1.13 \pm 0.13$ , and  $0.91 \pm 0.06$  for the Taghdout carbonates, the ironstones and the siliciclastic stromatolites, respectively (Fig. 9g). The strong positive  $Gd_{SN}$  anomalies for the Wanimzi Fe-rich deposit is consistent with those found in many Precambrian IFs.

#### 4.6. Redox reconstruction

With the exception of two samples, the three successions (Fig. 9a) display pronounced true cerium anomalies ( $Ce/Ce^*$ ). However, redox reconstruction using Fe-based redox proxy points to mainly ferruginous and anoxic bottom water during the deposition of the ironstones and the carbonate lithologies, with full water column oxygenation limited to the Fe-poor stromatolitic reference rocks (Fig. 10b-c).

#### 4.7. Fe Isotopes

Bulk  $\delta^{56}Fe$  distribution in the stromatolitic and the Wanimzi Fe-rich lithologies range from  $0.45\text{‰}$  to  $0.61\text{‰}$  and  $-0.41\text{‰}$  to  $0.35\text{‰}$  with means of  $0.52\text{‰}$  and  $-0.03\text{‰}$ , respectively (Fig. 11a-b; Table 3). With a fractionation factor of  $0.55\text{‰}$  (i.e.,  $\Delta^{56}Fe = \delta^{56}Fe_{\text{stromatolitic unit}} - \delta^{56}Fe_{\text{Fe-rich units}}$ ), the data show that the siliciclastic stromatolitic rocks are  $\delta^{56}Fe$  enriched compared to the Fe-rich units. At  $<5$  wt.% Fe concentration,  $\delta^{56}Fe$  values become increasingly positive, and at  $>5$  wt.% Fe concentration, they switch towards being more negative, with the exception of sample AG08 and AG12 (Fig. 11c).

### 5.0. Discussion

#### 5.1. Sediment mineralogy and paragenesis

The primarily siliciclastic composition of the three studied successions, differing only in their Fe, quartz, and carbonate contents, suggests formation of these deposits in a stable shallow marine platform environment (e.g. Schofield et al., 2006; Ennih and Liegeois, 2008; Jessell et al., 2016). The heterolithic bedding planes and the abiotic and biotic structures common in both the Wanimzi and the Imi n'Tizi Formations are consistent with their previously described deposition in a shallow marine setting marked by intermittent desiccation

intervals characterized by shrinkage cracks (Bouougri and Porada, 2002). The high siliciclastic content of the studied successions characterized by well-sorted, angular, rounded grains that range in size from fine to coarse clasts, and the presence of extensive ripple marks and desiccation cracks, are typical features of peritidal environments.

The studied ironstone facies lack typical mineral assemblages associated with late stage diagenesis and metamorphism. Secondary mineral phases such as Fe carbonates, often interpreted to be products of reductive transformation of ferric Fe during burial diagenesis and lithification, could not be detected by XRD, consistent with a low Fe carbonate signal obtained by the sequential Fe extraction method. Collectively, this observation suggests that the emergence of more energetic electron donors such as nitrate in post-GOE seawater (e.g., Stüeken et al., 2016) may have subdued DIR bacteria activity relative to the Archean. For instance, Archean IFs record high Fe carbonate concentrations compared to the simpler and mainly hematite-rich mineralogy of Proterozoic and Phanerozoic IFs (Bekker et al. 2010, Chi Fru et al., 2013; Lechte et al., 2018). Negligible post-depositional transformation is further evidenced by the mainly hematite cement considered to reflect primary to early diagenetic sedimentary features in Fe formations (Chi Fru et al., 2013, 15b, 2018a; Sun et al., 2015; Halverson et al., 2011). Mineralogical and microscopic analyses, combined with Fe speciation data, suggest primary and diagenetic pyrite deposition is imperceptible across the succession and no evidence was found to support pyrite oxidation as the source of ferric Fe in the rock. Significant sulfide production is expected to inhibit ferric Fe deposition through rapid chemical reaction with ferrous Fe, combined with abiotic ferric Fe reduction by sulfide (Wensheng and Millero, 1996; Poulton et al., 2004). The floating of silty grains in the Fe-rich cement and the occurrence of hematite, together with indiscernible grain replacement and transformation of the primary hematite (Figs. 5c-d; Appendix C-D), point to minimal compaction diagenesis and to the syngenetic origin of hematite in the Fe-rich Wanimzi ironstones. Combined with trace element and REE analyses and as discussed further below, collectively the data do not support a subterranean or potential groundwater supply of Fe to the basin during the formation of the Wanimzi ironstones.



The  $\delta^{13}\text{C}_{\text{org}}$  values, supported by the preservation of stromatolitic mats, suggest all three successions were associated with photosynthetic activity. The similar average  $\delta^{13}\text{C}_{\text{org}}$  values for the Fe-rich and stromatolitic layers differ from the underlying Taghdout carbonates by 2.4‰ and 2.0‰, respectively. We propose that similar carbon cycling processes were involved in the deposition of the early Neoproterozoic Waminzi Fe-rich units as in the siliciclastic stromatolitic rocks. The very negative  $\delta^{13}\text{C}_{\text{carbonate}}$  values of the underlying Taghdout Formation suggest negligible burial of photosynthetic  $\text{C}_{\text{org}}$ , which is demonstrated by the low  $\text{C}_{\text{org}}$  concentrations recorded at this time. It is also possible that the extreme negative  $\delta^{13}\text{C}_{\text{carbonate}}$  values reflect authigenic activity of the methane oxidizing bacteria (Schrag et al., 2013). There is no evidence in our dataset to suggest carbonate weathering as a mechanism that produced the large negative  $\delta^{13}\text{C}_{\text{carbonate}}$  excursion (Shields et al., 2017).

## 5.2. Hydrothermal versus seawater contribution

### 5.2.1. Insights from REE Systematics

REEs are reliable source tracers of sedimentary deposits. Being largely immobile in aqueous solution, they tend to behave conservatively during sediment formation (Taylor and McLennan, 1985). For example, La/Sm and Gd/Yb ratios normalized to upper continental crust values are frequently used as sediment source indicators (e.g., Wani and Mondal, 2011). Shale normalized Ce ( $\text{Ce}_{\text{SN}}$ ) depletion is assumed to be a seawater and redox proxy, and  $\text{Eu}_{\text{SN}}$  enrichment, a hydrothermal marker as well as a weathering proxy (Bau and Dulski, 1996; Singh and Rajamani, 2001; Shields et al., 2004; Bau and Koschinsky, 2009). The depletion of  $\text{Ce}_{\text{SN}}$  across the studied succession thus provides significant evidence for major seawater involvement in the origin of the studied facies (e.g., Tostevin et al., 2016). This conclusion is corroborated by independent sedimentological evidence that has long alluded to a marginal sea setting for the studied facies (e.g., Hefferan et al., 2000; Bouougri and Saquaque, 2000, 2004; Ennih and Liégeois, 2001; Thomas et al., 2004; Bouougri and Porada, 2002, 2010; Bouougri et al., 2020).

The statistically supported positive correlations between Nd (usually of hydrothermal or seawater origin) and Pr and Th (both often depleted in hydrothermal fluids) and Ce (of either hydrothermal or seawater provenance)

and Pr (Bau and Dulski, 1996, 1999; Planavsky et al., 2010), suggest a predominantly seawater origin for Ce. The positive correlation between Ce and the non-hydrothermal Pr, combined with the pronounced seawater  $Ce_{SN}$  signal, provide robust support for the latter proposition. Similarly, the lack of correlation amongst the three REEs - Nd vs Ga and Nd vs Eu (Fig. 8d, h), which are commonly enriched in hydrothermal fluids (German and Seyfried, 2014), again suggest REE contributions from seawater, probably as adsorbates of the abundant siliciclastic detritus. The latter proposal is consistent with the strong positive correlations of Ce vs. La and Ce vs. Nd (Fig. 8e-f), which hint that both La and Nd may be of a strong seawater origin. Typically,  $Eu_{SN}$  enrichment is attributed to hydrothermal activity (e.g., Douville et al., 2002; Tivey, 2007; Planavsky et al., 2010; German et al., 2014). However, the subtle positive enrichment of  $Eu_{SN}$  in the samples coupled to the moderate positive correlation between Eu and the non-detrital Zr (Fig. 8l), point to up to 58 % of Eu being associated with the siliciclastic material.

Increasing depletion of HREEs relative to LREEs, typically interpreted as evidence for hydrothermal influence, has been reported for Fe formations across Earth history (e.g., Planavsky et al., 2010; Bau, 1996; Ganno et al., 2017). For example, hydrothermal fluids emitted by modern deep-sea vents are generally enriched in LREE (Mitra et al., 1994; Bau and Dulski, 1999; Craddock et al., 2010), whereas enrichment of HREEs relative to LREEs is a common feature of the modern oxygenated seawater (e.g., Bau et al., 1997; Bolhar et al., 2007) but has also been recorded in hydrothermal fluids in a few cases (e.g., Klinkhammer et al., 1994; Douville et al., 1999). Non-siliciclastic Precambrian Fe formations with pronounced HREE enrichments also contain positive (Eu, La, Y and Ga) $_{SN}$  anomalies (Bau and Dulski, 1996). We propose that the fluctuating LREE/HREE ratios recorded in the Wanimzi ironstones reflect varying degrees of the mixing of hydrothermal fluids with seawater.

Because the entire sample set is characterized by detrital loading, the unique trends in the ironstones cannot be related to an anomaly attributable to detrital contamination relative to the reference underlying and overlying rocks, which are also composed of siliciclastic detritus. We therefore interpret the above observations to reflect long distance transportation and thorough mixing of the Fe-rich fluids with seawater, followed by delivery and deposition on the

margin of the WAC (Fig. 13). The data also imply that the seawater chemical conditions on the WAC margin were radically different from those at the source and during transportation, to enable the quantitative precipitation of dissolved Fe from seawater and transformation into ironstone.

#### *5.2.2. Insights from trace element systematics*

The Wanimzi Fe-rich lithologies are enriched in key redox sensitive elements, such as As, V, Co, Sb, and Fe, that are typically concentrated in submarine hydrothermal fluids by up to eight times relative to modern seawater concentrations (e.g., Douville et al., 2002; Tivey, 2007; German and Seyfried, 2014). This would have been more significant in the Precambrian oceans that experienced much higher levels of hydrothermal activity. For example, Fe supplied by submarine hydrothermal fluids is suggested to be a major source of Fe to Precambrian seawater (see for example Bekker et al., 2010), with values in excess of  $10^3$  ppm reported for fluids from present-day mid-ocean spreading ridges (Tivey et al., 2007).

Evidence shows that, despite the observed loss of reduced Fe escaping from modern hydrothermal vents and during plume dispersal through rapid chemical reactions with oxygenated seawater, the loss of Fe is much slower than previously thought (see Gertman and Findlay, 2020, for a review). The stabilization of Fe through binding with organic matter, inorganic nanoparticles, organic and inorganic colloids results in Fe being transported thousands of kilometers across the open modern ocean (Bennett et al., 2008; Toner et al., 2009; Sander and Koschinsky, 20011; Yücel et al., 2011; Resing et al., 2015; Fitzsimmons et al., 2017; Lough et al., 2019). However, the higher mobility of Fe in the predominantly anoxic Precambrian seawater would have allowed for more stable transportation of Fe across oceans and for thorough mixing with seawater. Because shallow oxygenation of the surface ocean was prevalent at this time, contact with oxic marginal seawater would have promoted the precipitation and burial of hydrous ferric oxyhydroxides and their diagenetic products in the affected shallow water sediments. Fe concentrations of up to  $10^5$  ppm are recorded in the continental platform sediments in the Wanimzi Formation (Table 2), being about a factor of two greater than the concentrations

in modern submarine hydrothermal systems (Tivey, 2007; German and Seyfried, 2014).

The variation in Fe and quartz content in the Fe-rich lithologies point to related changes in the intensity of the delivery of Fe-rich fluids to seawater (see for example Chi Fru et al., 2013; 2018). For instance, Zn/Co ratios with high and low values associated with hydrothermal and detrital influence, respectively (Toth, 1980; Halverson et al., 2011), largely decreased from the carbonates through to the overlying Neoproterozoic siliciclastic stromatolitic succession (Fig. 6f). Mo/W ratios, a measure of sediment formation from sulfide-rich fluids due to the high reactivity of Mo towards sulfide relative to W, are generally low (Fig. 6g). This observation suggests potential precipitation of particle-reactive thiomolybdate with sulfide minerals near the source of the Fe-rich fluids and subsequent precipitation of W enriched in the migrating plume relative to Mo with primary ferric Fe minerals on the oxygenated continental margin (see for example Mohajerin et al., 2016; Bauer et al., 2017; Dellwig et al., 2019).

The higher enrichment of W in the Fe-rich facies relative to the upper continental crust, the siliciclastic stromatolitic, and Taghdout carbonate rocks, support a significant supply of W to the basin by hydrothermal activity (Table 2). Consistent with the latter observation, the Fe-rich samples are ~2 and 4 times more enriched in W than the siliciclastic stromatolite-containing and carbonate facies, respectively (Table 2). Similarly, the strong enrichment of As and Sb in Fe-rich layers relative to the siliciclastic layer, the carbonates and upper continental crust are similar to those for Fe, consistent with a suggested hydrothermal original of these elements (e.g., Breuer and Pichler, 2013; Feely et al., 1991; 1998, Chi Fru et al., 2013; Zeng et al., 2018; Table 2). The latter proposition is supported by a clear lack of similar significant enrichment of As, Sb, and Fe in the siliciclastic and carbonate layers relative to the upper continental crust. (Table 2). Th/U ratios frequently used as a redox proxy whereby U is enriched in deoxygenated sediments relative to Th (Kerrick et al., 2013; Manikyamba, 2018), are relatively low in the Fe-rich sequences compared to the reference overlying and underlying Fe-poor samples (Fig. 6h).

The above observations suggest intense and prolonged hydrothermal activity linked to an Fe-rich source that enabled significant Fe enrichment in the fluids that deposited the Wanimzi ironstones on the coast of the WAC. The Fe

concentrations were probably much higher in the pristine hydrothermal fluids emerging from the vents, given that substantial quantities of Fe would have been precipitated with hydrothermal sulfides near the vents as commonly observed at various modern hydrothermal vent fields. Combined, the Fe-rich fluids that formed the Wanimzi ironstones and the sharp absence of ironstones in the underlying and overlying successions suggest sudden initiation and termination of the of supply Fe-rich fluids to the WAC during deposition of the unique Wanimzi ironstones. Intriguingly, this proposition is consistent with the suggested age of the Wanimzi Formation being coincident with the inception of rifting and breakup of the Rodinia supercontinent dated at 920-890 Ma in many Proterozoic cratons (e.g. Evans et al., 2016; Zhou et al., 2018; Baratoux et al., 2019; Chavez et al., 2019) and in the Anti-Atlas at 883 Ma (Bouougri et al., 2020). Such widespread rifting event and supercontinent breakup would have inevitably led to the development of active submarine hydrothermal vent complexes.

In addition to Fe, prominent hydrothermal metals like Co, As, V, Sb, Pb and Cu (Tivey, 2007; Beuer and Pichler, 2013; German and Seyfried, 2014; Rouxel et al., 2018), show variable but stronger enrichments in the Wanimzi ironstones compared to the Fe-poor reference sequences (Fig. 6; Table 2). For instance, the concentration of As in the ironstones is up to 80 times greater than the 3000 times As concentrations discharged by some modern back and Island arc basin shallow submarine hydrothermal fluids compared to unadulterated seawater levels (e.g., Breuer and Pichler, 2013). Importantly, Fe-hematite sedimentary rocks deposited from these pristine high As-containing submarine As-rich hydrothermal fluids are reported to record similar anomalously high As concentrations (e.g., Chi Fru et al., 2013). Even more interestingly, the As concentrations in the Fe-rich lithologies are up to 1400 times in excess of concentrations in hydrothermal fluids from the East Pacific Rise and 4600 times over the values reported for the Mid-Atlantic Ocean Ridge (Breuer and Pichler, 2013). Further, the average As concentration in the Fe-rich lithologies is 18 and 9 times above those present in the overlying siliciclastic and underlying carbonates in the Taghdout Formation, respectively. This observation is most parsimoniously interpreted to represent the levels of As concentrations in the waters that formed the different successions based on the assumption that the

Fe content of the sediments did not skew the data towards the enrichment of As by the ferric Fe in the Wanimzi Formation. This appears not to have been the case considering that the As/Fe ratios in these sediments are generally homogenous across the entire succession (Appendix O). Moreover, the comparable behaviors of As and Sb (Fig. 6a-b) across the studied successions have previously been related to water mass type and interaction with rocks by hydrothermal fluids and migrating hydrothermal plumes emitted by active vents (Wu et al., 2017; Zeng et al., 2018). Importantly, 63 % of the As in the Fe-rich lithologies is explained by a positive covariance with Fe (Fig. 12a), similar to observations between hydrothermal ferric Fe and As (e.g., Feely et al., 1991; Chi Fru et al., 2015). Similar to the behavior of hydrothermal ferric Fe and V, a positive correlations was observed between V and Fe in the ironstones (Fig. 12b; Feely et al., 1998). Only a weak positive correlation was observed for Fe, Cu, and none for Mo. As and Mo showed a strong positive correlation (Fig. 12c), suggesting they likely had the same hydrothermal source considering that both can be strongly enriched in hydrothermal fluids (German and Seyfried, 2014). However, the lack of correlation between Fe and Mo implies that precipitation of Mo into the ironstones may have been independent of ferric Fe precipitation.

The As data suggest that the microbial communities associated with the water mass that formed the Fe-rich lithologies would have had to combat the dramatic effects of arsenic toxicity, which include inhibiting the synthesis and function of proteins by As(III) in reducing environments and cell phosphate uptake and metabolism by As(V) in oxygenated habitats (Cervantes et al., 1994; Smedley and Kinniburgh, 2002). Such a scenario would have impeded primary production, as is common in modern oceans, compared to the reference arsenic-poor settings. This would have had major implications for carbon fixation, organic carbon burial, and oxygenation by the activities of the marine cyanobacteria (Dyhrman and Haley, 2011; Wurl et al., 2013; Saunders and Rocap, 2016; Giovannoni et al., 2019). However, a full set of arsenic detoxifying genes believed to have been present by the earliest Tonian Period (Chen et al., 2020), together with widespread mechanisms for controlling genes that select for phosphate at the expense of As(V), would have alleviated this situation to some extent. These genes have been shown to be abundant in a

modern submarine hydrothermal system exposed to hydrothermal fluids containing 3000 times more As than seawater concentrations (Chi Fru et al., 2018b). This would have partially mitigated As toxicity when the deep-sea deoxygenated hydrothermal As-rich fluids rose and mixed with the shallow seawater on the coast of the WAC, possibly supporting asenotrophic microbial activity in the deoxygenated waters (Visscher et al., 2020). Similarly, key nutrients like Mo and V, critical for nitrogen fixation and thus primary production in the early oceans (Zhang et al., 2014), would have equally contributed to maintaining a good degree of primary production as reflected by the photosynthetic  $\delta^{13}\text{C}_{\text{org}}$  proxy signature preserved in the ironstones.

### 5.2.3. Insights from Fe isotope systematics

The  $\delta^{56}\text{Fe}$  values of modern sulfide-rich hydrothermal fluids at seafloor mid-ocean ridges typically range from -1.26‰ to -0.14‰ with a reported average of -0.52‰ (Sharma et al., 2001; Severmann et al., 2004; Bennett et al., 2009; Li et al., 2017; Rouxel et al., 2016). These  $\delta^{56}\text{Fe}$ -depleted values are balanced by enriched seawater  $\delta^{56}\text{Fe}$  ratios that vary from -0.64‰ to up to 0.80‰ with an estimated average of 0.34‰ (Bennet et al., 2009; Rouxel et al., 2016; Fitzsimmons et al., 2016, 2017; Karl et al., 2016; Li et al., 2017; Lough et al., 2017). In contrast, a mean value of +0.1‰ has been suggested for sulfide-depleted hydrothermal fluids from Pele's pit in the Hawaiian Loihi submarine volcanic hotspot similar to neighboring seafloor basaltic  $\delta^{56}\text{Fe}$  ratios (Rouxel et al., 2018). The  $\delta^{56}\text{Fe}$  values are commonly controlled by a combination of biological and abiological processes, including chemical precipitation of Fe oxides during abiotic and biotic oxidation of Fe with oxygen, anoxic precipitation of Fe sulfide, microbial reduction of Fe, water rock interactions, and phase separation (e.g., Rouxel et al., 2008; Severmann et al., 2004; Li et al., 2017; Rouxel et al., 2018; Heard and Dauphas, 2020). However, there is a consensus that net seawater  $\delta^{56}\text{Fe}$  values are generally heavier relative to submarine hydrothermal fluids (Radic et al., 2011; Conway et al., 2014, 2015). For instance, high temperature hydrothermal fluids with light  $\delta^{56}\text{Fe}$  ratios of -0.23‰ from the Rainbow hydrothermal vents precipitate and deliver Fe with  $\delta^{56}\text{Fe}$  values similar to those recorded in the receiving deep North Atlantic seafloor sediments (e.g., Severmann et al., 2004). Further, studies have shown that Fe

isotopes are more sensitive to local environmental conditions (e.g., precipitating authigenic sulfide and Fe oxyhydroxide minerals) than to extant biological and abiological processes (Lough et al., 2017; Rouxel et al., 2018). This implies that Fe isotopes are best applied as tracers of environmental change processes. The source and sink of Fe in the ocean and global Fe biogeochemical cycling are dependent on our knowledge of fluxes between various Fe pools and their associated isotopic signatures. Therefore, quantitative precipitation of primary Fe from seawater and hydrothermal fluids is expected to conservatively display  $\delta^{56}\text{Fe}$  values reflecting sources and variable mixing with seawater. Similarly, examining the behavior of Fe isotopes during the dispersal and transportation of hydrothermal plumes through seawater can provide information on the sources and sinks of Fe to seawater as well as the influence of hydrothermal Fe in the deposition of Fe Formations on ancient continental margins.

The variability of  $\delta^{56}\text{Fe}$  in the Fe-rich sedimentary units from the Wanimzi Formation are more similar to the signatures of hydrothermal fluids than for modern oxic seawater values that are often more homogeneously heavy. This view is supported by the transition from light to exceptionally heavy  $\delta^{56}\text{Fe}$  values in the overlying reference Fe-poor stromatolitic succession shown to have the least hydrothermal influence by their REE+Y and trace metal composition. Because Fe is insoluble in oxygenated seawater, its concentration in the modern ocean is usually in the nM to pM range, while  $\mu\text{M}$  to mM concentrations are documented in anoxic hydrothermal fluids and plumes (Elderfield and Schultz, 1996; Bennett et al., 2008; Fitzsimmons et al., 2014; Resing et al., 2015; Lough et al., 2017). Similar to this observation, the Fe-rich lithologies, which were deposited beneath anoxic bottom waters, are 26 times more enriched in Fe than the stromatolitic rocks, which we argue formed in full bottom water oxygenated conditions. Moreover, these Fe-rich lithologies contain  $\delta^{56}\text{Fe}$  signatures that on average are light ( $-0.03\text{‰}$ ) compared to the heavy values of up to  $0.52\text{‰}$  measured in the stromatolitic Fe-poor reference rocks that are believed to have experienced the least hydrothermal influence of all the samples. Further, mid-ocean ridge plumes from the East Pacific Rise with similar  $\delta^{56}\text{Fe}$  values of  $-0.91\text{‰}$  and  $-0.03\text{‰}$  were interpreted to have resulted from variable mixing of hydrothermal fluids with seawater, lithospheric interactions, and biogenic Fe cycling (Rouxel et al., 2016).



The lowest  $\delta^{56}\text{Fe}$  value of  $-0.41\text{‰}$  in the Wanimzi ironstones has been reported for Fe particles in endmember hydrothermal plumes following systematic stripping of light  $^{56}\text{Fe}$  by Fe sulfide minerals (Rouxel et al., 2016). In the absence of direct evidence for the sulfide content of the original fluids that formed the ironstones, Mo/W ratios are used as proxies for Mo depletion and W enrichment during the precipitation of particulate sulfide minerals (Mohajarin et al., 2016; Bauer et al., 2017; Dellwig et al., 2019). Upon transition to conditions that support the production of ferric Fe, W is preferentially sequestered relative to Mo. The variable levels of Mo/W ratios in the Fe-rich lithologies (Fig. 6g) may therefore be linked to the influence of sulfide fluids. However, owing to the absence of correlation amongst Mo, W and Fe, it is suggested that Mo and W enrichments in the ironstones were not the direct results of Fe precipitation. The positive correlation between Mo and As in the Fe-enriched lithologies (Fig. 12c), both being strong chalcophiles possessing high affinities for sulfide, suggests low sulfide concentration in the source vent fluids. This, allowed substantial amounts of As, Mo, and Fe to escape precipitation with vent sulfides and subsequent enrichments in the ironstones. The mainly heavier  $\delta^{56}\text{Fe}$  signal of up to  $+0.61\text{‰}$  recorded in the Fe-poor siliciclastic Imi n'Tizi reference rocks and their REE+Y distribution, are comparable to values recorded in some modern seawater. In addition, these reference Fe-poor rocks lack evidence for strong hydrothermal influence, while the lighter  $\delta^{56}\text{Fe}$  values in the ironstones are more consistent with a hydrothermal source.

Our  $\delta^{56}\text{Fe}$  values fall within the range for published Proterozoic Fe formations believed to have been influenced by varying degrees of hydrothermal input (Planavsky et al., 2010; Yan et al., 2010; Halverson et al., 2011; Li et al., 2017; Heard and Dauphas, 2020; Fig. 11b). The simple hematite and quartz mineralogy of the Wanimzi ironstones is comparable to the reported predominance of hematite in syn-glacial Neoproterozoic Snowball Fe formations (Bekker et al., 2010; Halverson et al., 2011; Cox et al., 2013; Lechte et al., 2013). However, the narrower range of  $\delta^{56}\text{Fe}$  values in the Wanimzi ironstones ( $-0.41\text{‰}$  to  $0.35\text{‰}$ ) are more similar to modern hydrothermal  $\delta^{56}\text{Fe}$  seafloor deposits (Planavsky et al., 2010; Rouxel et al., 2008; 2016; 2018), while the wider range in  $\delta^{56}\text{Fe}$  values of  $-0.7\text{‰}$  to  $1.2\text{‰}$  in Neoproterozoic syn-

glacial Fe formations compared to the narrower records in the Wanimzi Fe-rich lithologies, point perhaps to varying degrees of partial Fe oxidation (e.g., Halverson et al., 2011; Table 3).

The data suggest that the relationship between Fe concentrations and Zn/Co ratios may be a stronger indicator of the degree of hydrothermal influence than the relationship between  $\delta^{56}\text{Fe}$  and Zn/Co ratios in the studied succession. For instance, although  $\delta^{56}\text{Fe}$  lacked a significant negative correlation with Fe concentrations and the Zn/Co ratios, a goodness of fit positive correlation between Fe and Zn/Co points to hydrothermal activity contributing to at least 64 % of bulk Fe enriched in the Fe-rich sediments (Appendix P). Further, while Fe concentrations in the Wanimzi Formation are much elevated relative to the underlying Paleoproterozoic Taghdout carbonates and the overlying Ediacaran Imi n-Tizi siliciclastic deposits, the Zn/Co ratios of the Wanimzi ironstones are lower compared to the Fe-poor carbonates and higher relative to the Fe-poor Ediacaran deposit. This suggests potential mixing of seawater with Fe-poor hydrothermal fluids during the deposition of the Taghdout carbonates and progressively negligible hydrothermal influence during the deposition of the siliciclastic rocks above the Wanimzi ironstones. The positive  $\delta^{56}\text{Fe}$  values of the Fe-poor, non-hydrothermal siliciclastic sediments above the Wanimzi ironstones, linked to low seawater Fe concentration and Zn/Co ratios, reflect expected heavier  $\delta^{56}\text{Fe}$  values resulting from low seawater Fe concentration and hydrothermal activity in some modern seawater settings. Moreover, quantitative and partial oxidation of Fe by biotic and abiotic processes, would result in quantitative or partial fractionation of Fe isotopes between the precipitated Fe(III) and residual dissolved hydrothermal Fe(II), decoupling the  $\delta^{56}\text{Fe}$  and Zn/Co signals.

### 5.3. Redox depositional conditions

The pronounced  $\text{Ce}_{\text{SN}}$  depletion observed in our samples is a feature common to modern oxygenated seawater (e.g., Bau and Dulski, 1996; Singh and Rajamani, 2001; Shields et al., 2004; Bau and Koschinsky, 2009). Statistical test for the redox state of seawater by the calculated true negative  $\text{Ce}/\text{Ce}^*$  anomaly, indicates extensive oxygenation of the WAC margin (Fig. 10a; Bau, 1996; Planavsky et al., 2010). However, redox reconstruction using the Fe-

based redox proxy (Poulton and Canfield, 2005; Poulton and Canfield, 2011; Clarkson et al., 2014) suggests deposition of both the reference siliciclastic carbonates from the Taghdout Formation and the Wanimzi ironstone lithologies occurred beneath a deoxygenated water column, while full water column oxygenation coincides with the reference Fe-poor siliciclastic Imi n'Tizi rocks. Persistent ferruginous conditions were widespread at this time while euxinia is not supported by the data.

The siliciclastic detritus derived from continental weathering likely influenced the REE+Y distribution patterns, as supported by the corresponding average Y/Ho clastic values. Importantly, because the entire sequence is siliciclastic, the divergent redox conditions indicated by the Ce/Ce\* and the Fe-based redox proxies, are interpreted to reflect the unique ability of the Fe-based redox proxy to record the emergent anoxic bottom water depositional conditions induced by the fluids that delivered Fe to the continental margin. Further, as the chemocline deepens, the Y/Ho ratios are expected to decrease as the Ce/Ce\* anomaly increases because of effective dissolution of Fe(III)(oxyhydr)oxide particles that tend to be relatively enriched in Ho and Ce (Bau et al., 1997; Planavsky et al., 2010; Halverson et al., 2011). Instead the lack of an inverse correlation between Y/Ho and Ce/Ce\*, together with static average Y/Ho ratios across the sampled section, are consistent with a stable shallow marine platform experiencing little or no change in the depth of the chemocline.

We propose that the shallow margins of the WAC were fully oxygenated prior to the process that introduced Fe-rich fluids to the platform waters. This suggestion implies that the process that conveyed the ferruginous fluids to the WAC margin to promote kinetic deoxygenation of the shallow seawater mass was too rapid to allow equilibration with the atmosphere and the establishment of a stable chemocline with fluctuating depth. Moreover, the Y/Ho ratios being more similar to composite shale and clastic sediment values, imply that the REE+Y values are influenced by contribution of clast weathered from the upper continental crust, relative to hydrothermal input. This is consistent with the lack of meaningful correlation between the inferred hydrothermal Fe and corresponding Y/Ho ratios, a strong seawater Ce<sub>SN</sub> and subtle Eu<sub>SN</sub> anomalies, the latter being undetectable in some cases. The negative  $\delta^{57}\text{Fe}$  correlation to Y/Ho ratios recorded in syn-glacial Neoproterozoic Fe formations isolated from

continental contamination by detrital material, and marked by the scavenging of REE+Y by Fe oxides precipitated from a deepening chemocline (Halverson et al., 2011), is not observed in our samples.

Instead, the Fe-based redox proxy points to a sudden deoxygenation event of what was likely a fully oxygenated shallow water mass by anoxic submarine hydrothermal plumes released from a distal anoxic deep-sea source. Attenuation of the REE+Y hydrothermal signal is interpreted to be the product of long distance plume transportation to the continental margin. As a result, vigorous mixing of the migrating plume with seawater and particle precipitation, systematically weakened the hydrothermal REE+Y signal (Fig. 13). This observation is supported by the attenuated hydrothermal Eu signature, reported for various Precambrian IFs to be related to high temperature hydrothermal provenance of Fe (Michard, 1989; Klein and Beukes, 1993; Halverson et al., 2011).

The Fe-based redox trends are supported by variations in associated redox sensitive trace metals such as elevated levels of U and V in the Fe-rich lithologies (Fig. 6-c; Table 2). For example, U concentrations average  $1.6 \pm 0.6$  ppm in the ironstones compared to  $1.0 \pm 0.5$  ppm and  $\sim 0.4 \pm 0.0$  ppm in the reference Fe-poor siliciclastic rocks above and beneath the Fe-rich sequence, respectively. Similarly, V concentrations averaged  $70.8 \pm 50.6$  relative to  $36.3 \pm 6.6$  ppm and  $\sim 8.5$  for the Fe-poor rocks above and below the Fe-rich layer, respectively. These average values are below continental crust concentrations of 2.8 ppm and 107 ppm for U and V, respectively (McLennan (2001). Nonetheless, the higher co-enrichment of U and V in the Fe-rich lithologies relative to the Fe-poor lithologies, is consistent with the strong anoxic, non-euxinic, ferruginous depositional conditions established by our Fe speciation analysis in Figure 10b-c (e.g., Tribovillard et al., 2006; Scott et al., 2008; Scott & Lyons, 2012). Equally, the lack of any meaningful Mo enrichment is consistent with the absence of euxinic conditions suggested by our Fe speciation data across the studied section (Fig. 6a).

## 6. Conclusions

We present a siliciclastic ironstone deposit estimated to be of Early Neoproterozoic age in the Anti Atlas Mountains of Morocco, marked by a unique

hematite enrichment style different from that reported for most Precambrian Fe Formations. The data indicate a predominantly anoxic deep ocean that enabled the transportation and delivery of strongly reducing submarine hydrothermal plumes to an oxygenated early Neoproterozoic shallow marine wave-influenced platform. Here, reduced Fe was mixed with and oxidized by oxygenated seawater and deposited in association with siliciclastic material weathered from the continent. Based on the combined Ce/Ce\* anomaly and Fe-based bottom water redox reconstruction, we propose that the marginal shallow seawaters were fully oxygenated until the anoxic hydrothermal fluids upwelled from the deep-sea and rapidly deoxygenated the shallow waters for an extended period of time. This resulted in the oxidation of upwelling reduced hydrothermal ferrous Fe and the deposition of primary ferric Fe that was preserved as hematite in the Wanimzi ironstones. The data further suggest that, in addition to the open oceans being redox stratified to enable large-scale migration of reduced hydrothermal plumes to the WAC margin, the breakup of Rodinia supercontinent may have initiated widespread early Neoproterozoic redox processes that orchestrated extended episodes of widespread shallow seawater anoxia in affected basins. This observation is consistent with the proposition that increased deposition of ferric Fe during the Early Neoproterozoic may have suppressed extensive seawater-atmosphere oxygenation through the scavenging and burial of dissolved phosphate by ferric Fe particles precipitating from seawater (Guilbard et al., 2020).

## Acknowledgements

This work was funded by the European Research Council (Grant No. 336092 to ECF). We acknowledge funding support from Hassan II Academy of Science and Technology (HIIAST/SDU/2016.02 El Albani et al.) and the funding fellowship awarded to I. Chraiki).

## References

Baratoux, L., Söderlund, U., Ernst, R.E., de Roever, E., Jessell, M.W., Kamo, S., Naba, S., Perrouty, S., Metelka, V., Yatte, D., Grenholm, M., Diallo, D.P., Ndiaye, P.M., Dioh, E., Cournède, C., Benoit, M., Baratoux, D., Youbi, N., Rousse, S., Bendaoud, A., 2019. New U–Pb Baddeleyite ages

- of mafic dyke swarms of the West African and Amazonian Cratons: implication for their configuration in supercontinents through time. In: Srivastava, R.J., Ernst, R.E., Peng, P (Eds.), *Dyke Swarms of the World: A Modern Perspective*, Springer, Singapore, pp. 263–314.
- Bau, M., Dulski, P. (1996). Distribution of yttrium and rare-earth elements in the Penge and Kuruman iron-formations, Transvaal Supergroup, South Africa. *Pre. Res.* 79:37–55. [https://doi.org/10.1016/0301-9268\(95\)00087-9](https://doi.org/10.1016/0301-9268(95)00087-9).
- Bau, M., Mdler, P., Dulski, P., 1997. Yttrium and lanthanides in eastern Mediterranean seawater and their fractionation during redox-cycling. *Mar. Chem.* 56:123–131. [https://doi.org/10.1016/S0304-4203\(96\)00091-6](https://doi.org/10.1016/S0304-4203(96)00091-6).
- Bau, M., Dulski, P., 1999. Comparing yttrium and rare earths in hydrothermal fluids from the Mid-Atlantic Ridge: implications for Y and REE behaviour during near-vent mixing and for the Y/Ho ratio of Proterozoic seawater. *Chem. Geol.* 155:77–90. [https://doi.org/10.1016/S0009-2541\(98\)00142-9](https://doi.org/10.1016/S0009-2541(98)00142-9).
- Bau, M., Koschinsky, A., 2009. Oxidative scavenging of cerium on hydrous Fe oxide: Evidence from the distribution of rare earth elements and yttrium between Fe oxides and Mn oxides in hydrogenetic ferromanganese crusts. *Geochem. J.* 43:37–47. <https://doi.org/10.2343/geochemj.1.0005>.
- Bauer, S., Blomqvist, S., Ingri, J., 2017. Distribution of dissolved and suspended particulate molybdenum, vanadium, and tungsten in the Baltic Sea. *Mar. Chem.* 196:135–147. <https://doi.org/10.1016/j.marchem.2017.08.010>.
- Bekker, A., Slack, J.F., Planavsky, N., Krapež, B., Hofmann, A., Konhauser, K.O., Rouxel, O.J., 2010. Iron Formation: The Sedimentary Product of a Complex Interplay among Mantle, Tectonic, Oceanic, and Biospheric Processes. *Econ. Geol.* 105:467–508. <https://doi.org/10.2113/econgeo.107.2.379>.
- Bennett, S.A., Achterberg E.P., Connelly, D.P., Statham, P.J., Fones, G.R., German, I.C.R., 2008. The distribution and stabilisation of dissolved Fe in deep-sea hydrothermal plumes. *Earth Planet. Sci. Letts.* 270:157–167. <https://doi.org/10.1016/j.epsl.2008.01.048>.
- Bennett, S.A., Rouxel, O., Schmidt, K., Garbe-Schönberg, D., Statham, P.J., German, C.R., 2009. Iron isotope fractionation in a buoyant hydrothermal plume, 5°S Mid-Atlantic Ridge. *Geochim. Cosmochim. Acta* 73:5619–

1049 5634. <https://doi.org/10.1016/j.gca.2009.06.027>.

1050 Bouougri, E. H., Ait Lahna, A., Tassinari, C. C. G., Basei, M. A. S., Youbi, N.,  
 1051 Admou, H., Saquaque, A., Boumehdi, A., Maacha, L., 2020. Time  
 1052 constraints on Early Tonian Rifting and Cryogenian Arc terrane-continent  
 1053 convergence along the northern margin of the West African craton: Insights  
 1054 from SHRIMP and LA-ICP-MS zircon geochronology in the Pan-African  
 1055 Anti-Atlas belt (Morocco). *Gond. Res.* 85:169–188.  
 1056 <https://doi.org/10.1016/j.gr.2020.03.011>.

1057 Bouougri, E. H. and Porada, H., 2011. Biolaminated siliciclastic deposits. In:  
 1058 *Advances in Stromatolite Geobiology, Lecture Notes in Earth Sciences*,  
 1059 Springer Switzerland, pp. 507–524.

1060 Bouougri, E. H. and Saquaque, A., 2004. Lithostratigraphic framework and  
 1061 correlation of the Neoproterozoic northern West African Craton passive  
 1062 margin sequence (Siroua-Zenaga-Bouazzar Elgraara Inliers, Central Anti-  
 1063 Atlas, Morocco): An integrated approach. *J. Afri. Earth Sci.* 39:227–238.  
 1064 <https://doi.org/10.1016/j.jafrearsci.2004.07.045>.

1065 Bouougri, E., 2003. The Moroccan Anti-Atlas: the West African craton passive  
 1066 margin with limited Pan-African activity. Implications for the northern limit  
 1067 of the craton – discussion. *Pre. Res.* 120:179–183.  
 1068 [https://doi.org/10.1016/S0301-9268\(02\)00169-9](https://doi.org/10.1016/S0301-9268(02)00169-9).

1069 Bouougri, E. and Porada, H., 2002. Mat-related sedimentary structures in  
 1070 Neoproterozoic peritidal passive margin deposits of the West African  
 1071 Craton (Anti-Atlas, Morocco). *Sed. Geol.* 153:85–106.  
 1072 [https://doi.org/10.1016/S0037-0738\(02\)00103-3](https://doi.org/10.1016/S0037-0738(02)00103-3).

1073 Bouougri, E. H. and Saquaque, A., 2000. Organisation stratigraphique et  
 1074 structure de la marge Anti-Atlasique du craton Ouest-Africain au sud du  
 1075 Siroua (Néoprotérozoïque, Anti-Atlas central, Maroc). *Comptes Rendus de*  
 1076 *l'Académie Des Sciences - Series IIA - Earth Planet. Sci.* 330:753–759.  
 1077 [https://doi.org/10.1016/S1251-8050\(00\)00232-9](https://doi.org/10.1016/S1251-8050(00)00232-9).

1078 Breuer, C., Pichler T., 2013. Arsenic in marine hydrothermal fluids. *Chem. Geol.*  
 1079 348:2–14. <https://doi.org/10.1016/j.chemgeo.2012.10.044>.

1080 Brocks, J. J., Jarett, A.J.M., Sirantoine, E., Hallmann, C., Hoshino, Y, and  
 1081 Liyanage T., 2017. The rise of algae in Cryogenian oceans and the  
 1082 emergence of animals. *Nature* 548:578–581. DOI:10.1038/nature23457.

1083 Canfield, D. E., 1998. A new model for Proterozoic ocean chemistry. *Nature*  
1084 396:450–453. DOI:10.1038/24839.

1085 Cervantes, C., Ji, Guangyong, Ramirez, J.L., Silver, S., 1994. Resistance to  
1086 arsenic compounds in microorganisms. *FEMS Microbiol. Rev.* 15:355–  
1087 367. [https://doi.org/10.1016/0168-6445\(94\)90069-8](https://doi.org/10.1016/0168-6445(94)90069-8).

1088 Chavez, A.D.O., Ernst, R.E., Söderlund, U., Wang, X., Naeraa, T., 2019. The  
1089 920–900 Ma Bahia-Gangila lip of the São Francisco and Congo cratons  
1090 and link with Dashigou-Chulan lip of North China craton: new insights from  
1091 U-Pb geochronology and geochemistry. *Pre. Res.* 329, 124–137.  
1092 <https://doi.org/10.1016/j.precamres.2018.08.023>.

1093 Chen, S.-C., Suna, G.-X., Yan, Y., Konstantinidis, K.T., Zhange, S.-Y., Deng,  
1094 Y., Lia, X.-M., Cuia, H.-L., Musat, F., Popp, D., Rosenh, B.P., Y.-G., Zhu.,  
1095 2020. The Great Oxidation Event expanded the genetic repertoire of  
1096 arsenic metabolism and cycling. *Proc. Natl. Sci. U.S.A.* 117:10414-10421.  
1097 <https://doi.org/10.1073/pnas.2001063117>.

1098 Chi Fru, E., Piccinelli, P., Fortin, D., 2012. Insights into the global microbial  
1099 community structure associated with iron oxyhydroxide minerals deposited  
1100 in the aerobic biogeosphere. *Geomicrobiol. J.* 29:587–610.  
1101 <https://doi.org/10.1080/01490451.2011.599474>.

1102 Chi Fru, E., Ivarsson, M., Kiliass, S.P., Bengtson, S., Belivanova, V., Marone, F.,  
1103 Fortin, D., Broman, C., Stampanoni, M., 2013. Fossilized iron bacteria  
1104 reveal a pathway to the biological origin of banded iron formation. *Nature*  
1105 *Comms* 4:2050. DOI: 10.1038/ncomms3050.

1106 Chi Fru, E., Arvestål, E., Callac, N., El Albani, A., Kiliass, S., Argyraki, A., and  
1107 Jakobsson, M., 2015a. Arsenic stress after the Proterozoic glaciations. *Sci.*  
1108 *Rep.* 5:17789. DOI: 10.1038/srep17789.

1109 Chi Fru, E., Ivarsson., M, Kiliass. S.P, Frings, P.J., Hemmingsson, C., Broman,  
1110 C., Bengtson, S., Chatzitheodoridis, E., 2015b. Biogenicity of an Early  
1111 Quaternary iron formation, Milos Island, Greece. *Geobiology* 13:225-244.  
1112 <https://doi.org/10.1111/gbi.12128>.

1113 Chi Fru, E., Rodríguez, N.P., Partin, C.A., Lalonde, S.V., Andersson, P., Weiss,  
1114 D.J., El Albani, A., Rodushkin, I., and Konhauser, K.O., 2016a. Cu isotopes  
1115 in marine black shales record the Great Oxidation Event. *Proc. Natl. Acad.*  
1116 *Sci. U.S.A.* 113:4941–4946. <https://doi.org/10.1073/pnas.1523544113>.



1117 Chi Fru, E., Hemmingsson, C., Holm, M., Chiu, B., Iñiguez E., 2016b. Arsenic-  
 1118 induced phosphate limitation under experimental Early Proterozoic  
 1119 oceanic conditions. *Earth Planet. Sci. Letts.* 434:52–63.  
 1120 <https://doi.org/10.1016/j.epsl.2015.11.009>.  
 1121 Chi Fru, E., Kiliass, S., Ivarsson, M., Rattray, J.E., Gkika, K., McDonald, I., He,  
 1122 Q., Broman, C., 2018a. Sedimentary mechanisms of a modern banded  
 1123 iron formation on Milos Island, Greece. *Solid Earth* 9:573–598.  
 1124 <https://doi.org/10.5194/se-9-573-2018>.  
 1125 Chi Fru, F., Callac, N., Posth, N.R., Argyraki, A., Ling, Y.-C., Ivarsson, M.,  
 1126 Broman, C., Kiliass, S.P., 2018b. Arsenic and high affinity phosphate  
 1127 uptake gene distribution in shallow submarine hydrothermal sediments.  
 1128 *Biogeochemistry* 141:41–62. <https://doi.org/10.1007/s10533-018-0500-8>.  
 1129 Chi Fru, E., Somogyi, A., El Albani, A., Medjoubi, K., Aubineau, J., Robbins,  
 1130 L.J., Lalonde, S.V., and Konhauser, K.O., 2019. The rise of oxygen-driven  
 1131 arsenic cycling at ca. 2.48 Ga. *Geology* 47:243–246.  
 1132 <https://doi.org/10.1130/G45676.1>.  
 1133 Choubert, G., 1947. L'accident majeur de l'Anti-Atlas, C.R. Acad. Sci. Paris,  
 1134 224:1172–1173.  
 1135 Clarkson, M.O., Poulton, S.W., Guilbaud, R., Wood, R.A., 2014. Assessing the  
 1136 utility of the Fe/Al and Fe-speciation to record water column redox  
 1137 conditions in carbonate-rich sediments. *Chem. Geol.* 382:111–122.  
 1138 <https://doi.org/10.1016/j.chemgeo.2014.05.031>.  
 1139 Conway, T.M., John, S.G., 2014. Quantification of dissolved iron sources to the  
 1140 North Atlantic ocean. *Nature* 511:212–215. DOI:10.1038/nature12382.  
 1141 Conway, T.M., John, S.G., 2015. The cycling of iron, zinc and cadmium in the  
 1142 North East Pacific Ocean-Insights from stable isotopes. *Geochim. Cosmo.*  
 1143 *Acta* 164:262–283. <https://doi.org/10.1016/j.gca.2015.05.023>.  
 1144 Cox, G.M., Halverson, G.P., Minarik, W.G., Le Heron, D.P., Macdonald, F.A.  
 1145 Bellefroid, E.J. Strauss, J.V., 2013. Neoproterozoic iron formation: An  
 1146 evaluation of its temporal, environmental and tectonic significance. *Chem.*  
 1147 *Geol.* 362:232–249. <https://doi.org/10.1016/j.chemgeo.2013.08.002>.  
 1148 Craddock, P.R., Bach, W., Seewald, J.S., Rouxel, O.J. Reeves, E, Tivey, M.K.,  
 1149 2010. Rare earth element abundances in hydrothermal fluids from the  
 1150 Manus Basin, Papua New: Indicators of sub-seafloor hydrothermal

1151 processes in backarc basins. *Geochim. Cosmochim. Acta* 74:675–683.  
 1152 <https://doi.org/10.1016/j.gca.2010.07.003>.

1153 Craddock, P.R., Dauphas, N., 2011. Iron and carbon isotope evidence for  
 1154 microbial iron respiration throughout the Archean. *Earth Planet. Sci. Letts.*  
 1155 303:121–132. <https://doi.org/10.1016/j.epsl.2010.12.045>.

1156 Dauphas, N., John, S.G., Rouxel, O., 2016. Iron isotope systematics. *Rev. Min.*  
 1157 *Geochem.* 82:415–510. <http://dx.doi.org/10.2138/rmg.2017.82.11>.

1158 Dellwig, O., Wegwerth, W., Schnetger, B., Schulz, H., Arz H.W., 2019.  
 1159 Dissimilar behaviors of the geochemical twins W and Mo in hypoxic-euxinic  
 1160 marine basins. *Earth-Sci. Rev.* 193:1–23.  
 1161 <https://doi.org/10.1016/j.earscirev.2019.03.017>.

1162 Douville E., Bienvenu P., Charlou J. L., Donval J. P., Fouquet Y., Appriou P.  
 1163 and Gamo T., 1999. Yttrium and rare earth elements in fluids from various  
 1164 deep-sea hydrothermal systems. *Geochim. Cosmochim. Acta* 63:627–  
 1165 643. [https://doi.org/10.1016/S0016-7037\(99\)00024-1](https://doi.org/10.1016/S0016-7037(99)00024-1).

1166 Douville, E., Charlou, J.L., Oelkers, E.H., Bienvenu, P., C.F. Colon, J., Donval,  
 1167 J.P., Fouquet, Y., Prieur, D., Appriou, P., 2002. The rainbow vent fluids  
 1168 (3614VN, MAR): the influence of ultramafic rocks and phase separation on  
 1169 trace metal content in Mid-Atlantic Ridge hydrothermal fluids. *Chem. Geol.*  
 1170 184:37–48. [https://doi.org/10.1016/S0009-2541\(01\)00351-5](https://doi.org/10.1016/S0009-2541(01)00351-5).

1171 Dyhrman, S.T., Haley, S.T., 2011. Arsenate resistance in the unicellular marine  
 1172 Di <https://doi.org/10.3389/fmicb.2011.00214>.

1173 Dymek, R.F., Klein, C., 1988. Chemistry, petrology and origin of banded iron-  
 1174 formation lithologies from the 3800 MA isua supracrustal belt, West  
 1175 Greenland. *Pre. Res.* 39:247–302. [https://doi.org/10.1016/S0009-](https://doi.org/10.1016/S0009-2541(01)00351-5)  
 1176 [2541\(01\)00351-5](https://doi.org/10.1016/S0009-2541(01)00351-5).

1177 Elderfield H. and Schultz A., 1996. Mid-ocean ridge hydrothermal fluxes and  
 1178 the chemical composition of the ocean. *Annu. Rev. Earth Planet. Sci.*  
 1179 24:191–224. <https://doi.org/10.1146/annurev.earth.24.1.191>.

1180 El Hadi, H., Simancas, J.F., Martinez-Poyatos, D., Azor, A., Tahiri, A., Montero,  
 1181 P., Fanning, C.M., Bea, F., Gonzalez-Lodeiro, F., 2010. Structural and  
 1182 geochronological constraints on the evolution of the Bou Azzer  
 1183 Neoproterozoic ophiolite (Anti-Atlas, Morocco). *Pre. Res.* 182:1–14.  
 1184 <https://doi.org/10.1016/j.precamres.2010.06.011>.

1185 Ennih, N., Liégeois, J.-P., 2001. The Moroccan Anti-Atlas: the West African  
 1186 craton passive margin with limited Pan-African activity. Implications for the  
 1187 northern limit of the craton. *Pre. Res.* 112:289–302.  
 1188 [https://doi.org/10.1016/S0301-9268\(01\)00195-4](https://doi.org/10.1016/S0301-9268(01)00195-4).

1189 Ennih, N., Liégeois, J.P., 2008. The boundaries of the West African craton, with  
 1190 special reference to the basement of the Moroccan metacratonic Anti-Atlas  
 1191 belt. *Geological Society London, Special Publication* 297:1–17.  
 1192 <https://doi.org/10.1144/SP297.1>.

1193 Evans, D.A.D., Trindade, R.I.F., Catelani, E.L., D'Agrella-Filho, M.S., Heaman,  
 1194 L.M., Oliveira, E.P., Söderlund, U., Ernst, R.E., Smirnov, A.V., Salminen,  
 1195 J.M., 2016. Return to Rodinia? Moderate to high palaeolatitude of the São  
 1196 Francisco/Congo craton at 920 Ma. *Geological Society London, Special*  
 1197 *Publication* 424:167–190. <https://doi.org/10.1144/SP424.1>.

1198 Feely, R. A., Trefry, J. H., Lebon, G. T., German C. R., 1998. The relationship  
 1199 between P/Fe and V/Fe ratios in hydrothermal precipitates and dissolved  
 1200 phosphate in seawater. *Geophy. Res. Lett.* 15:2253–2256.  
 1201 <https://doi.org/10.1029/98GL01546>.

1202 Feely, R. A., Trefry, J. H., Massoth, G. J., Metz, S. A., 1991. Comparison of the  
 1203 scavenging of phosphorus and arsenic from seawater by hydrothermal iron  
 1204 oxyhydroxides in the Atlantic and Pacific Oceans. *Deep-Sea Res.* 38:617–  
 1205 623. [https://doi.org/10.1016/0198-0149\(91\)90001-V](https://doi.org/10.1016/0198-0149(91)90001-V).

1206 Fischer, W.W., Knoll, H.A., 2009. An iron shuttle for deepwater silica in Late  
 1207 Archean and early Paleoproterozoic iron formation. *GSA Bulletin*:  
 1208 121:222–235. <https://doi.org/10.1130/B26328.1>.

1209 Fitzsimmons J N., Boyle E.A., Jenkins W.J., 2014. Distal transport of dissolved  
 1210 hydrothermal iron in the deep South Pacific Ocean. *Proc. Natl. Acad. Sci.*  
 1211 *U.S.A.* 111:16654–16661. <https://doi.org/10.1073/pnas.1418778111>.

1212 Fitzsimmons J.N., Conway T.M., Lee J. M., Kayser R., Thyng K.M., John S. G.,  
 1213 Boyle E.A., 2016, Dissolved iron and iron isotopes in the southeastern  
 1214 Pacific Ocean. *Glob. Biogeochem. Cycl.* 30:1372–1395.  
 1215 <https://doi.org/10.1002/2015GB005357>.

1216 Fitzsimmons J.N., John S.G., Marsay C.M., Hoffman C.L., Nicholas S.L., Toner  
 1217 B.M., German C.R. and Sherrell R.M., 2017. Iron persistence in a distal  
 1218 hydrothermal plume supported by dissolved-particulate exchange. *Nat.*

1219 Geosci. 10:U195–U150. <https://doi.org/10.1038/ngeo2900>.

1220 Frei, R., Dahl, P.S., Duke, E.F., Frei, K.M., Rintza, H., Frandsson, M.M.,  
 1221 Jensen, L.A., 2008. Trace element and isotopic characterization of  
 1222 Neoarchean and Paleoproterozoic iron formations in the Black Hills (South  
 1223 Dakota, USA): Assessment of chemical change during 2.9-1.9 Ga  
 1224 deposition bracketing the 2.4-2.2 Ga first rise of atmospheric oxygen. *Pre.*  
 1225 *Res.* 162:441–474. <https://doi.org/10.1016/j.precamres.2007.10.005>.

1226 Gartman, A., Findlay, A.J., 2020. Impacts of hydrothermal plume processes on  
 1227 oceanic metal cycles and transport. *Nat. Geosci.* 13:396–402.

1228 German, C.R., and Seyfried, W.E., Jr., 2014. Hydrothermal processes. In  
 1229 *Treatise on Geochemistry*, 2nd edn. Oxford, Elsevier, Vol. 8, pp. 191–233.

1230 Giovannoni, S.J., Halsey, K.H., Saw, J., Muslin, O., Suffridge, C.P., Sun, J.,  
 1231 Lee, C.-P., Moore, E.R., Temperton, B., Noell, S.E., 2019. A parasitic  
 1232 arsenic cycle that shuttles energy from phytoplankton to heterotrophic  
 1233 bacterioplankton. *mBio* 10:e00246-19. doi:10.1128/mBio.00246-19.

1234 Guilbaud, R., Poulton, S.W., Thompson, J., Husband, K.F., Zhu, M., Zhou, Y.,  
 1235 Shields, G.A., Lenton, T.M., 2020. Phosphorus-limited conditions in the  
 1236 early Neoproterozoic ocean maintained low levels of atmospheric oxygen.  
 1237 *Nat. Geosci.* 13:296–30. <https://doi.org/10.1038/s41561-020-0548-7>.

1238 Halverson, G.P., Poitrasson, F., Hoffman, P.F., Nédélec, A., Montel, J.-M.,  
 1239 Kirby, J., 2011. Fe isotope and trace elements geochemistry of the  
 1240 Neoproterozoic syn-glacial Rapitan iron formation. *Earth Planet. Sci. Letts.*  
 1241 309:100–112. <https://doi.org/10.1016/j.epsl.2011.06.021>.

1242 Hugaard, R., Pecoits, E., Lalonde, S., Rouxel, O., Konhauser, K., 2016. The  
 1243 Joffre banded iron formation, Hammersley Group, Western Australia:  
 1244 Assessing the palaeoenvironment through detailed petrology and  
 1245 chemostratigraphy. *Pre. Res.* 273:12–37.  
 1246 <https://doi.org/10.1016/j.precamres.2015.10.024>.

1247 Heard, A.W., Dauphas, N., 2020. Constraints on the coevolution of oxic and  
 1248 sulfidic ocean iron sinks from Archean–Paleoproterozoic iron isotope  
 1249 records. *Geology* 48:58–362. <https://doi.org/10.1130/G46951.1>.

1250 Heimann, A., Johnson, C.M., Beard, B.L., Valley, J.W., Roden, E.E., Spicuzza,  
 1251 M.J., Beukes, N.J., 2010. Fe, C, and O isotope compositions of banded  
 1252 iron formation carbonates demonstrate a major role for dissimilatory iron

1253 reduction in ~2.5 Ga marine environments. *Earth Planet. Sci. Letts.* 294:8–  
 1254 18. <https://doi.org/10.1016/j.epsl.2010.02.015>.

1255 Hemmingsson, C., Pitcairn, I.K., Chi Fru, C., 2018. Evaluation of phosphate-  
 1256 uptake mechanisms by Fe (III)(oxyhydr) oxides in Early Proterozoic  
 1257 oceanic conditions. *Environ. Chem.* 15:18–28.  
 1258 <https://doi.org/10.1071/EN17124>.

1259 Hoffman, P.F., Abbot, D.S., Ashkenazy, Y., Benn, D.I., Brocks, J., Coheren,  
 1260 P.A., Cox, G.M., Creveling, J.R., Erwin, D.H., Fairchild, I.J., Ferreira, D.,  
 1261 Goodman, J.C., Haverson, G.P., Jansen, M.F., Fe Hir, G., Love, G.D.,  
 1262 Macdonald, F.A., Maloof, A.C., Partin, A.C., Ramstein, G., Rose, B.E.J.,  
 1263 Rose, C.V., Sadler, P.M., Tziperman, E., Voigt, A., Warren, S.G., 2017.  
 1264 Snowball Earth climate dynamics and Cryogenian geology-geobiology.  
 1265 *Sci. Adv.* 3:e1600983. DOI:10.1126/sciadv.1600983.

1266 Hefferan, K.P., Admou H., Karson, J.A., Saquaque, A., 2000. Anti-Atlas  
 1267 (Morocco) role in Neoproterozoic Western Gondwana reconstruction. *Pre.*  
 1268 *Res.* 103:89–96. [https://doi.org/10.1016/S0301-9268\(00\)00078-4](https://doi.org/10.1016/S0301-9268(00)00078-4).

1269 Inglis, J.D., D’Lemos, R.S., Samson, S.D., Admou, H., 2005. Geochronological  
 1270 constraints on Late Precambrian intrusion, metamorphism, and tectonism  
 1271 in the Anti-Atlas mountains. *The J. Geol.* 113:439–450.  
 1272 <https://doi.org/10.1086/430242>.

1273 Jessell, M.W., Begg, G.C., Miller, M.S., 2016. The geophysical signatures of  
 1274 the West African craton. *Prec. Res.* 274:3–24.  
 1275 <https://doi.org/10.1016/j.precamres.2015.08.010>.

1276 Kerrich, R., Said, N., Manikyamba, C., Wyman, D., 2013. Sampling oxygenated  
 1277 Archean hydrosphere: Implications from fractionations of Th/U and Ce/Ce\*  
 1278 in hydrothermally altered volcanic sequences. *Gond. Res.* 23:506–525.  
 1279 <https://doi.org/10.1016/j.gr.2012.02.007>.

1280 Keyser, W., Ciobanu, C.L., Cook, N.J., Johnson, G., Feltus, H., Johnson, S.,  
 1281 Dmitrijeva, M., Ehrig, K., Nguyen, P.T., 2018. Petrography and trace  
 1282 element signatures of iron-oxides in deposits from the middleback Ranges,  
 1283 South Australia: From banded iron formation to ore. *Ore Geol. Rev.*  
 1284 93:337–360. <https://doi.org/10.1016/j.oregeorev.2018.01.006>.

1285 Klein, C., Beukes, N.J., 1993. Sedimentology and geochemistry of the  
 1286 glaciogenic late Proterozoic Rapitan Iron-Formation in Canada. *Econ.*

1287 Geol. 88:542–565. <https://doi.org/10.2113/gsecongeo.88.3.542>.  
 1288 Klinkhammer, G.P., Elderfield, H., Edmond, J.M., Mitra, A., 1994. Geochemical  
 1289 implications of rare earth element patterns in hydrothermal fluids from mid-  
 1290 ocean ridges. *Geochim. Cosmochim. Acta* 58:5105–5113.  
 1291 [https://doi.org/10.1016/0016-7037\(94\)90297-6](https://doi.org/10.1016/0016-7037(94)90297-6).  
 1292 Konhauser, K.O., Hamade, T., Raiswell, R., Morris, R.C., Ferris, F.G.,  
 1293 Southam, G., Canfield, D.E., 2002. Could bacteria have formed the  
 1294 Precambrian banded iron formations? *Geology* 30:1079–1082.  
 1295 [https://doi.org/10.1130/0091-7613\(2002\)030<1079:CBHFTP>2.0.CO;2](https://doi.org/10.1130/0091-7613(2002)030<1079:CBHFTP>2.0.CO;2).  
 1296 Konhauser, K.O., Planavsky, N.J., Hardisty, D.S., Robbins, L.J., Warchola,  
 1297 T.J., Haugaard, R., Lalonde, S.V., Partin, C.A., Oonk, P.B.H., Tsikos, H.,  
 1298 Lyons, T.W., Bekker, A., Johnson, C.M., 2017. Iron formations: A global  
 1299 record of Neoarchaeon to Palaeoproterozoic environmental history. *Earth-*  
 1300 *Sci. Rev.* 172:140–177. <https://doi.org/10.1016/j.earscirev.2017.06.012>.  
 1301 Large, R.R., Halpin, J.A., Lounejeva, E., Danyushevsky, L.V., Maslennikov,  
 1302 V.V., Gregory, D., Sack, P.J., Haines, P.W., Long, J.A., Makoundi, C.,  
 1303 Stepanov, S., 2015. Cycles of nutrient trace elements in the Phanerozoic  
 1304 ocean. *Gond. Res.* 28:1282–1293.  
 1305 <https://doi.org/10.1016/j.gr.2015.06.004>.  
 1306 Leblanc, M., Lancelot, J., 1980. Interprétation géodynamique du domaine Pan-  
 1307 Africain de l'Anti-Atlas (Maroc) à partir de données géologiques et  
 1308 géochronologiques. *Can. J. Earth Sci.* 17:142–155.  
 1309 <https://doi.org/10.1139/e80-012>.  
 1310 Lechte, M. A., Wallace, M., van Smeerdijk Hood, A., Planavsky, N. 2018.  
 1311 Cryogenian iron formations in the glaciogenic Kingston Peak Formation,  
 1312 California. *Pre. Res.* 310:443-462.  
 1313 <https://doi.org/10.1016/j.precamres.2018.04.003>.  
 1314 Lough, A. J. M., Klar, J. K., Homoky, W. B., Comer-Warner, S. A., Milton, J. A.,  
 1315 Connelly, D.P., James, R.H., Mills, R.A., 2017. Opposing authigenic  
 1316 controls on the isotopic signature of dissolved iron in hydrothermal plumes.  
 1317 *Geochim. Cosmochim. Acta* 202:1–20.  
 1318 <https://doi.org/10.1016/j.gca.2016.12.022>.  
 1319 Lough, A.J.M. Homoky, W.B., Connelly, D.P., Comer-Warner, S.A., Nakamura,  
 1320 K., Abyaneh, M.K., Kaulich, B., Mills, R.A., 2019. Soluble iron conservation

1321 and colloidal iron dynamics in a hydrothermal plume. *Chem.*  
1322 *Geol.* 511:225–237. <https://doi.org/10.1016/j.chemgeo.2019.01.001>.

1323 Lyons, T. W., Reinhard, C. T., and Planavsky, N. J., 2014. The rise of oxygen  
1324 in Earth's early ocean and atmosphere. *Nature* 506:307–315.  
1325 DOI:10.1038/nature13068.

1326 Manikyamba, C., Said, N., Santosh, M., Saha, A., Ganguly, S., Subramanyam,  
1327 K.S.V., 2018. U enrichment and Th/U fractionation in Archean boninites:  
1328 Implications for paleo-ocean oxygenation and U cycling at juvenile  
1329 subduction zones. *J. Asian Earth Sci.* 157:187–197.  
1330 <https://doi.org/10.1016/j.jseaes.2017.10.009>.

1331 McLennan, S.M., 1989. Rare Earth elements in sedimentary rocks: Influence of  
1332 provenance and sedimentary processes. In: Lipin, B., McKay, G. (Eds.),  
1333 *Geochemistry and mineralogy of the Rare Earth Elements: Mineralogical*  
1334 *Society of America*, pp. 169–200.

1335 McLennan, S.M., 2001. Relationships between the trace element composition  
1336 of sedimentary rocks and upper continental crust. *Geochem. Geophys.*  
1337 *Geosyt.* 2: <https://doi.org/10.1029/2000GC000109>.

1338 Millet, M.-A., Baker, J.A., Payne, C.E., 2012. Ultra-precise stable Fe isotope  
1339 measurements by high resolution multiple-collector inductively coupled  
1340 plasma mass spectrometry with a  $^{57}\text{Fe}$ – $^{58}\text{Fe}$  double spike. *Chem. Geol.*  
1341 304-305:18–25. <https://doi.org/10.1016/j.chemgeo.2012.01.021>

1342 Mitra A., Elderfield H. and Greaves M. J., 1994. Rare earth elements in  
1343 submarine hydrothermal fluids and plumes from the Mid-Atlantic Ridge.  
1344 *Marine Chem.* 46:217–235. [https://doi.org/10.1016/0304-4203\(94\)90079-](https://doi.org/10.1016/0304-4203(94)90079-5)  
1345 5.

1346 Mohajerin, T.J., Helz, G.R., Johannesson, K.H., 2016. Tungsten–molybdenum  
1347 fractionation in estuarine environments. *Geochim. Cosmo. Acta* 117:105–  
1348 119. <https://doi.org/10.1016/j.gca.2015.12.030>.

1349 Mondillo, N., Balassone G., Boni, M., Chelle-Michou C., Cretella S., Mormone,  
1350 A., Putzolu F., Santoro, F., Scognamiglio, G., Tarallo, M., 2019. Rare Earth  
1351 Elements (REE) in Al- and Fe-(oxy)-hydroxides in bauxites of provence  
1352 and Languedoc (Southern France): Implications for the potential recovery  
1353 of REEs as by-products of bauxite mining. *Minerals* 9:504.  
1354 <https://doi.org/10.3390/min9090504>.

1355 Mukherjee, I., Large, R.R., Bull, S., Gregory, D.G., Stepanov, A.S., Ávila, J.,  
1356 Ireland, T.R., Corkrey, R., 2019. Pyrite trace-element and sulfur isotope  
1357 geochemistry of paleo-mesoproterozoic McArthur Basin: Proxy for  
1358 oxidative weathering. *Am. Min.* 104:1256–1272.  
1359 <https://doi.org/10.2138/am-2019-6873>.

1360 Ganno, S., Laure, N.T.E., Djibril, K.N.G., Arlette, D.S., Cyriel, M., Timoléon, N.,  
1361 Paul, N.J., 2017. A mixed seawater and hydrothermal origin of superior-  
1362 type banded iron formations (BIF)-hosted Kouambo iron deposit,  
1363 Paleoproterozoic Nyong Series Southwestern Cameroon: Constraints  
1364 petrography and geochemistry. *Ore Geol.* 80:860–875.  
1365 <https://doi.org/10.1016/j.oregeorev.2016.08.021>.

1366 Gartman, A., Findlay, A.J., 2020. Impacts of hydrothermal plume processes on  
1367 oceanic metal cycles and transport. *Nat. Geosci.* 13:396–402.  
1368 DOI:10.1038/s41561-020-0579-0.

1369 Percoits, E., Gingras, M.K., Barley, M.E., Kappler, A., Posth, N.R., Konhauser,  
1370 K.O., 2009. Petrography and geochemistry of the Dales Gorge banded iron  
1371 formation: Paragenetic sequence, source and implications for palaeo-  
1372 ocean chemistry. *Pre. Res.* 72:163–187.  
1373 <https://doi.org/10.1016/j.precamres.2009.03.014>.

1374 Planavsky, N., Bekker, A., Rouxel, O.J., Kamber, B., Hofmann, A., Knudsen,  
1375 A., Lyons, T.W., 2010. Rare Earth Element and Yttrium compositions of  
1376 Archean and Paleoproterozoic Fe formations revisited: new perspectives  
1377 on the significance and mechanisms of deposition. *Geochim. Cosmochim.*  
1378 *Acta* 74:6387–6405. <https://doi.org/10.1016/j.gca.2010.07.021>.

1379 Planavsky, N., Rouxel, O., Bekker, A., Hofmann, A., Little, C.T.S., Lyons., 2012.  
1380 Iron isotope composition of some Archean and Proterozoic iron formations.  
1381 *Geochim. Cosmo. Acta* 80:158–169.  
1382 <http://dx.doi.org/10.1016/j.gca.2011.12.001>.

1383 Poulton, S.W., Krom, M.D., Raiswell, R., 2004. A revised scheme for the  
1384 reactivity of iron (oxyhydr)oxide minerals towards dissolved sulfide.  
1385 *Geochim. Cosmochim. Acta* 68:3703–3715.  
1386 <https://doi.org/10.1016/j.gca.2004.03.012>.

1387 Poulton, S.W., Canfield, D.E., 2005. Development of a sequential extraction  
1388 procedure for iron: Implications for iron partitioning in continentally derived



1389 particulates. Chem. Geol. 214:209–221.  
 1390 <https://doi.org/10.1016/j.chemgeo.2004.09.003>.  
 1391 Poulton, S.W., Canfield, D.E., 2011. Ferruginous Conditions: A dominant  
 1392 feature of the ocean through Earth's history. *Elements* 7:107–112.  
 1393 <https://doi.org/10.2113/gselements.7.2.107>.  
 1394 Radic A., Lacan, F., Murray, J.W., 2011. Iron isotopes in the seawater of the  
 1395 equatorial Pacific Ocean: New constraints for the oceanic iron cycle. *Earth*  
 1396 *and Planet. Sci. Letts.* 306:1–10.  
 1397 <https://doi.org/10.1016/j.epsl.2011.03.015>.  
 1398 Raiswell, R., Hardisty, D.S., Lyons, T.W., Canfield, D.E., Owens, J.D.,  
 1399 Planavsky, N.J., Poulton, S.W., Reinhard, C.T., 2018. The iron paleoredox  
 1400 proxies: A guide to the pitfalls, problems and proper practice. *Am. J.*  
 1401 *Sci.* 318:491–526. DOI: <https://doi.org/10.2475/05.2018.03>.  
 1402 Reinhard, C.T., Planavsky, N.J., Robbins, L.J., Partin, C.A., Gill, B.C., Lalonde,  
 1403 S.V., Bekker, A., Konhauser, K.O., Lyong, T.W., 2013. Proterozoic ocean  
 1404 redox and biogeochemical stasis. *Proc. Natl. Acad. Sci. U.S.A.* 110:5357–  
 1405 5362. <https://doi.org/10.1073/pnas.1208622110>.  
 1406 Reinhard, C.T., Planavsky, N.J., Gill, B.C., Ozaki, K., Robbins, L.J., Lyons,  
 1407 T.W., Fischer, W.W., Wang, C., Cole, D.B., Konhauser, K.O., 2017.  
 1408 Evolution of the global phosphate cycle. *Nature* 541:386–389.  
 1409 DOI:10.1038/nature20772.  
 1410 Resing J. A., Sedwick P. N., German C. R., Jenkins W. J., Moffett J. W., Sohst  
 1411 B. M. and Tagliabue A., 2015. Basin-scale transport of hydrothermal  
 1412 dissolved metals across the South Pacific Ocean. *Nature* 523:U140–U200.  
 1413 Robbins, L.J., Konhauser, K.O., Warchola, T.J., Homann, M., Thoby, M.,  
 1414 Foster, I., Mloszewska, A.M., Alessi, D.S., Lalonde, S.V., 2019. A  
 1415 comparison of bulk versus laser ablation trace element analysis in banded  
 1416 iron formations: Insights into the mechanisms leading to compositional  
 1417 variability. Chem. Geol. 506:197–224.  
 1418 <https://doi.org/10.1016/j.chemgeo.2018.12.036>.  
 1419 Rouxel, O., Dobbek, N., Ludden, J., Fouquet, Y., 2003. Iron isotope  
 1420 fractionation during oceanic crust alteration. *Chem. Geol.* 202:155–182.  
 1421 <https://doi.org/10.1016/j.chemgeo.2003.08.011>.  
 1422 Rouxel, O.J., Bekker, A., Edwards, K.J., 2005. Iron isotope constraints on the

1423 Archean and Paleoproterozoic ocean redox state. *Science* 307:1088–  
 1424 1091. <http://dx.doi.org/10.1126/science.1105692>.

1425 Rouxel, O., Shanks Iii, W.C., Bach, W., Edwards, K.J., 2008. Integrated Fe-  
 1426 and S-isotope study of seafloor hydrothermal vents at East Pacific rise 9-  
 1427 10°N. *Chem. Geol.* 252:214–227.  
 1428 <https://doi.org/10.1016/j.chemgeo.2008.03.009>.

1429 Rouxel, O., Toner, B.M., Manganini, S.J., German, C.R., 2016. Geochemistry  
 1430 and iron isotope systematics of hydrothermal plume fall-out at East Pacific  
 1431 Rise 9°50'N. *Chem. Geol.* 441:212–234.  
 1432 <https://doi.org/10.1016/j.chemgeo.2016.08.027>.

1433 Rouxel, O., Toner, B., Germain, Y., Glazer, B., 2018. Geochemical and iron  
 1434 isotopic insights into hydrothermal iron oxyhydroxide deposit formation at  
 1435 Loihi Seamount. *Geochim. Cosmo. Acta* 220:449-482.  
 1436 <https://doi.org/10.1016/j.gca.2017.09.050>.

1437 Sander, S. G. & Koschinsky, A., 2011. Metal flux from hydrothermal vents  
 1438 increased by organic complexation. *Nat. Geosci.* 4:145–150.

1439 Saunders, J.K., Rocap, G., 2016. Genomic potential for arsenic efflux and  
 1440 methylation varies among global *Prochlorococcus* populations. *The ISME*  
 1441 *J.* 10:197–209.

1442 Saquaque, A., Admou, H., Karson, J.A., Hefferan, K.P., Reuber, I., 1989.  
 1443 Precambrian accretionary tectonics in the Bou-Azzer El Graara region,  
 1444 Anti-Atlas. *Geology* 17:1107–1110. [http://dx.doi.org/10.1130/0091-](http://dx.doi.org/10.1130/0091-7613(1989)017<1107:PATITB>2.3.CO;2)  
 1445 [7613\(1989\)017<1107:PATITB>2.3.CO;2](http://dx.doi.org/10.1130/0091-7613(1989)017<1107:PATITB>2.3.CO;2).

1446 Schofield, D.I., Horstwood, M.S.A., Pitfield, P.E.J., Crowley, Q.G., Wilkinson,  
 1447 A.F., Sidaty, H.C.O., 2006. Timing and kinematics of Eburnean tectonics  
 1448 in the central Reguibat shield, Mauritania. *J. Geol. Soc.* 163:549–560.  
 1449 <https://doi.org/10.1144/0016-764905-097>.

1450 Schrag, D.P., Higgins, J.A., Macdonald, F.A., Johnston, D.T., 2013. Authigenic  
 1451 carbonate and the history of the global carbon cycle. *Science* 339:540–  
 1452 543. DOI: 10.1126/science.1229578.

1453 Scott C, Lyons TW, Bekker A, Shen Y, Poulton SW, Chu X, Anbar AD., 2008.  
 1454 Tracing the stepwise oxygenation of the Proterozoic ocean. *Nature*  
 1455 452:456–459. DOI:10.1038/nature06811.

1456 Scott, C., Lyons, T.W., 2012. Contrasting molybdenum cycling and isotopic

1457 properties in euxinic versus non-euxinic sediments and sedimentary rocks:  
 1458 Refining the paleoproxies. *Chem. Geol.* 324–325:19–27.  
 1459 <https://doi.org/10.1016/j.chemgeo.2012.05.012>.  
 1460 Severmann, M., Johnson, C.M., Beard, B.L., 2004. The effect of plume  
 1461 processes on the Fe isotope composition of hydrothermally derived Fe in  
 1462 the deep ocean as inferred from the Rainbow vent site, Mid-Atlantic Ridge,  
 1463 36°14'N. *Earth Planet. Sci. Letts.* 225:63–76.  
 1464 <http://dx.doi.org/10.1016/j.epsl.2004.06.001>.  
 1465 Severmann, S., Lyons, T.W., Anbar, A., McManus, J., Gordon, G., 2008.  
 1466 Modern iron isotope perspective on the benthic iron shuttle and the redox  
 1467 evolution of ancient oceans. *Geology* 36:487–490.  
 1468 <https://doi.org/10.1130/G24670A.1>.  
 1469 Sharma, M., Polizzotto, M., Anbar, A.D., 2001. Iron isotope in hot spring along  
 1470 the Juan de Fuca Ridge. *Earth Planet. Sci. Letts.* 194:39–51.  
 1471 [https://doi.org/10.1016/S0012-821X\(01\)00538-6](https://doi.org/10.1016/S0012-821X(01)00538-6).  
 1472 Shields, G.A., Webb, G.E., 2004. Has the REE composition of seawater  
 1473 changed over geological time? *Chem. Geol.* 204:103–107.  
 1474 <https://doi.org/10.1016/j.chemgeo.2003.09.010>.  
 1475 Shields, G.A., Mills, B.J., 2017. Tectonic controls on the long-term carbon  
 1476 isotope mass balance. *Proc. Natl. Acad. Sci. U.S.A.* 114:4318–4323.  
 1477 <https://doi.org/10.1073/pnas.1614506114>.  
 1478 Singh, P., Rajamani, V., 2001. REE geochemistry of recent clastic sediments  
 1479 from the Kaveri floodplains, southern India: Implication to source area  
 1480 weathering and sedimentary processes. *Geochim. Cosmochim. Acta*  
 1481 65:3093–3108. [https://doi.org/10.1016/S0016-7037\(01\)00636-6](https://doi.org/10.1016/S0016-7037(01)00636-6).  
 1482 Smedley P.L., Kinniburgh, D.G., 2002. A review of the source, behaviour and  
 1483 distribution of arsenic in natural waters. *Appl. Geochem.* 17:517–568.  
 1484 [https://doi.org/10.1016/S0883-2927\(02\)00018-5](https://doi.org/10.1016/S0883-2927(02)00018-5).  
 1485 Song, H., Jiang, G., Poulton, S. W., Wignall, P. B., Tong, J., Song, H., An, Z.,  
 1486 Chu, D., Tian, L., She, Z., Wang, C., 2017. The onset of widespread marine  
 1487 red beds and the evolution of ferruginous oceans. *Nat. Comms.* 8:399.  
 1488 |DOI: 10.1038/s41467-017-00502-x.  
 1489 Sperling, E.A., Wolock, C.J., Morgan, A.S., Gill, B.C., Kunzmann, M.,  
 1490 Halverson, G.P., Macdonald, F.A., Knoll1, A.H., Johnston, D.T., 2015.

1491 Statistical analysis of iron geochemical data suggests limited late  
 1492 Proterozoic oxygenation. *Nature* 523:451–454. DOI:10.1038/nature14589.  
 1493 Stokey, L., 1970. Ferrozine—a new spectrophotometric reagent for iron. *Anal.*  
 1494 *Chem.* 42:779–781. <https://doi.org/10.1021/ac60289a016>.  
 1495 Stüeken, E. E. Kipp, M., Koehler, M. C., Buick, R. 2016. The evolution of Earth's  
 1496 biogeochemical nitrogen cycle. *Earth-Sci. Rev.* 160:220–239.  
 1497 <https://doi.org/10.1016/j.earscirev.2016.07.007>.  
 1498 Sun, Si., Konhauser, K.O., Kappler, A., Li, Y.-L., 2015. Primary hematite in  
 1499 Neoarchean to Paleoproterozoic oceans. *GSA Bulletin* 127:850–861.  
 1500 Thomas, R. J., Fekkak, A., Ennih, N., Errami, E., Loughlin, S.C., 2004. A new  
 1501 lithostratigraphic framework for the Anti-Atlas Orogen , Morocco. 39, 217–  
 1502 226. <https://doi.org/10.1016/j.jafrearsci.2004.07.046>.  
 1503 Thompson, K.J., Kenward, P.A., Bauer, K.W., Warchola, T., Gauger, T.,  
 1504 Martinez, R., Simister, R.L., Michiels, C.C., Llrós, M., Reinhard, C.T.,  
 1505 Kappler, A., Konhauser, K.O., Crowe, S.A., 2019. Photoferrotrophy,  
 1506 deposition of banded iron formations, and methane production in Archean  
 1507 oceans. *Science Advances* 5: eaav2869. DOI: 10.1126/sciadv.aav2869.  
 1508 Tivey, M.K., 2007. Generation of seafloor hydrothermal fluids and associated  
 1509 mineral deposits. *Oceanography* 20:50–65.  
 1510 <https://doi.org/10.5670/oceanog.2007.80>.  
 1511 Toner, B. M. Fakra, S.C., Manganini, S.J., Santelli, C.M., Marcus, M.A., Moffett,  
 1512 J.W., Rouxel, O., German, C.R., Edwards, K.J., 2009. Preservation of  
 1513 iron(II) by carbon-rich matrices in a hydrothermal plume. *Nat. Geosci.*  
 1514 2:197–201. DOI:10.1038/ngeo433.  
 1515 Tostevin, R., Shields, G.A., Tarbuck, G.M., He, T., Clarkson, M.O., Wood, R.A.,  
 1516 2016. Effective use of cerium anomalies as a redox proxy in carbonate-  
 1517 dominated marine settings. *Chemical Geology*, 438, 146-162.  
 1518 <https://doi.org/10.1016/j.chemgeo.2016.06.027>.  
 1519 Toth, J.R., 1980. Deposition of submarine crusts rich in manganese and iron.  
 1520 *Geol. Soc. Amer. Bull.* 91:52–60. [https://doi.org/10.1130/0016-](https://doi.org/10.1130/0016-7606(1980)91<44:DOSCRI>2.0.CO;2)  
 1521 [7606\(1980\)91<44:DOSCRI>2.0.CO;2](https://doi.org/10.1130/0016-7606(1980)91<44:DOSCRI>2.0.CO;2).  
 1522 Triantafyllou, A., Berger, J., Baele, J.-M., Diot, H., Ennih, N., Plissart, G.,  
 1523 Monnier, C., Watlet, A., Bruguier, O., Spagna, P., Vandycke, S., 2016. The  
 1524 Tachakoucht-Iriri-Tourtit arc complex (Moroccan Anti-Atlas):

1525 Neoproterozoic records of polyphased subduction accretion dynamics  
 1526 during the Pan-African orogeny. *J. Geody.* 96:81–103.  
 1527 <https://doi.org/10.1016/j.jog.2015.07.004>.

1528 Tribovillard, N., Algeo, T.J., Lyons, T., Riboulleau, A., 2006. Trace metals as  
 1529 paleoredox and paleoproductivity proxies: An update. *Chem. Geol.*  
 1530 232:12–32. <https://doi.org/10.1016/j.chemgeo.2006.02.012>.

1531 Visscher, P.T., Gallagher, K.L., Bouton, A., Farias, M.E., Kurth, D., Sancho-  
 1532 Tomás, M., Philippot, P., Somogyi, A., Medjoubi, K., Vennin, E., Bourillot,  
 1533 R., 2020. Modern arsenotrophic microbial mats provide an analogue for life  
 1534 in the anoxic Archean. *Comm. Earth Environ.* 1:24.  
 1535 <https://doi.org/10.1038/s43247-020-00025-2>.

1536 Wani, H., Mondal, M.E.A., 2011. Evaluation of provenance, tectonic setting and  
 1537 paleoredox conditions of the Meso-Neoproterozoic basins of the Bastar  
 1538 craton, Central Indian Shield: Using petrography of sandstones and  
 1539 geochemistry of shales. *Lithosphere* 3:143-154.  
 1540 <https://doi.org/10.1130/L74.1>.

1541 Weber, K.A., Achenbach, L.A., Coates, J.D., 2006. Microorganisms pumping  
 1542 iron: Anaerobic microbial iron oxidation and reduction. *Nature Rev.*  
 1543 *Microbiol.* 4:752–764. <http://dx.doi.org/10.1038/nrmicro1490>.

1544 Wu, D., Purnomo, B.J., Sun, S., 2017. As and Sb speciation in relation with  
 1545 physico-chemical characteristics of hydrothermal waters in Java and Bali.  
 1546 *J. Geochem. Exp.* 173:85–91.  
 1547 <https://doi.org/10.1016/j.gexplo.2016.12.003>.

1548 Wurl, O., Zimmer, L., Cutter, G.A., 2013. Arsenic and phosphorus  
 1549 biogeochemistry in the ocean: Arsenic species as proxies for P-limitation.  
 1550 *Limnol. Oceanogr.* 58: 729–740.  
 1551 <https://doi.org/10.4319/lo.2013.58.2.0729>.

1552 Yan, B., Zhu, Z.-K., Tang, S.-H., Zhu, M.-Y., 2010. Fe isotope characteristics of  
 1553 Neoproterozoic BIF in Guangxi Province and its implications. *Acta Geol.*  
 1554 *Sin.* 84:1080–1086.

1555 Yücel, M., Gartman, A., Chan, C. S., Luther, G. W., 2011. Hydrothermal vents  
 1556 as a kinetically stable source of iron-sulphide-bearing nanoparticles to the  
 1557 ocean. *Nat. Geosci.* 4:367–371. DOI:10.1038/ngeo1148.

1558 Zhang, X., Sigman, D.M., Morel, F.M.M., Kraepiel, A.M.L., 2014. Nitrogen

isotope fractionation by alternative nitrogenases and past ocean anoxia.  
Proc. Natl. Acad. Sci. U.S.A. 111:4782–4787.  
<https://doi.org/10.1073/pnas.1402976111>.

Zegeye, A., Bonneville, S., Benning, L.G., Sturm, A., Fowle, D.A., Jones, C.,  
Canfield, D.E., Ruby, C., MacLean, L.C., Nomosatryo, S., Crowe, S.A.,  
Poulton, S.W., 2012. Green-rust formation controls nutrient availability in a  
ferruginous water column. *Geology* 40:599–602.  
<https://doi.org/10.1130/G32959.1>.

Zeng, Z., Wang, X., Qi, H., Zhu, B., 2018. Arsenic and Antimony in  
Hydrothermal plumes from the Eastern Manus Basin, Papua New Guinea.  
*Geofluids* 6079586. <https://doi.org/10.1155/2018/6079586>.

Zhou, J.L., Li, X.H., Tang, G.Q., Gao, B.Y., Bao, Z.A., Ling, X.X., Wu, L.G., Lu,  
K., Zhu, Y.S., Liao, X., 2018. Ca. 890 Ma magmatism in the northwest  
Yangtze block, South China: SIMS U-Pb dating, in-situ Hf-O isotopes, and  
tectonic implications. *J. Asian Earth Sci.* 151, 101–111.  
<https://doi.org/10.1016/j.jseaes.2017.10.029>.

## Figure Legend

Fig. 1: Geological setting and structural units of the Proterozoic basement of  
the Anti-Atlas and location of the studied area. (a) Geological sketch map of the  
Proterozoic basement of the Anti-Atlas showing the three lithostructural  
domains and the studied area. SAFZ: South Atlas Fault Zone, AAFZ: Anti-Atlas  
Fault Zone; inset showing the location of the Anti-Atlas domain, (b) simplified  
map of the Pan-African craton margin strata in the central Anti-Atlas showing  
location of the studied section (Ag). TI: Taliwine, Tz: Tazenakht. (Modified from  
Bouougri et al, 2020).

Fig. 2. (a) Stratigraphic framework of the craton margin successions in the central part of the Anti-Atlas subdivided into Pre-Pan-African and Pan-African megacycles (Bouougri et al., 2016, modified from Bouougri and Saquaque, 2004). Key radiometric ages in blue and red from Bouougri et al. (2020). (b) Simplified measured section showing the sampled horizons including Fe-rich deposits of Wanimzi Fm. and clastic stromatolites of Imi n'Tizi Fm.

Fig. 3. Field features of Fe-bearing rocks of Wanimzi Formation: (a) General view within the upper part of Wanimzi Formation showing the transition from Fe-bearing interval with purple-red color and the overlying white interval without Fe. Dashed blue line indicates the sampled section. (b) Location of the sampled layers, numbered within the studied section shown in (a). (c) Detail within the sampled section showing several Fe-rich thin layers and interbeds consisting of storm deposits with Hummocky cross-stratification (HCS); scale 14.5 cm. (d) Thick Fe-rich and isolated storm bed occurring within heterolithic deposits. Hammer scale is 33 cm.

Fig. 4. Examples of sedimentary and microbial mat-related features of the siliciclastic Wanimzi and Imi n'Tizi Formations (e.g., Bouougri and Porada, 2002, Porada and Bouougri, 2007; Bouougri and Porada, 2011). (a-b) Sandstones with bedding planes showing symmetrical and asymmetrical ripples. (c) Kinneyia-type wrinkles occurring as patches on bedding surfaces of storm deposits. (d) Sand-filled spindle-shaped and randomly oriented cracks. (e) Mat-deformation structures occurring as curved and often bifurcating ridges. (f) Bedding surface preserving subrounded and flat sand clasts. (g-h) Siliciclastic biolamintes (stromatolites) showing domal features on bedding surface (h) and in cross section (g). Scale: (a-e-g) hammer is 33 cm long, (d-f) and (h) coin is 2.4 cm and 2 cm in diameter, respectively.

Fig. 5. Examples of thin section photomicrographs of sampled facies viewed in cross polarized light. (a) Siliciclastic microbial mats at the Imi n'Tizi shallow water stromatolite-rich Formation, showing fine-grained and coarse-grained alternating layers. (b) magnification of the red box in panel (a) showing the

characteristic siliciclastic coarse-grained laminae composed mainly of quartz grains alternating with a thinner fine-grained clay-rich layer represented by the red arrow. c-f, Siliciclastic iron-rich deposits showing various well-sorted rounded and sub-angular quartz grains floating in a black iron-rich matrix in the Fe-rich lithologies of the Wanimzi Formation. g-i, Examples of thin section photomicrographs for the siliciclastic carbonate-rich facies from the Taghdout Formation, characterized by ooids, quartz, carbonates and iron oxides. Ooid-peloid grainstone, the iron ooids (1) are made of microcrystalline calcitic laminae with radially arranged crystals (light rings) and iron enriched thinner laminae (dark). (2) peloids. (3) Oolites relicts showing the dissolution of the original structure and its replacement by drusy calcite crystals, indicating a neomorphism process (advanced diagenesis). (4) quartz. (5) calcite. The presence of intraclasts (red dashed line) indicate a shallow marine environment.

Fig. 6. Redox sensitive trace element, organic carbon ( $C_{org}$ ) and  $\delta^{13}C_{org}$  distribution up the studied stratigraphic section. (a-d), Trace element distribution for Zn, Cu, Mo, Co, As, V, U, Sb. e, Bulk iron enrichment averaging 22 wt.%, 0.73 wt.% and 1.1 wt.% in the Wanimzi Formation, the overlying siliciclastic stromatolitic succession and in the underlying siliciclastic carbonates from the Taghdout Formation, respectively. f, Zn/Co ratios. g, Mo/W ratio. h, Th/U ratio. i,  $C_{org}$  concentration. j, Carbon isotope distribution in  $C_{org}$ . Sil Car= Siliciclastic carbonates.

Fig. 7. PAAS-normalized REE+Y distribution across the succession. a, REE+Y patterns in the overlying Imi n'Tizi stromatolitic formation. b, REE+Y distribution in the siliciclastic iron-rich Wanimzi Formation. c, REE+Y distribution in the underlying Taghdout Formation carbonates.

Fig. 8. Relationship between hydrothermally enriched REES (Nd, La, Ga, Eu and Ce) and non-hydrothermally enriched REE (Pr), and Zr and Th typically enriched in siliciclastic deposits.



Fig. 9. (a) Eu anomalies calculated as  $(Eu/Eu^*)_{SN1} = Eu_{SN}/(0.67Sm_{SN} + 0.33Tb_{SN})$  and as  $(Eu/Eu^*)_{SN2} = 2 \times Eu_{SN}/(Sm_{SN} + Gd_{SN}) - (Eu/Eu^*)_{SN1}$  and  $(Eu/Eu^*)_{SN2}$  to correct for anomalously high Gd and Tb concentrations, respectively. (b) Light REE (LREE) to high REE (HREE) ratios. (c) Y/Ho ratios. (d),  $(La/Y)_{bSN}$  ratio. (e)  $(Tb/Yb)_{SN}$  ratio. (f)  $(Pr/Yb)_{SN}$  ratio. (g),  $(Sm/Yb)_{SN}$  ratio. (h)  $(Eu/Sm)_{SN}$  ratio. (i)  $(Gd/Gd^*)_{SN}$  ratio. SN=Shale normalized.

Fig. 10. Water column redox conditions determined by REE and Fe-based redox reconstruction. a, Cerium anomaly calculated as  $(Ce/Ce^*)_{SN} = Ce_{SN}/(0.5Pr_{SN} + 0.5La_{SN})$  and  $(Pr/Pr^*)_{SN} = Pr_{SN}/(0.5Ce_{SN} + 0.5Nd_{SN})$ . Black rings, blue diamonds and purple filled rings represent the Imi n'Tizi stromatolitic deposit, Wanimzi Formation and the Taghdout carbonates, respectively. With the exception (ironstone) of sample AG12 and CAB (Taghdout carbonate) all data points record true negative Ce Anomalies. b-c, Iron-based bottom water redox reconstruction. S1-S4= Imi n'Tizi stromatolitic deposit. AG01-AG17=Wanimzi Formation. CA1, CA2, CAB= Taghdout carbonates.

Fig. 11. Distribution of iron concentrations and isotopic distribution. a,  $\delta^{56}Fe$  and  $\delta^{57}Fe$  distribution in the iron-rich and siliciclastic stromatolitic rocks. b, Bulk iron dynamics showing that at less than 5 wt.% Fe concentration (vertical line),  $\delta^{56}Fe$  values are more positive and increasingly positive above this value. Above this line strong fractionation of iron produces more negative  $\delta^{56}Fe$  values. The asterisks depict two samples (AG08 and AG12) that deviate from the latter observations and are linked to the enrichment of LREE levels, as depicted by LREE/HREE ratios and  $(La/Yb)_{SN}$  (See Figure 9b and 9d). c,  $\delta^{56}Fe$  distribution in sedimentary marine iron formations deposited at key intervals across Earth history adapted from Planavsky et al. (2012) and Halverson et al. (2011) relative to the black-ringed values obtained in this study. SS=siliciclastic stromatolites.

Fig. 12. Relationship between iron and As (a), iron and V (b) and Mo and As (c) in the Wanimzi ironstones.

1693 Fig. 13. Conceptual model for the formation of the Wanimzi iron-rich shallow  
1694 marine ironstone deposit on the Tonian passive continental margin of the WAC.  
1695

Table 1. XRD mineralogical data (+=Detected; -=Not detected; ?=Uncertain)

	Lithology	Hematite	Magnetite	Goethite	Ankarite	Siderite	Albite	Kaolinite	Quartz	Chlorite	Dolomite	Calcite	Illite	K-feldspar
S1	Stromatolitic	+	-	-	?	-	+	+	+	-	?	+	+	+
S2	Stromatolitic	+	-	-	?	-	+	+	+	-	?	+	+	+
S3	Stromatolitic	+	-	-	-	-	+	-	+	-	-	-	+	+
S4	Stromatolitic	+	-	-	-	-	+	-	+	-	-	-	+	+
AG17	Iron-Quartz	+	-	-	-	-	+	-	+	-	-	-	+	+
AG16	Iron-Quartz	+	-	-	-	-	-	-	+	-	-	-	+	+
AG15	Iron-Quartz	+	-	-	-	-	-	-	+	-	-	-	+	+
AG14	Iron-Quartz	+	-	-	-	-	-	-	+	-	?	?	+	+
AG13	Iron-Quartz	+	-	-	-	-	-	-	+	-	-	?	+	+
AG12	Iron-Quartz	+	-	-	-	-	-	-	+	-	?	-	+	-
AG11	Iron-Quartz	+	-	-	-	-	-	-	+	-	-	-	-	+
AG10	Iron-Quartz	+	-	-	-	-	-	-	+	-	-	-	+	-
AG09	Iron-Quartz	+	-	-	-	-	-	-	+	-	-	-	-	-
AG08	Iron-Quartz	+	-	-	-	-	-	-	+	-	-	-	+	+
AG07	Iron-Quartz	+	-	-	?	-	-	-	+	-	?	?	+	+
AG06	Iron-Quartz	+	-	-	?	-	-	-	+	-	-	?	+	+
AG05	Iron-Quartz	+	-	-	-	-	-	-	+	-	-	-	?	-
AG04	Iron-Quartz	+	-	-	-	-	-	-	+	-	-	-	+	-
AG03	Iron-Quartz	+	-	-	-	-	-	-	+	+	?	-	-	-
AG02	Iron-Quartz	+	-	-	-	?	-	+	+	-	-	-	-	-
AG01	Iron-Quartz	+	-	-	-	-	-	-	+	-	-	-	-	-
AG0	Iron-Quartz	+	-	-	-	-	-	-	+	-	-	-	+	-
CA1	Carbonates	+	-	-	-	-	-	-	+	-	+	+	+	-
CA2	Carbonates	+	-	-	-	-	-	-	+	-	+	+	+	+
CAB	Carbonates	+	-	-	-	-	-	-	+	-	+	+	+	+

Table 2. Trace metal(loid) distribution. With the exception of Au measured in ppb concentrations are in ppm. Total Fe was measured by the ferrozine method (Stokey, 1970). Av. UCC (Average Upper Continental Crust concentrations (McLennan, 2001)). All UCC units are in ppm with the exception of Au, Bi, and Pd that are in ppb. AG/SS (Average concentration in iron-rich facies relative to average siliciclastic stromatolitic facies). AG/CAB (Average concentration in iron-rich facies relative to average siliciclastic carbonate lithologies). AG/UCC (Average iron-rich concentrations relative to average upper continental crust concentrations). SS/UCC (Average siliciclastic stromatolitic facies concentration relative to average upper continental crust). CAB/UCC (Average siliciclastic carbonate concentration relative to upper continental crust concentrations).

	As	Au	Ba	Co	Cu	Fe	Hf	Ga	Mo	Nb	Ni
Av. UCC	1.5	1.8	550	17	25	3500	5.8	17	1.5	12	44
S1	3.4	1.6	421	72.4	13.3	4741	13.6	7.7	0.2	6.8	1.6
S2	0.8	1.8	337	68.8	13.7	7298	17.3	8.6	0.2	7.9	2
S3	0.6	0.8	459	65.2	13.2	7292	7.4	11.3	0.2	8.2	2.1
S4	1.6	<0.5	568	39.7	12.1	7292	10.5	12.8	0.2	9.3	1.5
AG17	3.4	<0.5	362	80.2	59.4	34044	6.9	11.5	0.3	6.5	22.8
AG16	33.7	1.3	130	50.8	40.6	384333	5.3	2.6	1.5	2.4	10.1
AG15	6.9	<0.5	156	129.6	12.9	56597	4.6	2.8	0.6	2.8	3.7
AG14	1.9	0.7	319	194.1	13.9	13359	11.6	7.3	0.4	4.6	4.3
AG13	40.1	1	218	114	20.4	157849	8.4	9.3	2.6	5.2	17.2
AG12	4.1	<0.5	381	61.6	8.5	19857	5.6	10.2	1	7.5	3.9
AG11	86.9	1.6	37	29.7	2.8	520283	0.8	2.8	8.9	1.6	12.9
AG10	26.8	2.3	242	64.2	5.7	101151	4.9	6.6	2	5.4	5
AG09	111.3	3.4	57	9.9	4.2	583798	0.8	3.5	6.9	4	9.9
AG08	48.4	1.7	46	80.8	4.3	228895	0.9	5.2	4.8	2.9	6.7
AG07	66.1	0.9	350	86.6	2.4	24710	5.7	8.7	0.3	5.5	10.1
AG06	3.3	<0.5	289	148.7	35.7	18935	4.4	4.5	0.4	2.8	18.1
AG05	2.2	<0.5	539	64.5	7.2	60397	7.2	22.1	0.3	13.4	18.9

AG04	10.6	1.1	184	110.5	23.3	71295	4.7	6.1	1.1	3.2	28.6
AG03	10.6	1.1	336	43	23.3	617303	0.5	5.7	1.1	2.8	28.6
AG02	43.2	2.8	215	37.3	20.1	559723	1.2	3.8	3.4	2.1	31.1
AG01	22	2.6	423	39	120.7	535025	0.6	5.1	2.2	1.4	38.6
AG0	3.5	1.5	491	42.4	29.4	44948	8.2	17	0.3	10.3	12.5
CA1	3.4	9.9	1606	21.1	2.3	13348	1	1.6	0.1	1.4	1.5
CA2	0.1	1.2	383	22.3	10	6458	2.5	2.9	2.2	1.5	3.3
CAB	6.4	1.4	215	38.9	4.6	11872	2.9	2.3	0.1	1.8	2.2
AG/SS	18.2	1.2	0.6	1.3	1.8	33.7	0.4	0.7	10.6	0.6	8.7
AG/CAB	8.8	0.4	0.4	2.8	4.3	21.2	2.1	3.3	2.6	3	6.7
AG/UCC	19.4	0.9	0.5	4.5	1	64	0.8	0.4	1.4	0.4	0.4
SS/UCC	1.1	0.8	0.8	3.6	0.5	1.9	2.1	0.6	0.1	0.7	0.04
CAB/UCC	2.2	2.3	1.3	1.6	0.2	3	0.4	0.1	0.5	0.1	0.05
	Pb	Rb	Sb	Sr	Ta	Th	U	V	W	Zn	Zr
UCC	0.5	112	0.2	350	1	10.7	2.8	107	2	71	190
S1	0.9	94.8	0	17.6	1.4	8.2	1.7	28	448.1	1	18.6
S2	1	95.5	0	16.9	1.3	9.5	0.9	34	491.1	0	21.6
S3	1.2	126.6	0	29.7	1.1	9.1	0.5	41	44.8	2	14.9
S4	1.2	151.1	0.2	21.9	1.1	10.6	1	42	242.6	1	20.3
AG17	1	104.7	0.1	13.3	1.2	9	1.8	56	517.7	8	23.4
AG16	2	22.3	0.9	12.1	0.7	3.7	1.1	17	332.8	10	31.7
AG15	1.8	29.6	0.2	11.3	1.8	3.5	1.3	11	936.5	3	8.9
AG14	0.8	71.4	0.1	17	2.7	6.7	0.9	30	1332.5	1	13.2
AG13	4.9	87.9	2.4	13.1	1.6	6.6	2.1	37	749.9	4	14.2
AG12	0.7	117.4	0.3	16	1.3	8.4	2.2	54	461.3	1	15
AG11	3.4	15.8	5.3	5	0.4	2.8	1.2	74	172.9	2	7.5
AG10	2.9	69.8	2	13	1.2	5.8	0.4	31	486.2	2	12.7

AG09	11.3	25.3	7.8	6.8	0.2	2.2	2.3	81	36.3	2	13.9
AG08	4.3	37.3	3.6	4.5	1	4.5	1	74	580.5	1	21.1
AG07	1.2	84.8	0.1	13.6	1.6	6.4	2.2	44	663.9	4	13.4
AG06	0.8	47.4	0	14.1	2.2	3	1.9	24	1250.8	7	7.2
AG05	1.5	186.7	0.3	20.8	1.8	16	2.3	110	484.3	7	17.2
AG04	1.7	36.6	0.3	8.6	1.9	4.3	1	47	941.9	10	12.9
AG03	1.7	5.5	2.5	9.8	0.2	2	2.2	178	75.2	10	14.4
AG02	5.1	3	2.8	8.8	0.3	2.5	1.9	172	180.8	11	27.6
AG01	3.3	3.5	1.4	11	0.2	1.6	1	139	135.1	15	15.4
AG0	1.6	143.3	0.3	20.8	1.7	12.5	2.5	95	516.2	4	30.9
CA1	14.6	21.5	0.1	1074.4	0.3	10.7	0.4	8	128.3	8	25
CA2	10	44	0	790.8	0.3	7.7	0.4	9	111.9	3.3	18.4
CAB	11	29.1	0	1033.9	0.4	11.7	0.4	<8	227.8	9	20.8
AG/SS	2.6	0.5	33.8	0.6	1	0.6	1.6	2	1.8	5.7	0.9
AG/CAB	0.2	1.9	50.7	0.01	3.7	0.6	4.1	8.3	3.5	0.8	0.8
AG/UCC	5.6	0.5	8.4	0.03	1.2	0.5	0.6	41.6	273.7	0.1	0.1
SS/UCC	2.2	1	0.3	0.1	1.2	0.9	0.4	21.3	153.3	0.01	0.1
CAB/UCC	23.7	0.3	0.2	2.8	0.3	0.9	0.1	5	78	0.1	0.1

---

Table 3. Carbon, iron, and oxygen isotopic data

	Lithology	$\delta^{13}\text{C}_{\text{carbonate}}$ (‰ VPDB)	1sd	$\delta^{18}\text{O}_{\text{carbonate}}$ (‰ VPDB)	1sd	Carbonate (%wt)	$\delta^{13}\text{C}_{\text{org}}$ (‰ VPDB)	1sd	C <sub>org</sub> (wt%)	$\delta^{56}\text{Fe}$ (‰ IRMM)	2sd	$\delta^{57}\text{Fe}$ (‰ IRMM)	2sd
S1	Stromatolitic	-1.84	0.10	-13.13		0.02	-31.80	0.49	0.01	0.61	0.05	0.86	0.14
S2	Stromatolitic	ND*	-	ND*	-	0.01	-30.16	0.49	0.01	0.45	0.05	0.70	0.15
S3	Stromatolitic	-0.33	0.22	-4.00	0.17	0.02	-28.13	0.49	0.02	0.57	0.05	0.88	0.15
S4	Stromatolitic	-4.50	0.18	-9.29	0.16	0.01	-27.87	0.49	0.01	0.45	0.05	0.66	0.14
AG17	Iron-Quartz	ND*	-	ND*	-	ND*	-29.97	0.49	0.03	-0.14	0.05	-0.21	0.14
AG16	Iron-Quartz	ND*	-	ND*	-	ND*	-27.44	0.49	0.01	-0.04	0.05	-0.09	0.14
AG15	Iron-Quartz	ND*	-	ND*	-	ND*	-31.53	0.49	0.03	-0.07	0.05	-0.15	0.14
AG14	Iron-Quartz	-8.72	-	-12.788	-	0.02	-29.82	0.49	0.04	0.03	0.05	0.02	0.14
AG13	Iron-Quartz	ND*	-	ND*	-	ND*	-27.81	0.49	0.03	-0.41	0.05	-0.65	0.14
AG12	Iron-Quartz	ND*	-	ND*	-	ND*	-30.64	0.49	0.02	0.26	0.05	0.52	0.14
AG11	Iron-Quartz	ND*	-	ND*	-	ND*	-28.38	0.49	0.01	-0.19	0.05	-0.31	0.14
AG10	Iron-Quartz	ND*	-	ND*	-	ND*	-29.15	0.49	0.02	0.03	0.05	0.08	0.14
AG09	Iron-Quartz	ND*	-	ND*	-	ND*	-26.12	0.49	0.02	0.06	0.05	0.03	0.14
AG08	Iron-Quartz	ND*	-	ND*	-	ND*	-30.27	0.49	0.02	0.35	0.05	0.54	0.14
AG07	Iron-Quartz	ND*	-	ND*	-	ND*	-30.74	0.49	0.02	0.06	0.05	0.14	0.14
AG06	Iron-Quartz	ND*	-	ND*	-	ND*	-33.03	0.49	0.02	-0.37	0.05	-0.46	0.14
AG05	Iron-Quartz	ND*	-	ND*	-	ND*	-29.33	0.49	0.03	0.11	0.05	0.27	0.14

AG04	Iron-Quartz	-8.72	0.21	-12.788	0.21	ND*	-28.56	0.49	0.02	-0.15	0.05	-0.31	0.14
AG03	Iron-Quartz	ND*	-	ND*	-	ND*	-28.82	0.49	0.02	0.07	0.05	0.30	0.14
AG02	Iron-Quartz	ND*	-	ND*	-	ND*	-27.50	0.49	0.01	-0.22	0.05	-0.28	0.14
AG01	Iron-Quartz	ND*	-	ND*	-	ND*	-22.93	0.49	0.01	-0.09	0.05	-0.08	0.14
AG0	Iron-Quartz	ND*	-	ND*	-	ND*	-29.62	0.49	0.04	0.15	0.05	0.21	0.14
CA1	Carbonates	-0.77	0.13	-14.50	0.10	75	-26.44	0.49	0.04	ND	0.05	ND	0.14
CA2	Carbonates	0.11	0.07	-13.28	0.06	50	-27.41	0.49	0.04	ND	0.05	ND	0.14
CAB	Carbonates	-0.18	0.05	-14.30	0.05	75	-28.41	0.49	0.06	ND	0.05	ND	0.14

---

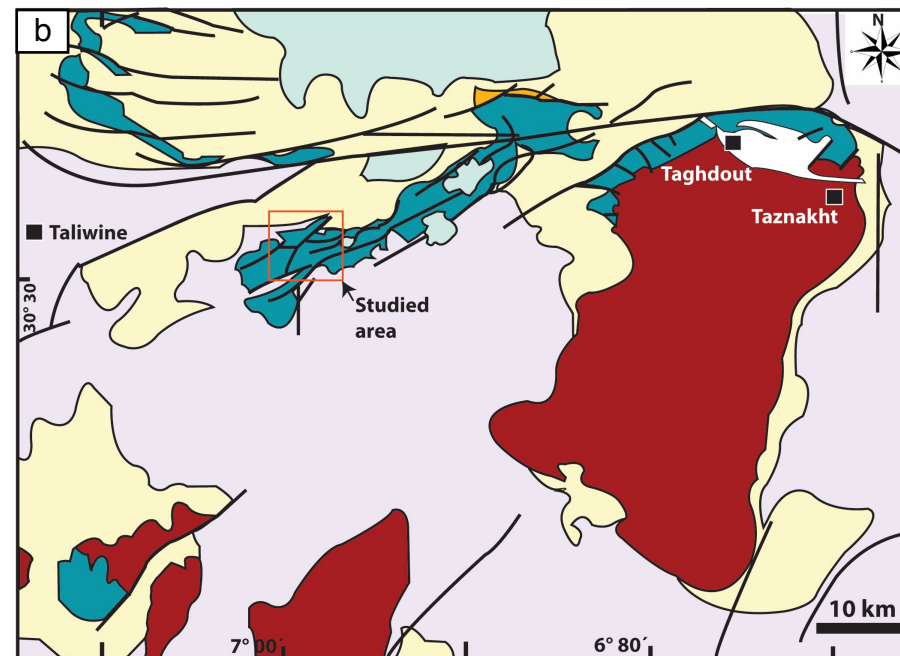
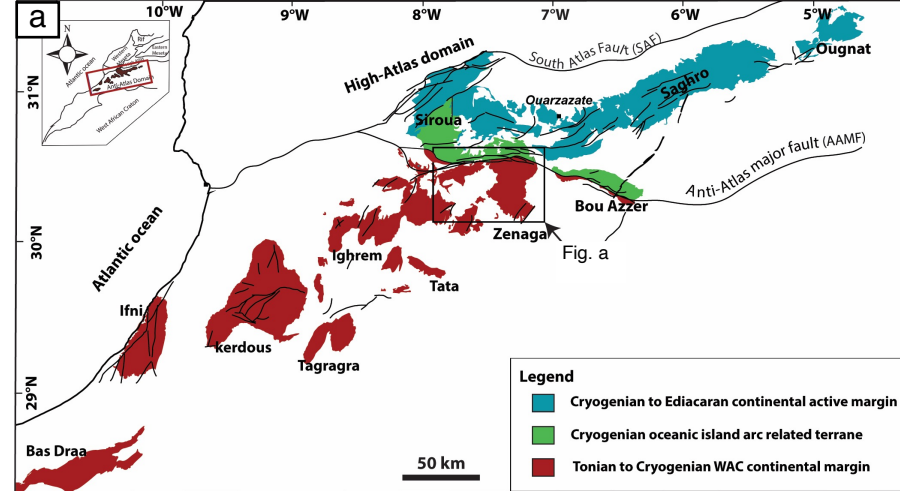
ND=Not determined

ND\*=Not determined because of extremely low carbonate content



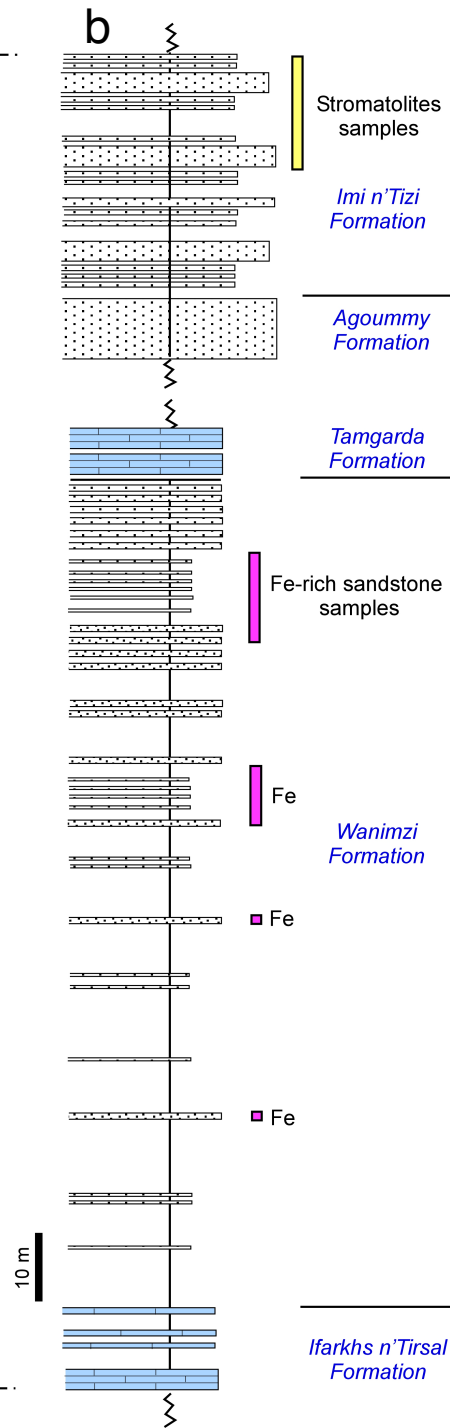
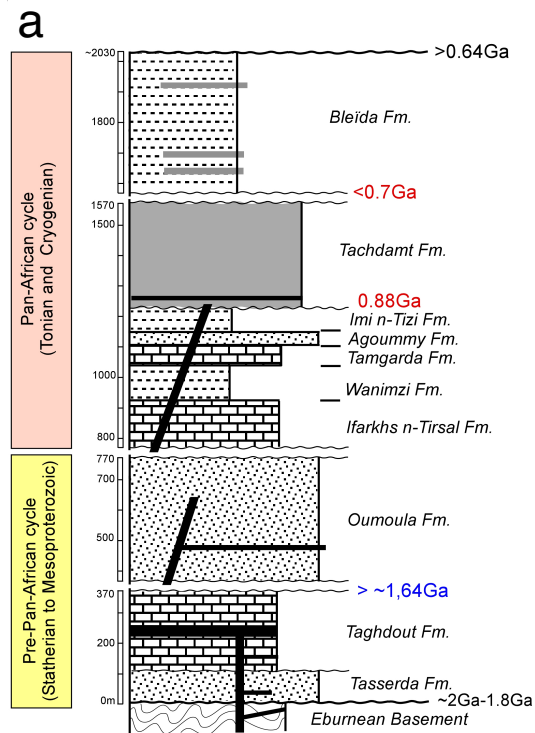
Table 4. Rare Earth Element +Yttrium. S1-S2=Siliciclastic stromatolitic mats. AG17-AG0=Wanimzi Formation. CA1,2,B=Taghdout carbonates.

	Lithology	La	Ce	Pr	Nd	Sm	Eu	Gd	Tb	Dy	Y	Ho	Er	Tm	Yb	Lu	ΣREE+Y	ΣREE
S1	Stromatolite	26.6	52.2	5.46	19.8	3.15	0.59	2.57	0.47	3.1	18.6	0.68	2.1	0.31	2.11	0.35	138.1	119.5
S2	Stromatolite	26.5	56.9	6.11	22.8	3.76	0.75	3.24	0.55	3.49	21.6	0.73	2.53	0.37	2.56	0.42	152.3	130.7
S3	Stromatolite	35.4	67.1	7.12	25.2	3.73	0.65	2.77	0.42	2.71	14.9	0.59	1.8	0.27	1.84	0.31	164.8	149.9
S4	Stromatolite	32.6	66.6	7.46	28.5	4.71	0.88	4.16	0.63	3.63	20.3	0.73	2.39	0.36	2.29	0.37	175.6	155.3
AG17	Iron-Quartz	17.6	35.9	4.45	19.3	6.2	1.46	8.38	1	4.51	23.4	0.79	2.09	0.29	1.84	0.27	127.5	104.1
AG16	Iron-Quartz	12.8	27.6	3.1	12.8	3.84	1.22	8.93	1.26	5.81	31.7	0.94	2.36	0.25	1.64	0.23	114.5	82.8
AG15	Iron-Quartz	10.7	23.7	2.75	10.8	2.56	0.57	2.53	0.32	1.67	8.9	0.29	0.84	0.12	0.84	11	77.6	68.7
AG14	Iron-Quartz	13.5	28	2.79	10	1.72	0.4	1.89	0.35	2.24	13.2	0.47	1.59	0.24	1.58	0.24	78.2	65.0
AG13	Iron-Quartz	23.2	54.4	5.3	19.3	3.28	0.8	3.11	0.48	2.87	14.2	0.52	1.58	0.23	1.56	0.25	131.1	116.9
AG12	Iron-Quartz	41.6	79.7	7.42	26.1	4.08	0.78	3.14	0.43	2.65	15	0.54	1.64	0.24	1.54	0.25	185.1	170.1
AG11	Iron-Quartz	3.8	10.5	1.15	5.3	2.15	0.58	2.54	0.38	1.81	7.5	0.31	0.76	0.11	0.68	0.1	37.7	30.2
AG10	Iron-Quartz	14.7	35.7	3.64	14.7	3.27	0.75	3.05	0.46	2.56	12.7	0.48	1.47	0.19	1.31	0.2	95.2	82.5
AG09	Iron-Quartz	15.3	39.6	4.05	17.6	4.78	1.09	4.67	0.68	3.34	13.9	0.55	1.32	0.16	1.11	0.14	108.3	94.4
AG08	Iron-Quartz	55.6	237.8	28.51	157.2	57.78	9.09	35.91	2.45	6.97	21.1	0.6	1.22	0.19	1.32	0.16	615.9	594.8
AG07	Iron-Quartz	18.7	36.4	4.2	15.9	2.98	0.59	2.52	0.38	2.22	13.4	0.44	1.36	0.21	1.31	0.22	100.83	87.4
AG06	Iron-Quartz	9.3	18.1	5.8	8	1.76	0.4	1.79	0.25	1.4	7.2	0.26	0.79	0.11	0.7	0.12	55.6	48.8
AG05	Iron-Quartz	25.1	51.4	5.8	22.2	4.79	0.93	3.79	0.54	3.12	17.2	0.64	1.94	0.29	1.97	0.28	140	122.8
AG04	Iron-Quartz	6.9	13.2	1.62	7.2	2.61	0.72	4	0.56	2.73	12.9	0.48	1.28	0.17	1.05	0.15	55.6	42.7
AG03	Iron-Quartz	5.5	12	1.42	6.1	2.54	0.81	4.39	0.66	3.08	14.4	0.55	1.26	0.15	0.87	0.12	53.9	39.5
AG02	Iron-Quartz	5.2	10.6	1.4	6.7	2.99	1.04	6.39	1.04	5.28	27.6	0.93	2.28	0.24	1.43	0.19	73.3	45.7
AG01	Iron-Quartz	3.1	6.2	0.91	4.6	2.42	0.84	5.43	0.78	3.38	15.4	0.58	1.33	0.14	0.89	0.11	46.1	30.7
AG0	Iron-Quartz	30.9	61.8	7.18	30	9.15	2.25	12.32	1.46	6.18	30.9	1.11	2.73	0.37	2.41	0.36	199.1	168.2
CA1	Carbonate	35.1	71.1	6.55	24.6	4.82	1.11	4.82	0.77	4.78	25	0.94	2.93	0.41	2.93	0.4	186.3	161.2
CA2	Carbonate	28.1	61.6	5.77	21.3	4.03	0.81	3.45	0.52	3.25	18.4	0.64	1.94	0.26	1.83	0.28	152.2	133.8
CAB	Carbonate	42.7	86	8.14	30.2	5.29	0.96	4.42	0.68	3.95	20.8	0.77	2.21	0.33	2.13	0.33	208.9	188.1

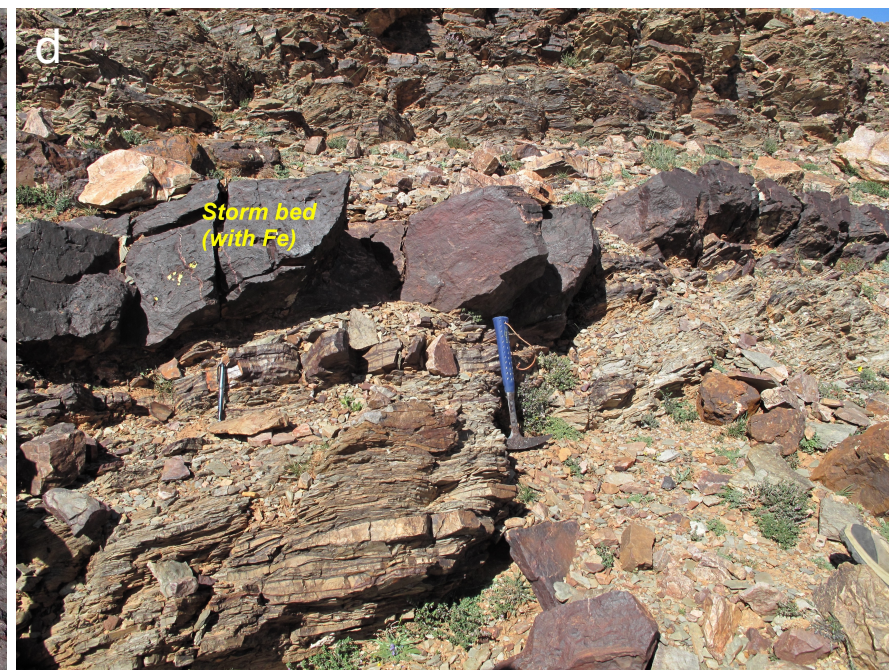
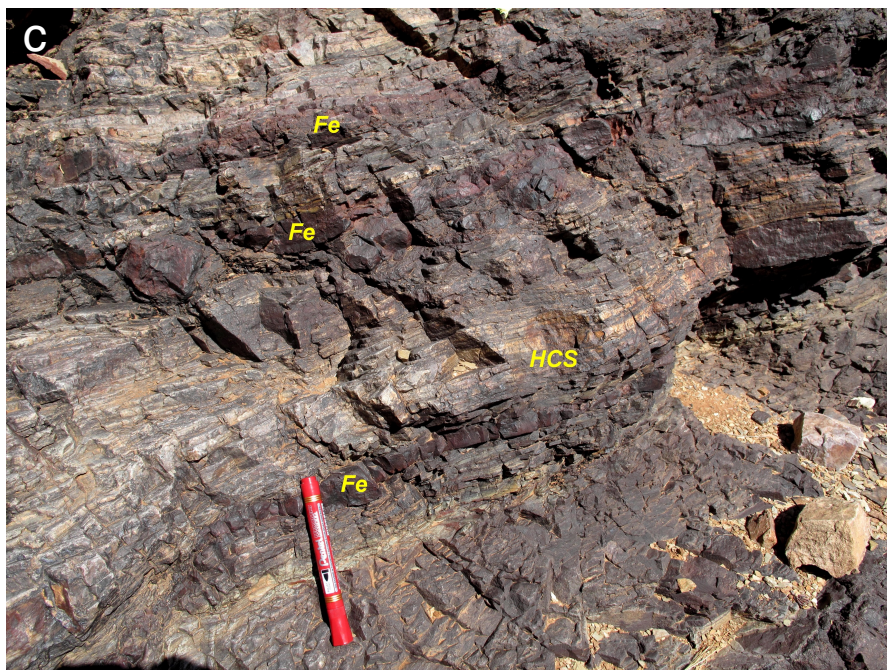
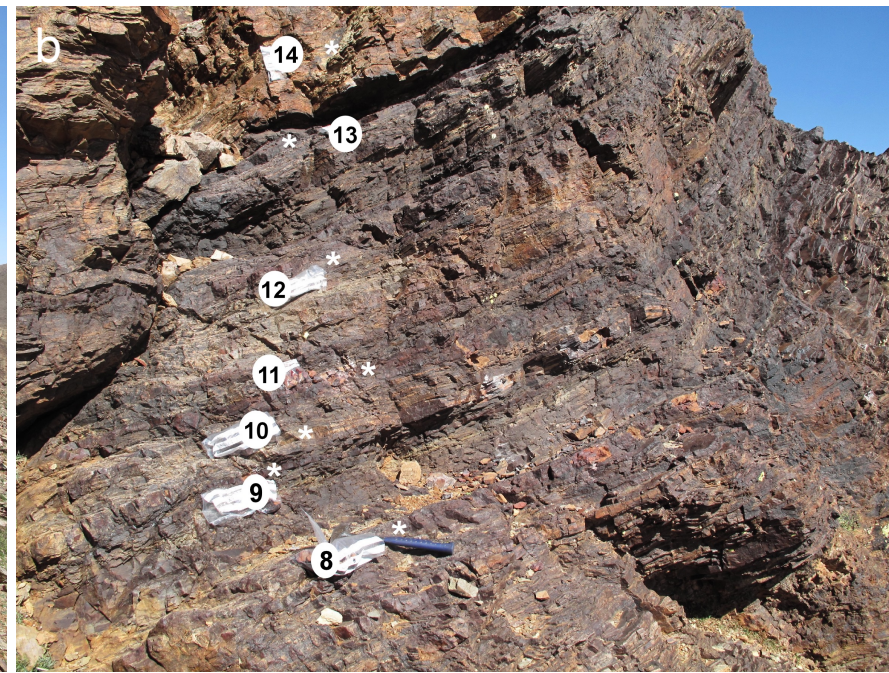
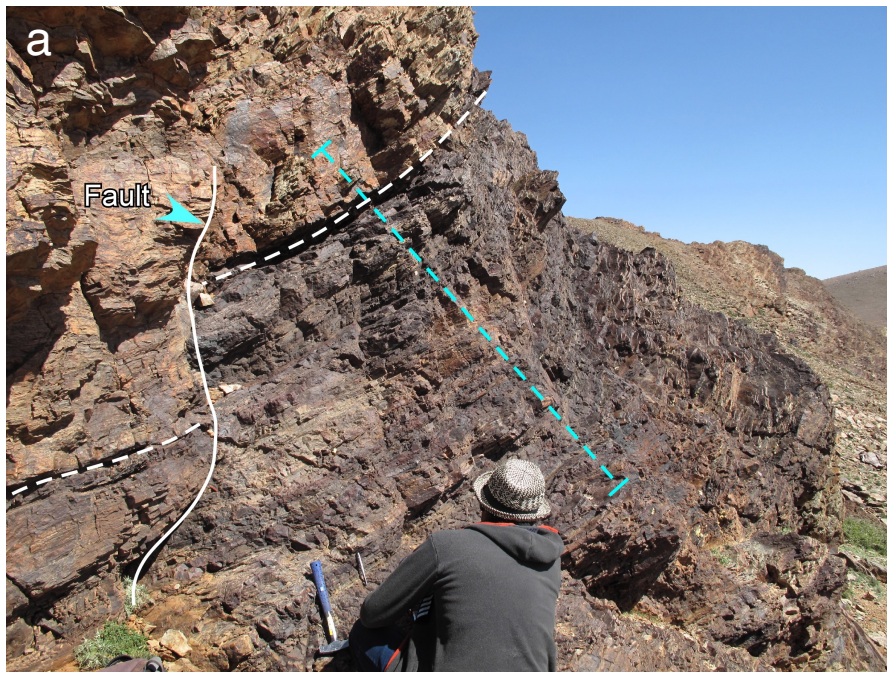


**Legend**

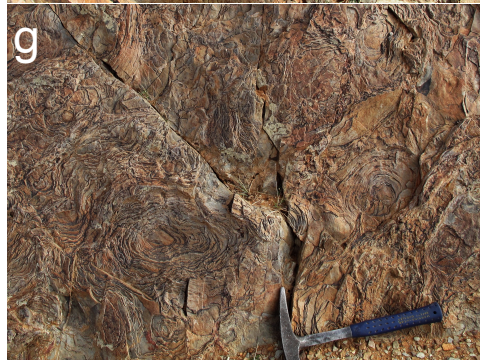
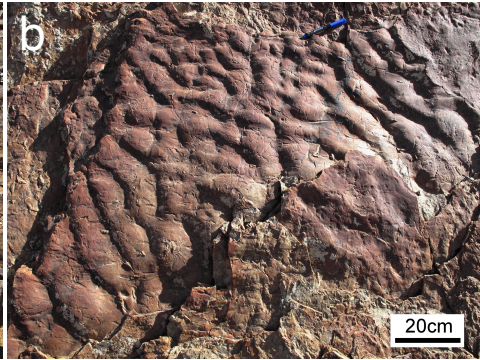
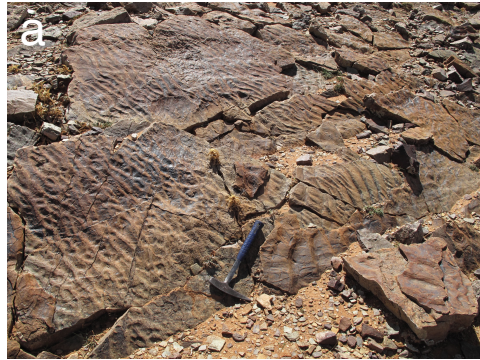
- |  |   |
|--|---|
| Tonian /Cryogenian arc terrane (ca. 770 to 640 Ma)             | Neogene volcano   |
| Upper Paleoproterozoic to Cryogenian continental margin strata | Late Ediacaran to Paleozoic units                       |
| Paleoproterozoic Eburnean basement (WAC)                       | Ediacaran Saghro and Ouarzazate Groups (ca. 625-550 Ma) |



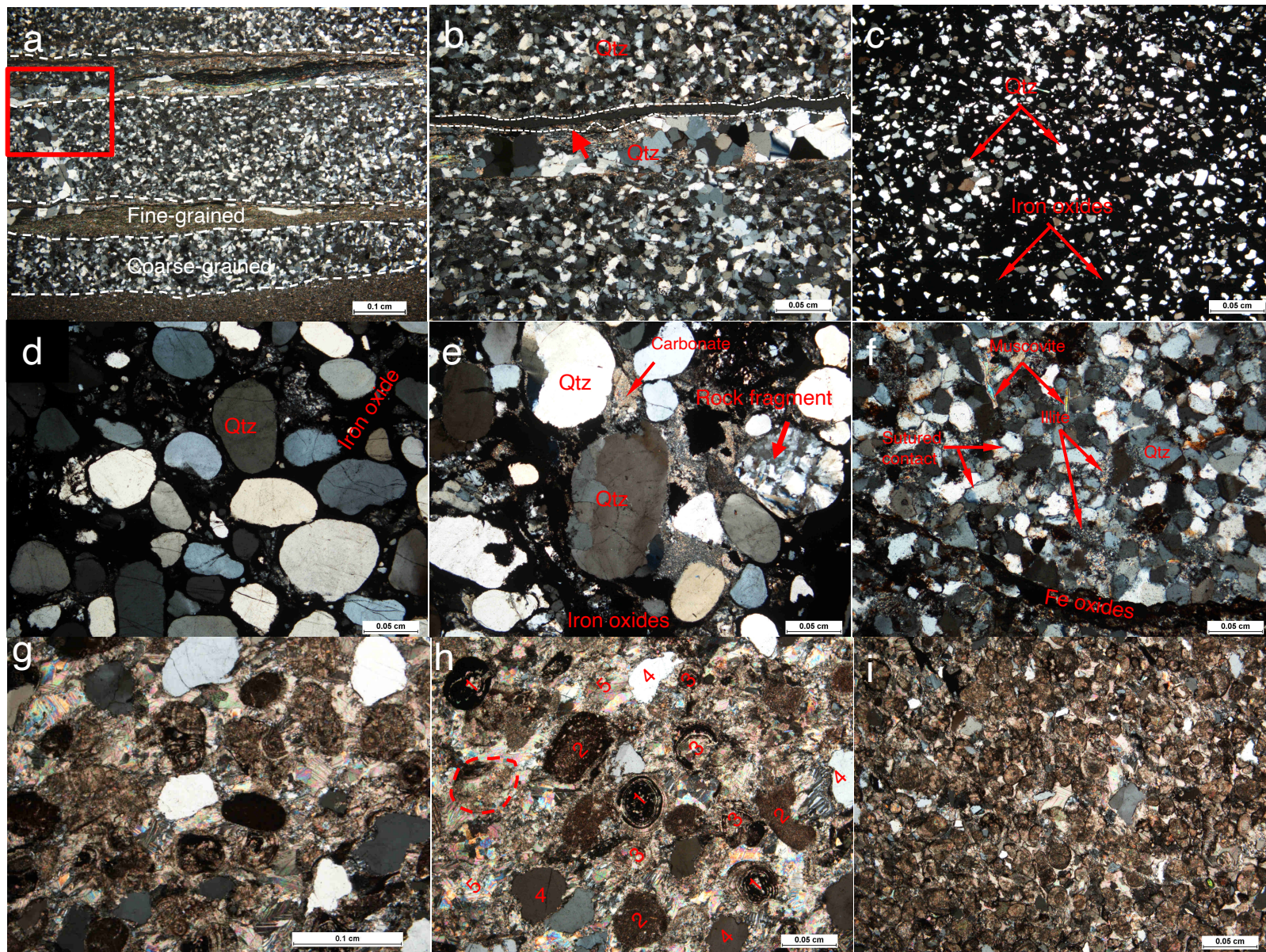




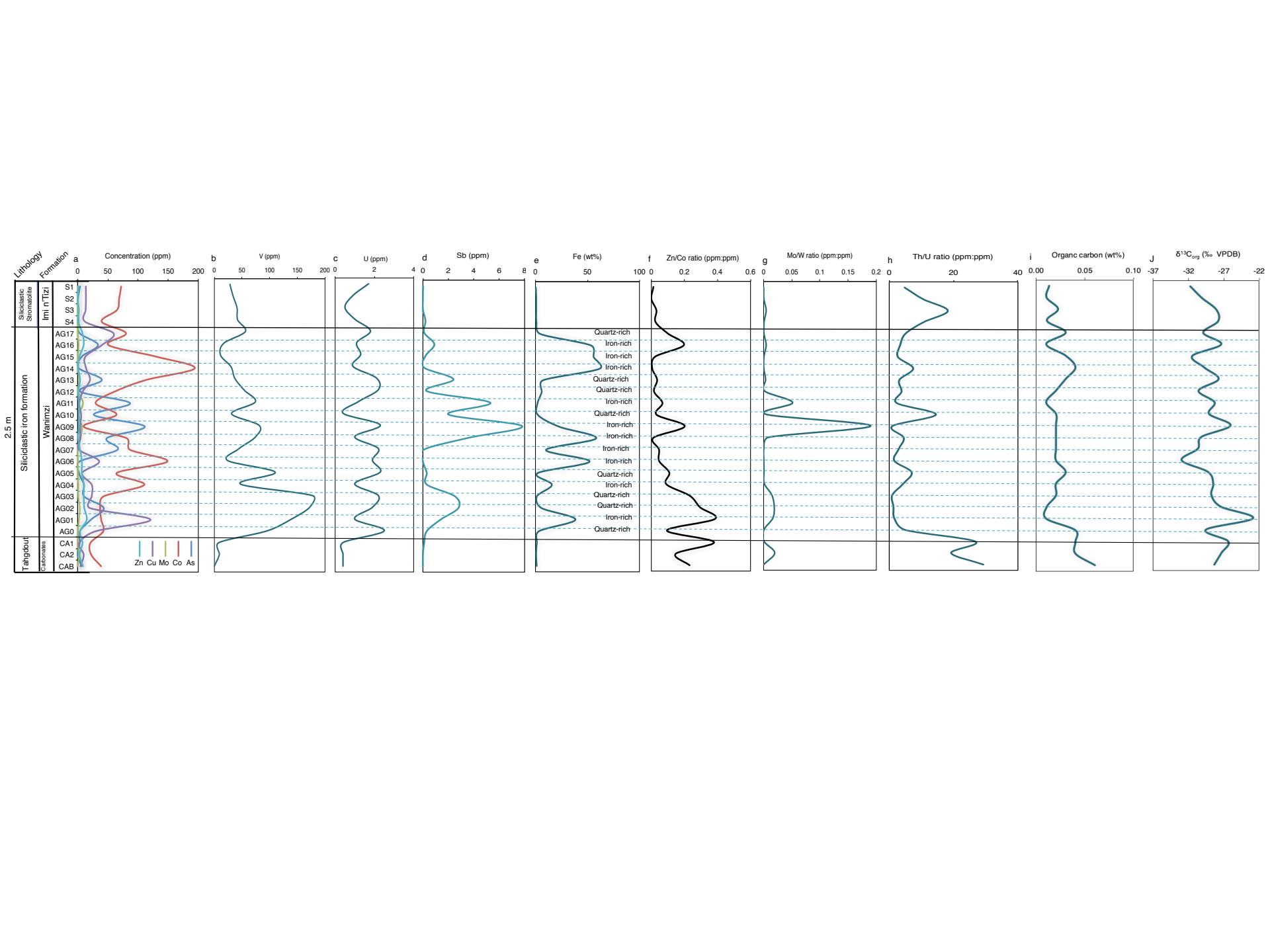


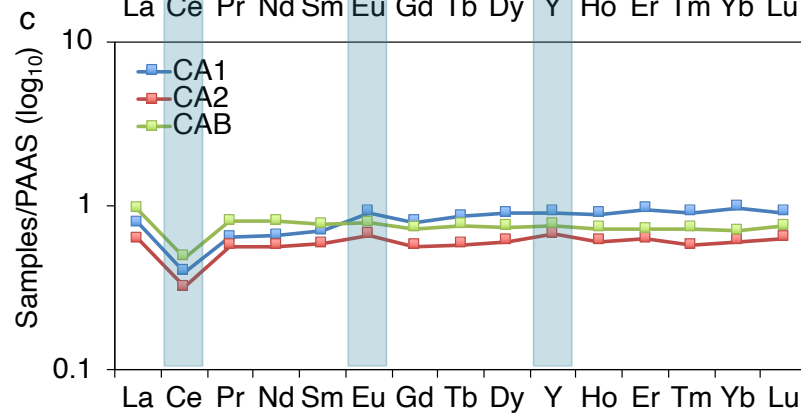
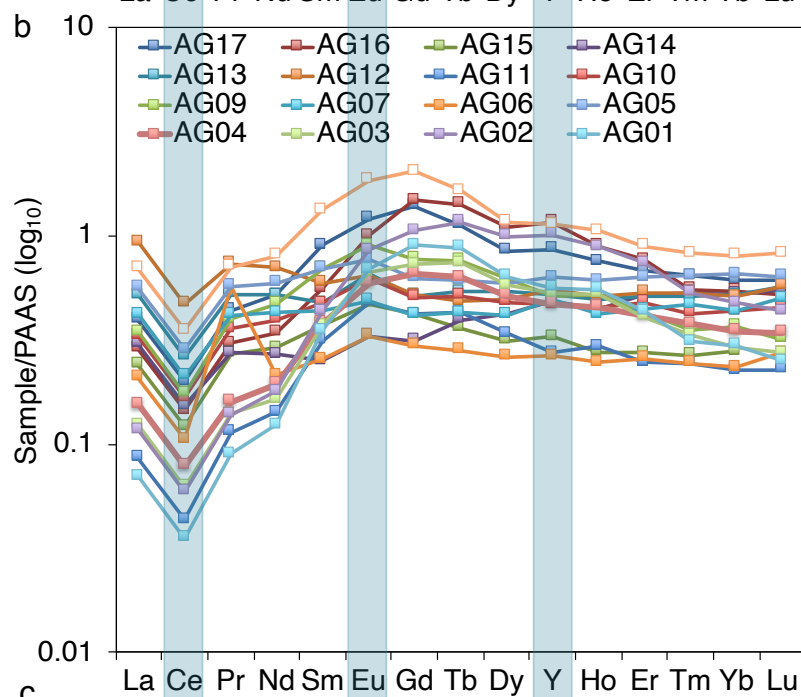
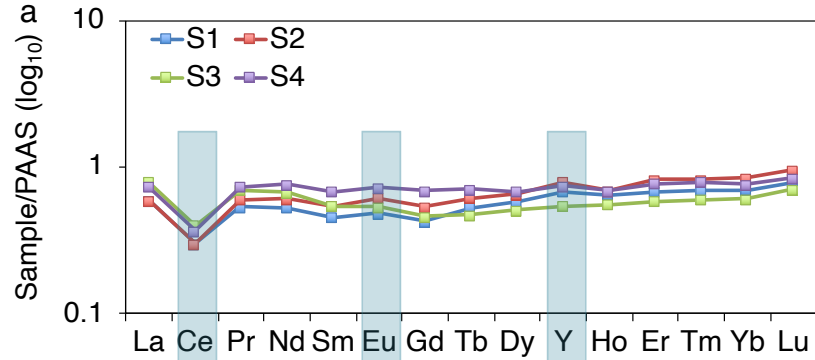




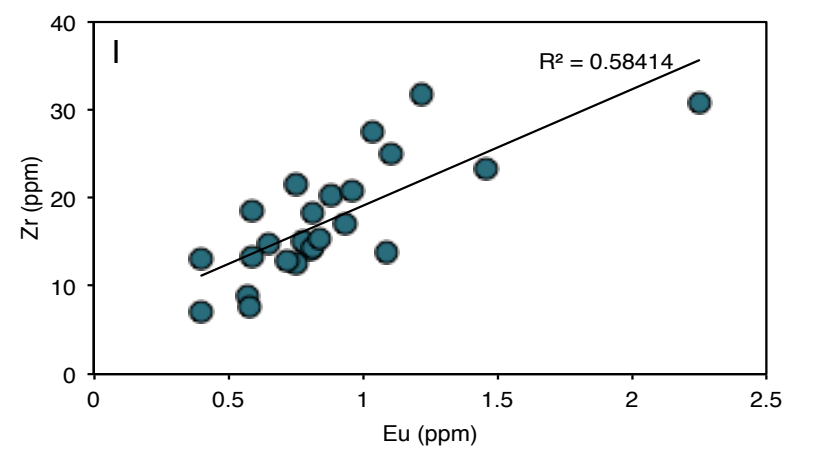
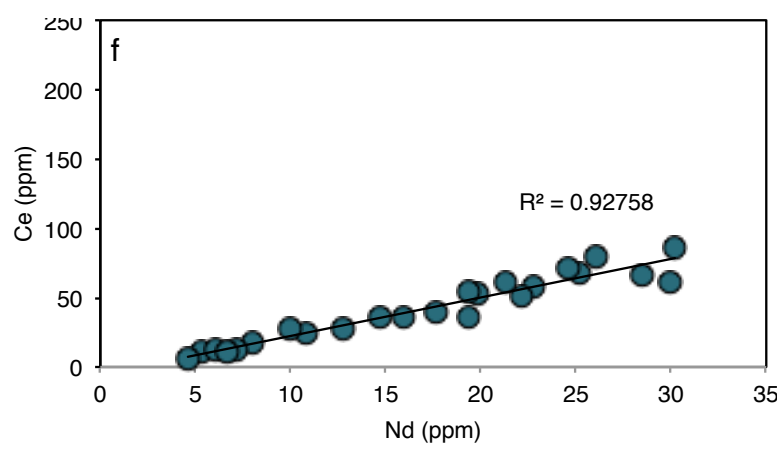
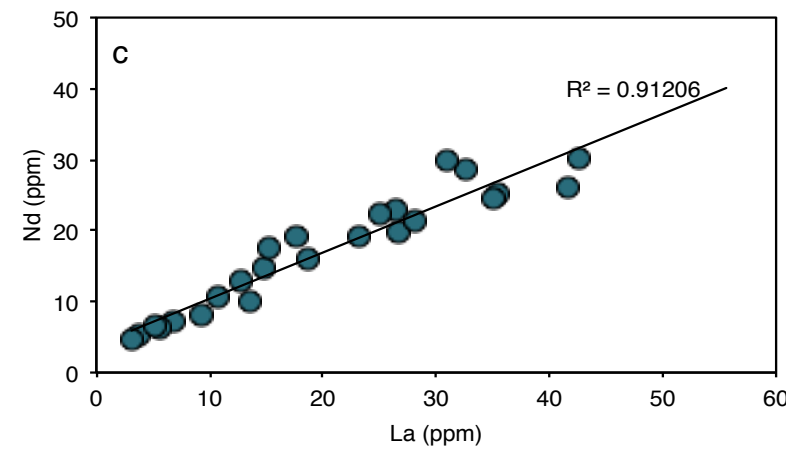
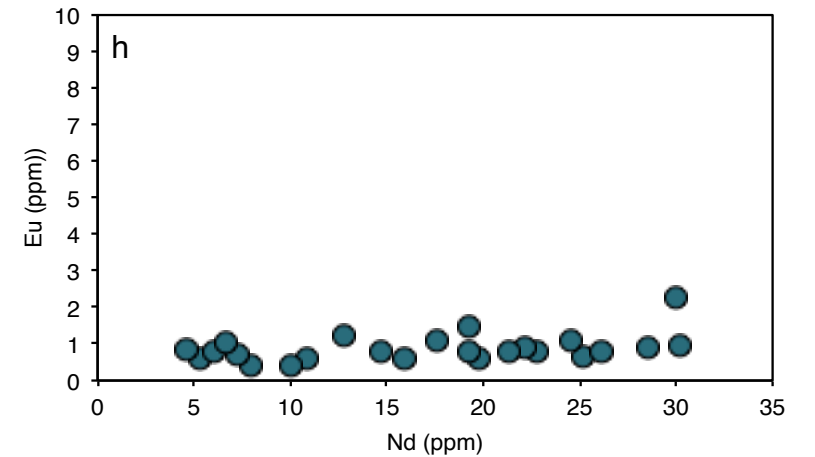
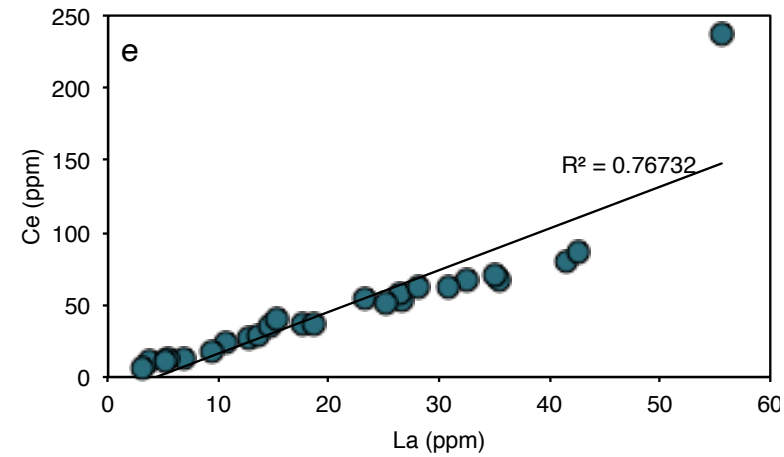
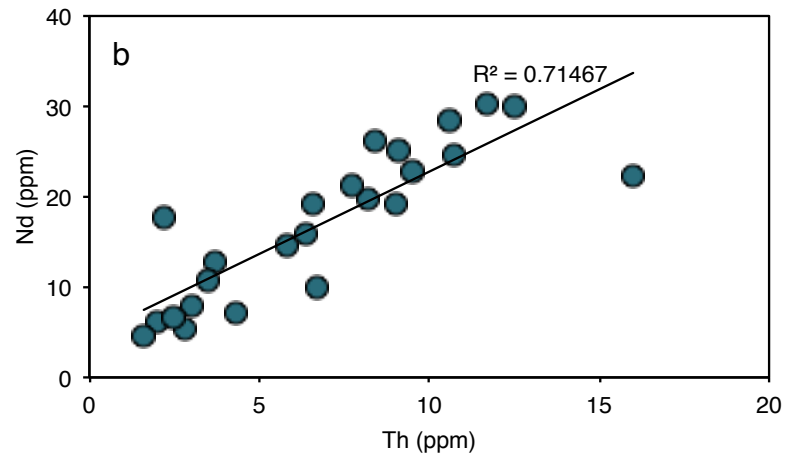
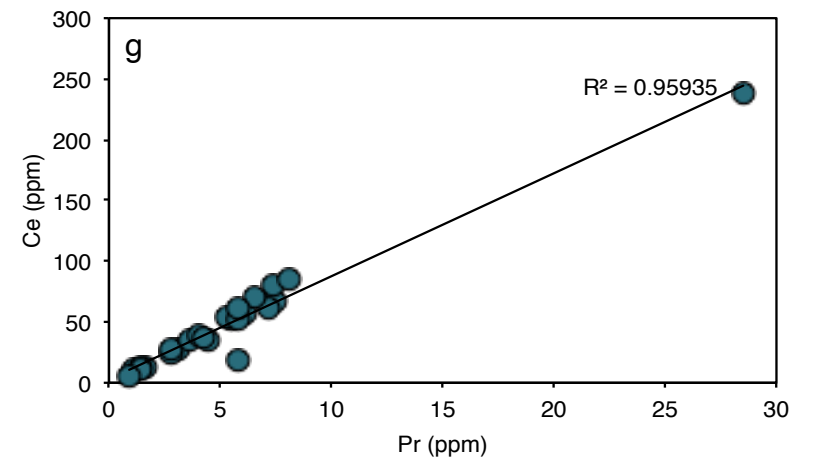
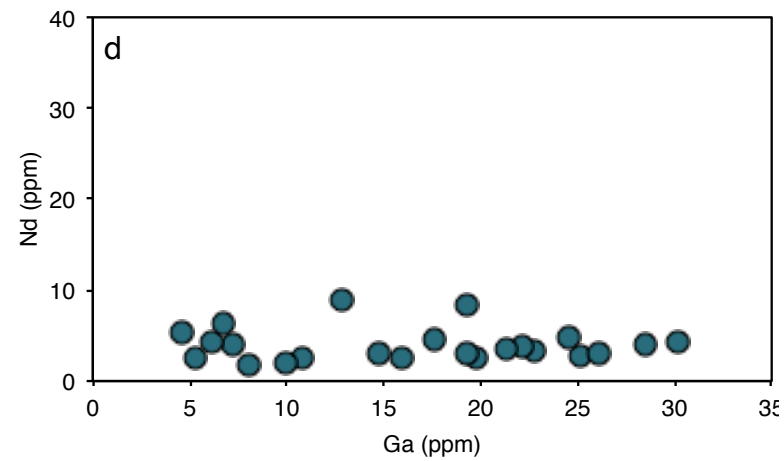
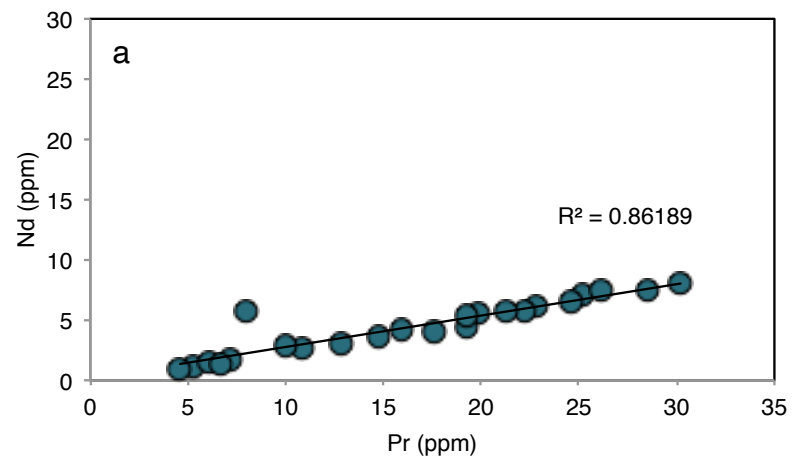


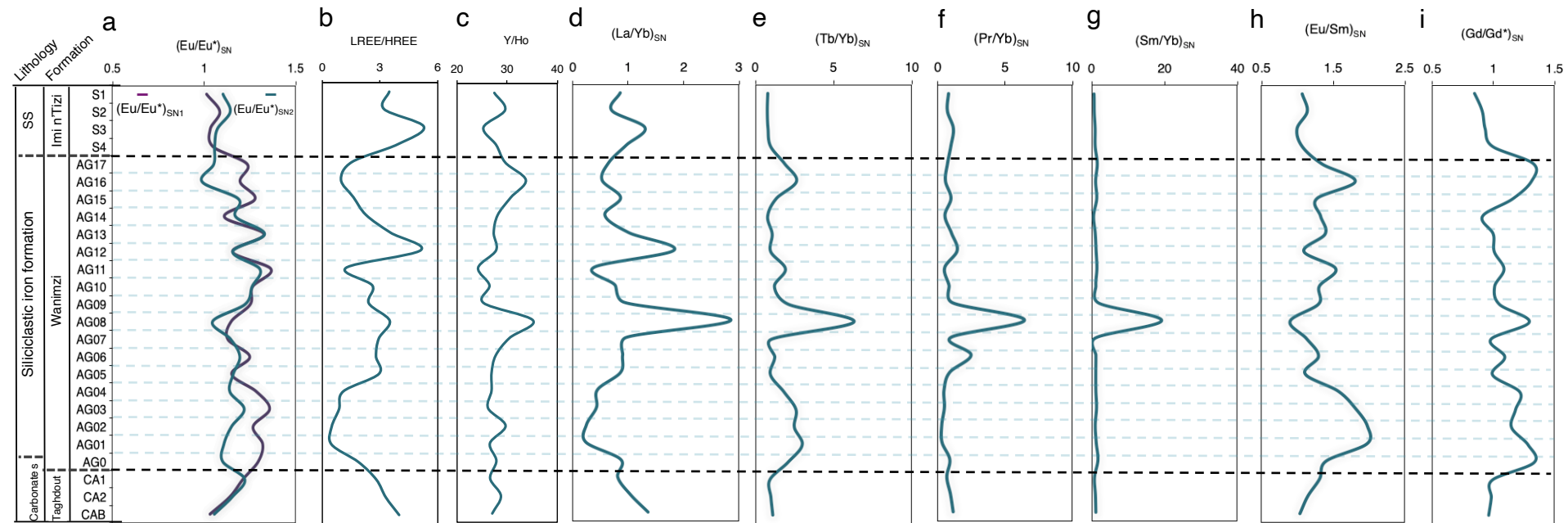


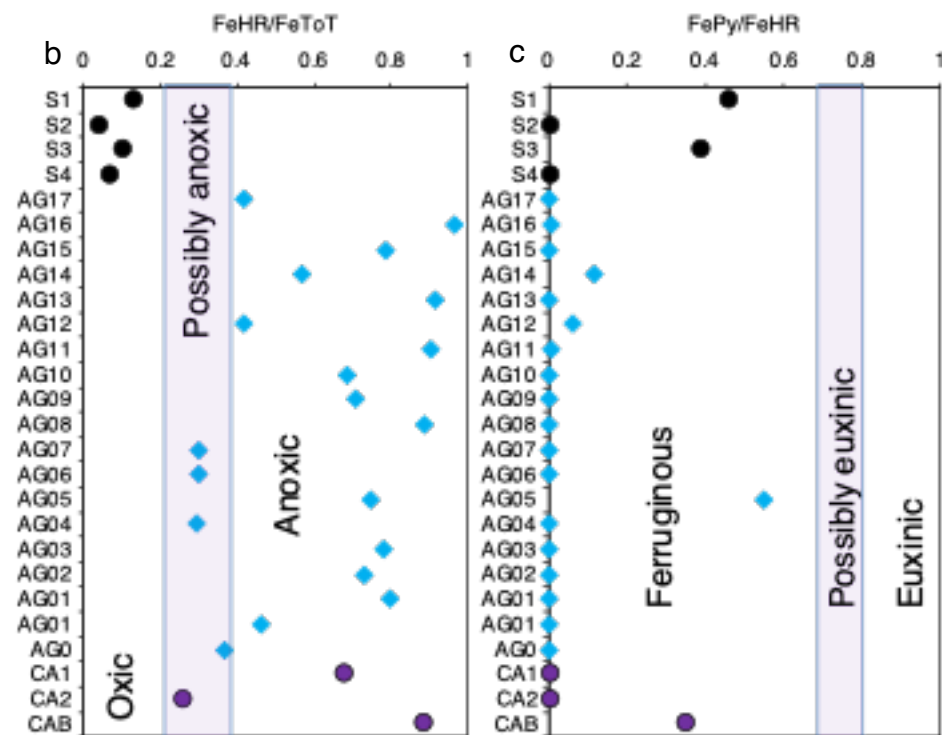
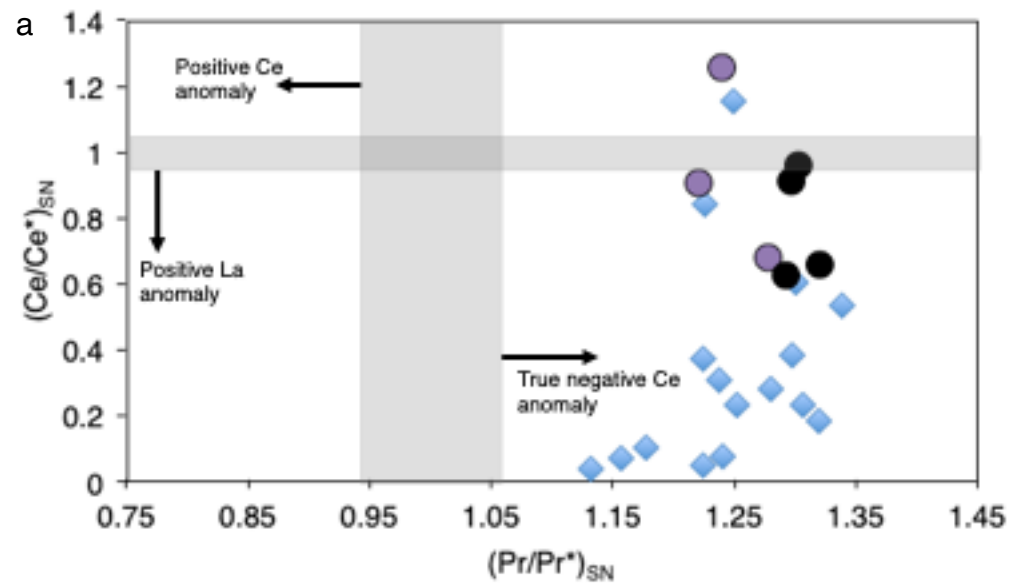


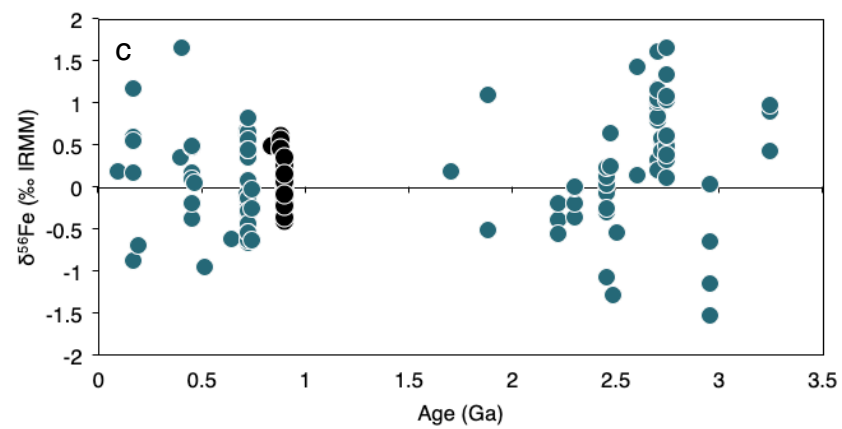
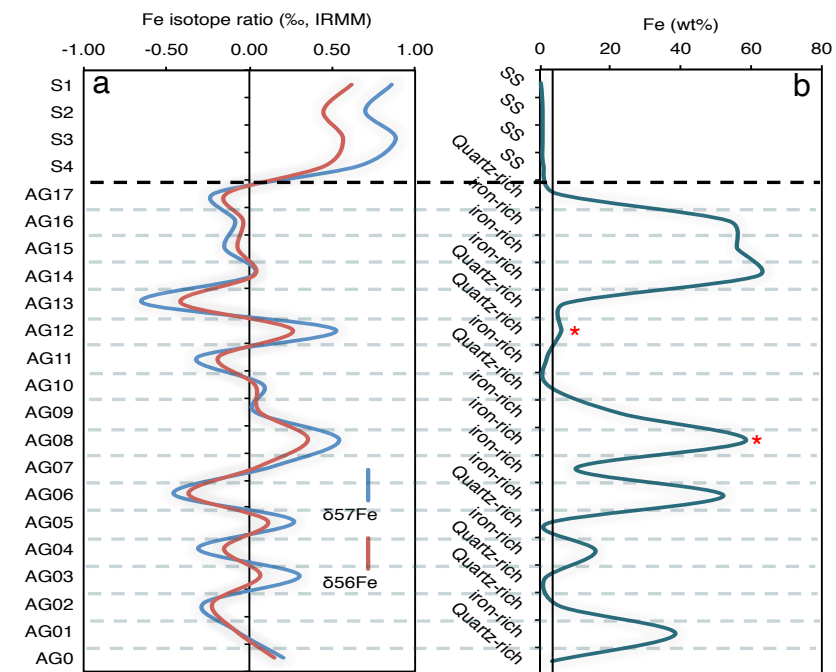


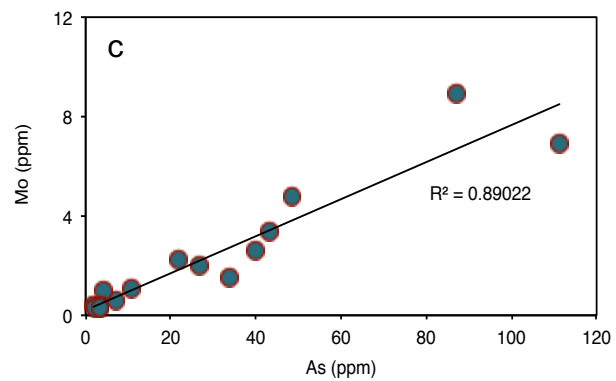
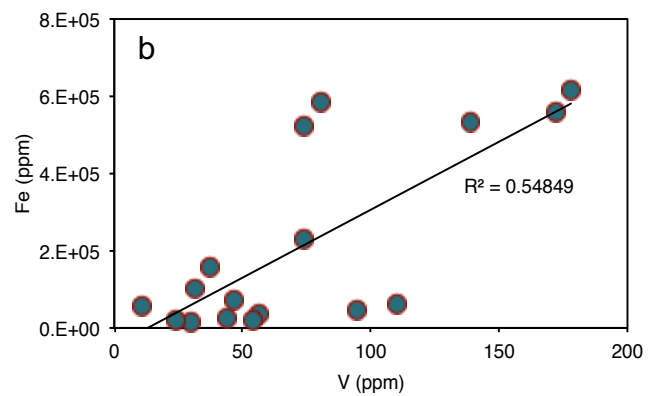
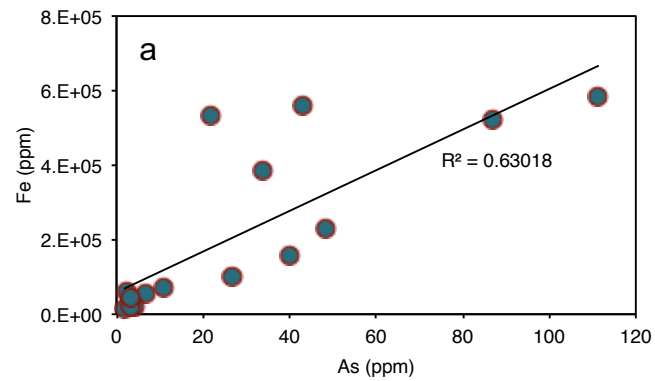


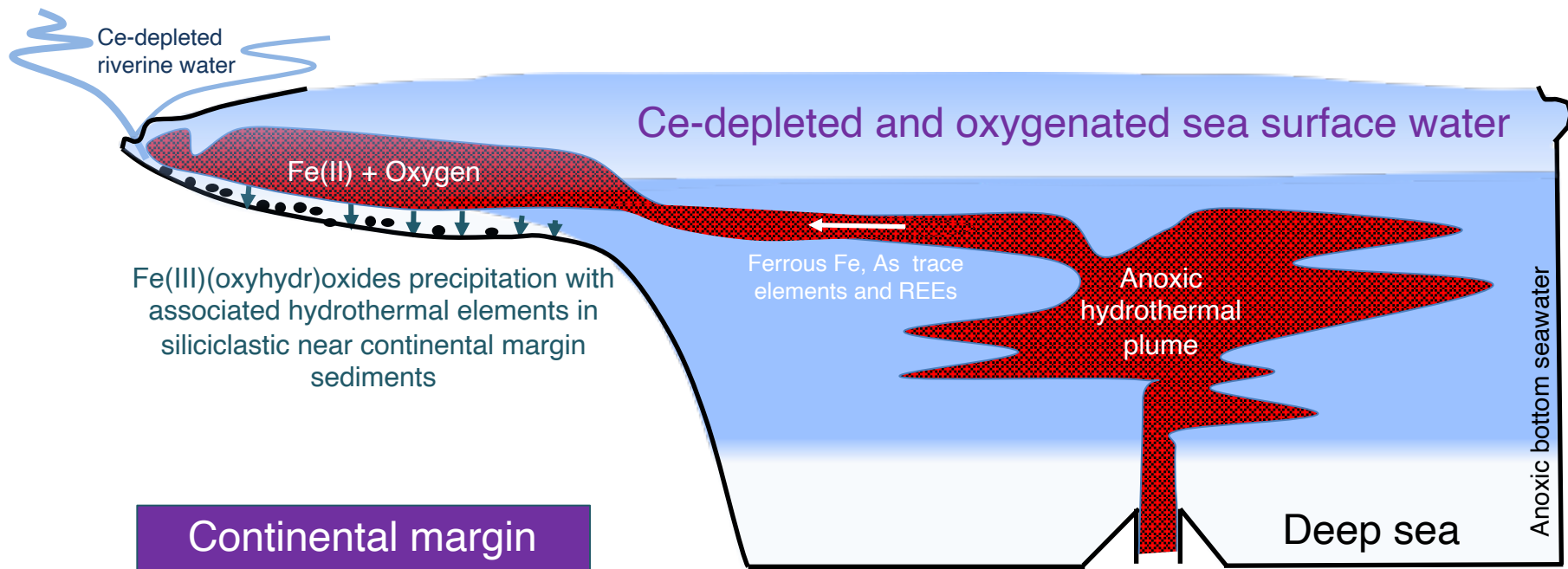












# Appendix

## Early Neoproterozoic oxygenation dynamics along the northern margin of the West African Craton, Anti-Atlas Mountains, Morocco

Ernest Chi Fru<sup>a\*</sup>, Olabode Bankole<sup>b</sup>, Ibtissam Chraiki<sup>c</sup>, Nassreddine Youbi<sup>c</sup>, Marc-Alban Millet<sup>a</sup>, Olivier Rouxel<sup>d</sup>, Abderrazzak El Albani<sup>b</sup>, El Hafid Bouougri <sup>c</sup>

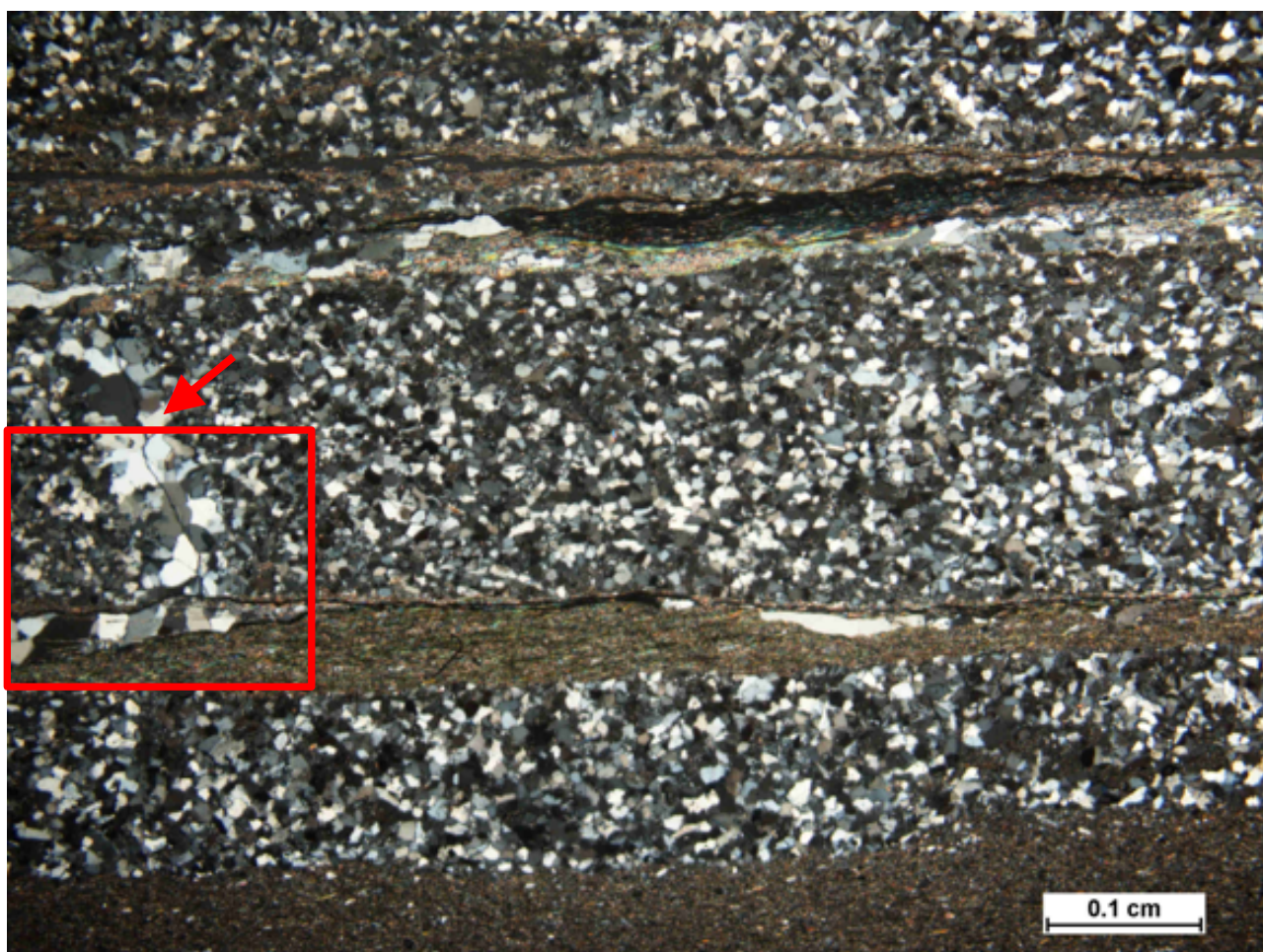
<sup>a</sup>School of Earth and Ocean Sciences, Centre for Geobiology and Geochemistry, Cardiff University, Cardiff CF10 3AT, Wales, UK

<sup>b</sup>University of Poitiers, CNRS IC2MP UMR 7285, Poitiers, France.

<sup>c</sup>DLGR, Department of Geology, Faculty of Sciences-Semlalia, Cadi Ayyad University, Marrakesh, Morocco.

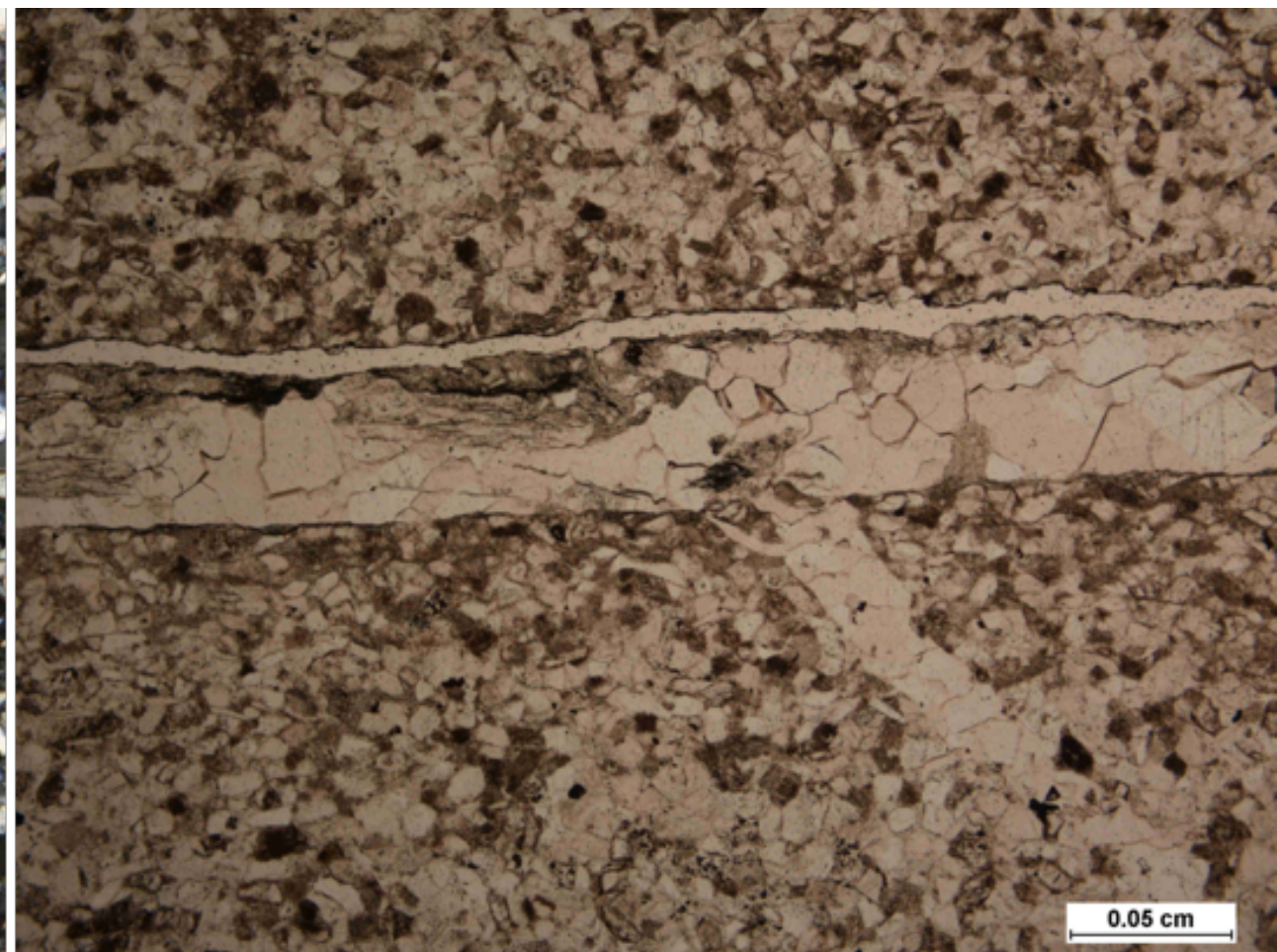
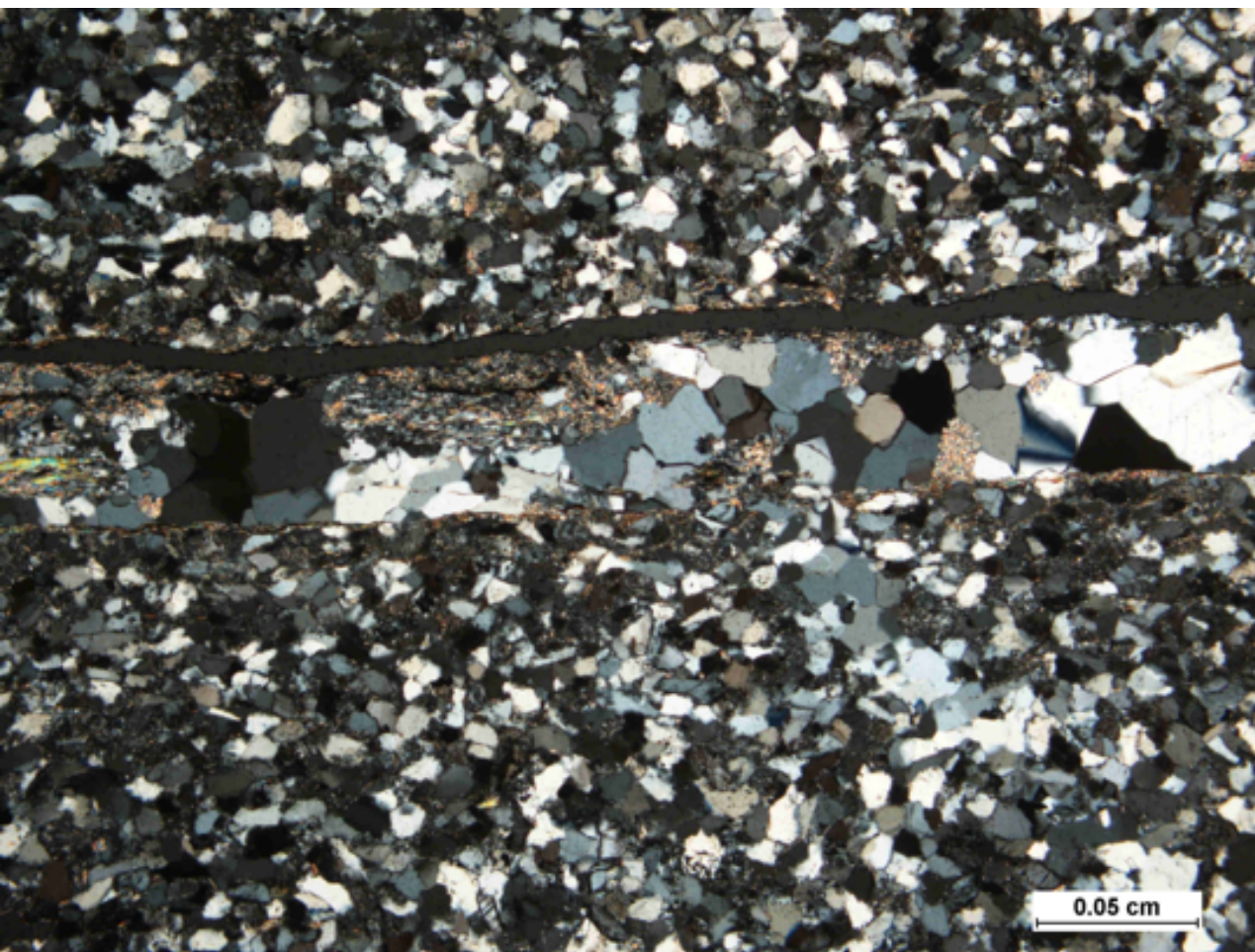
<sup>d</sup>Unité de Géosciences Marines, IFREMER, Z.I. Pointe du diable, BP 70, 29280 Plouzané, France.





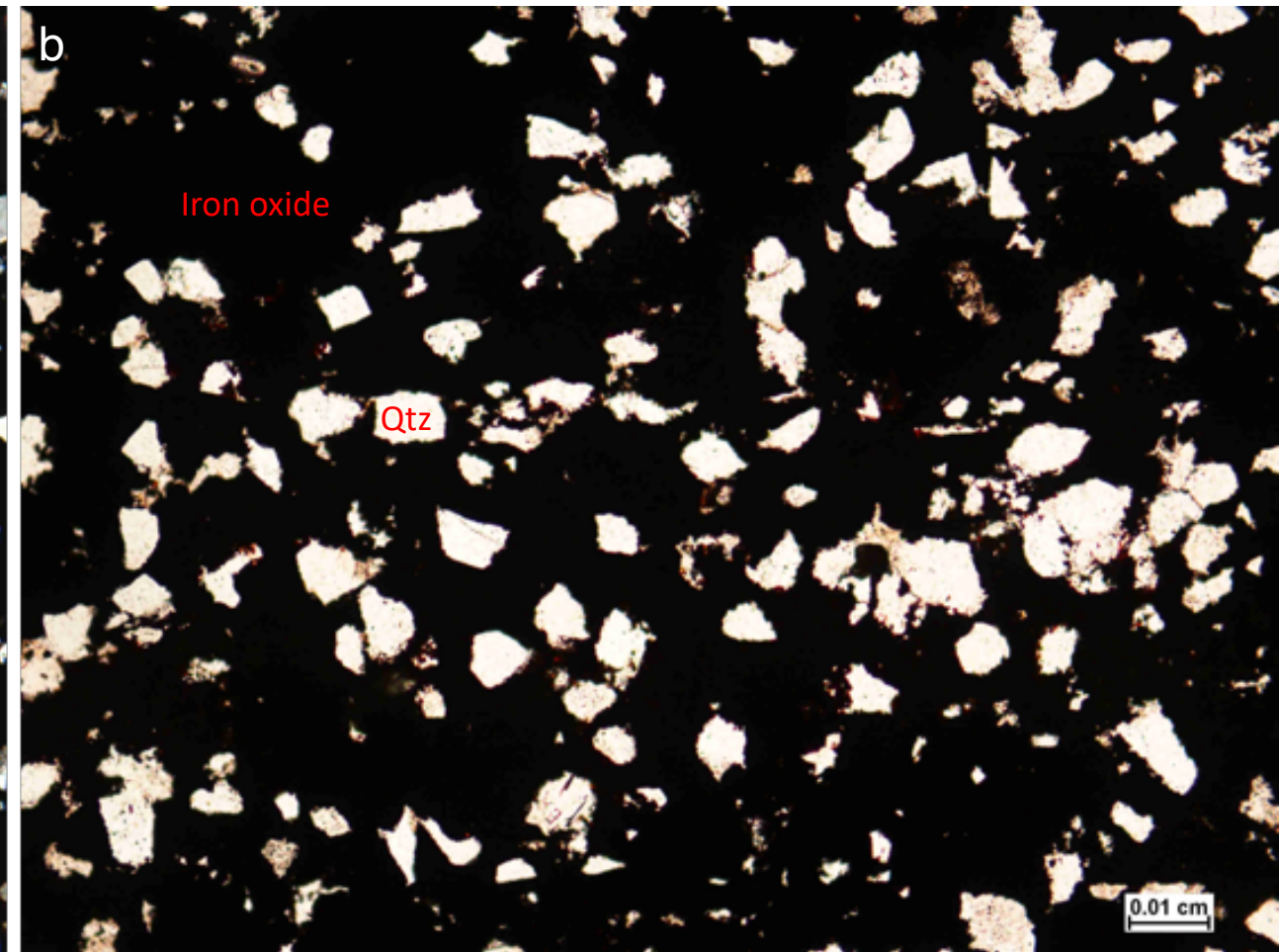
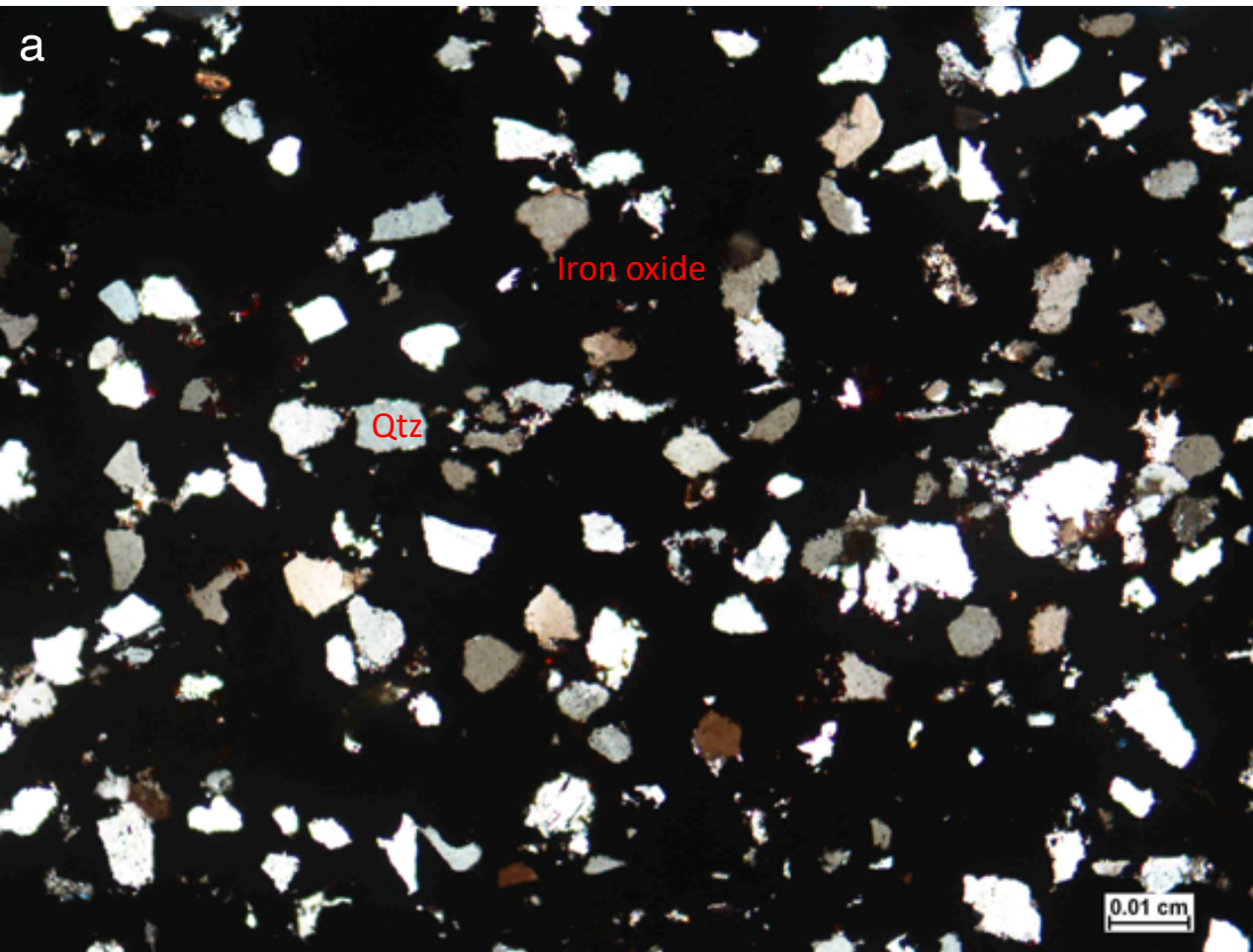
Appendix A. Microbially induced sedimentary structures of moderately compacted and well-sorted quartz-dominated silty-sandstone with alternating thin mud/shale laminae, consisting of micas (muscovite and illite). Thin sectioned cross polarized (a) and plain light (b) photographs showing the compositional layering of the flat top stromatolitic mats. The fluid nature of the fine-grained layer is suggested by leakages through cracks in the coarse-grained bed as indicated by the red arrows in panels a and b. The read box is enlarged in appendix B.





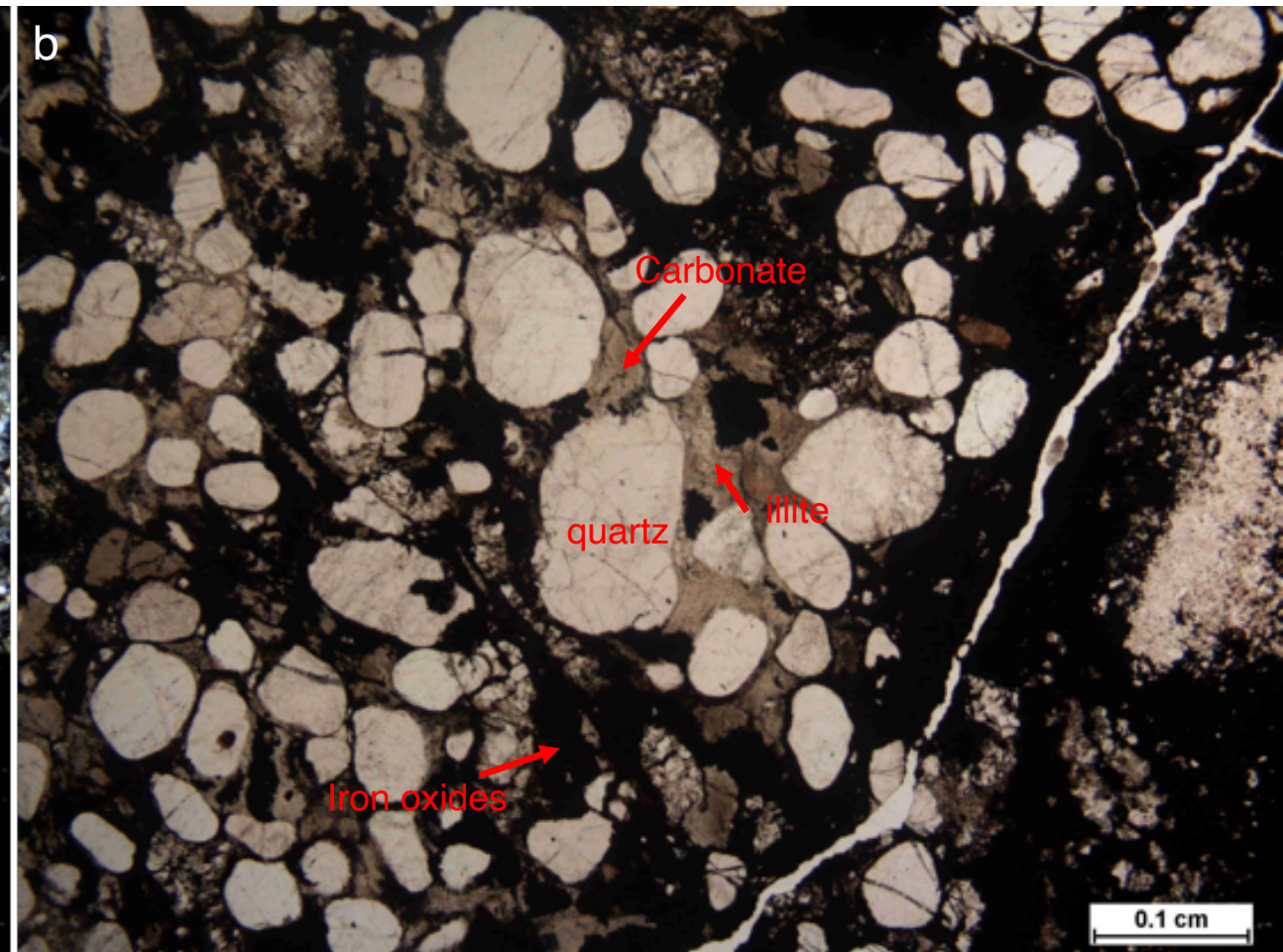
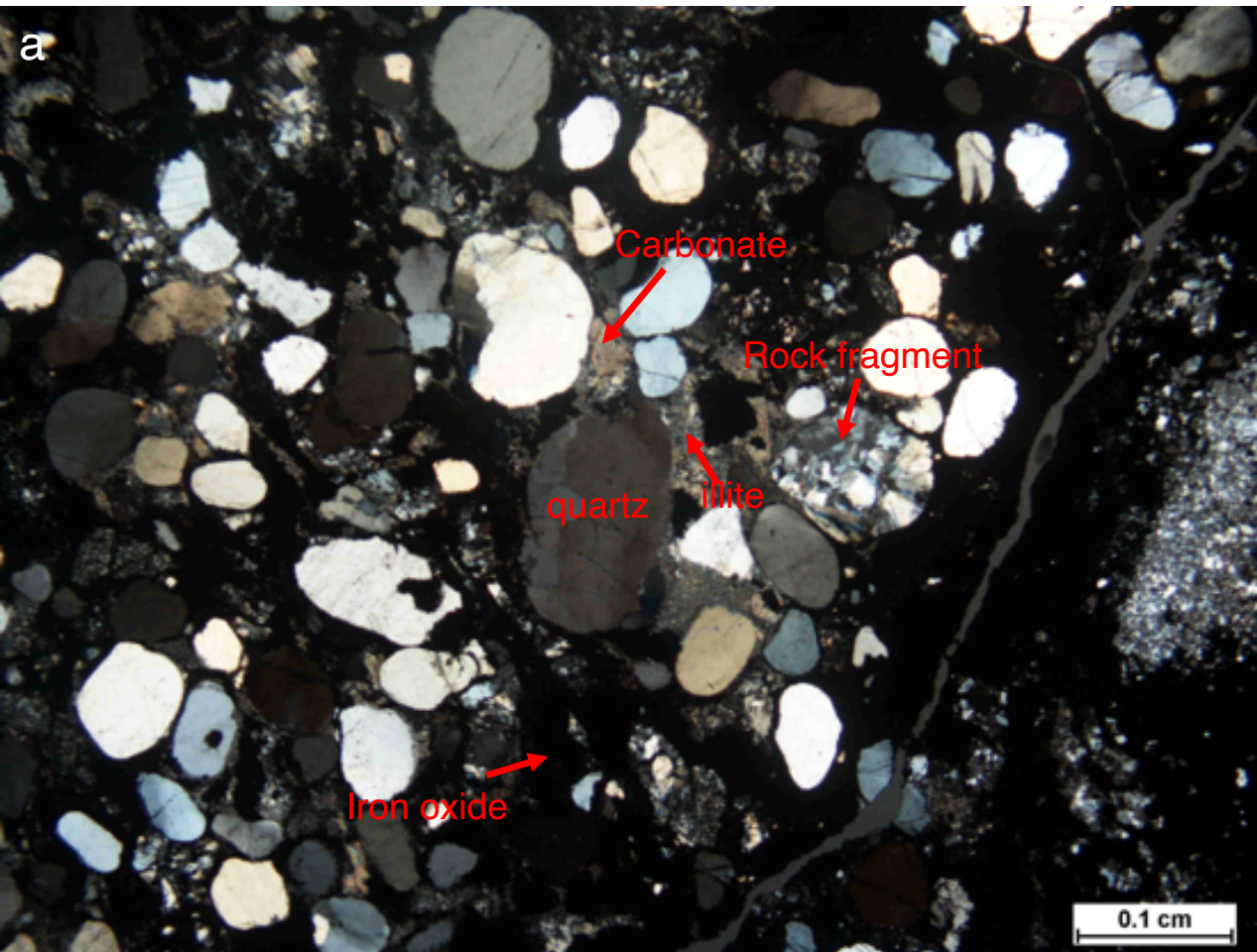
Appendix B. Enlarged red square in Appendix a, for thin sectioned cross polarized (a) and plain light (b) photographs showing the compositional layering of the flat top stromatolitic mats.





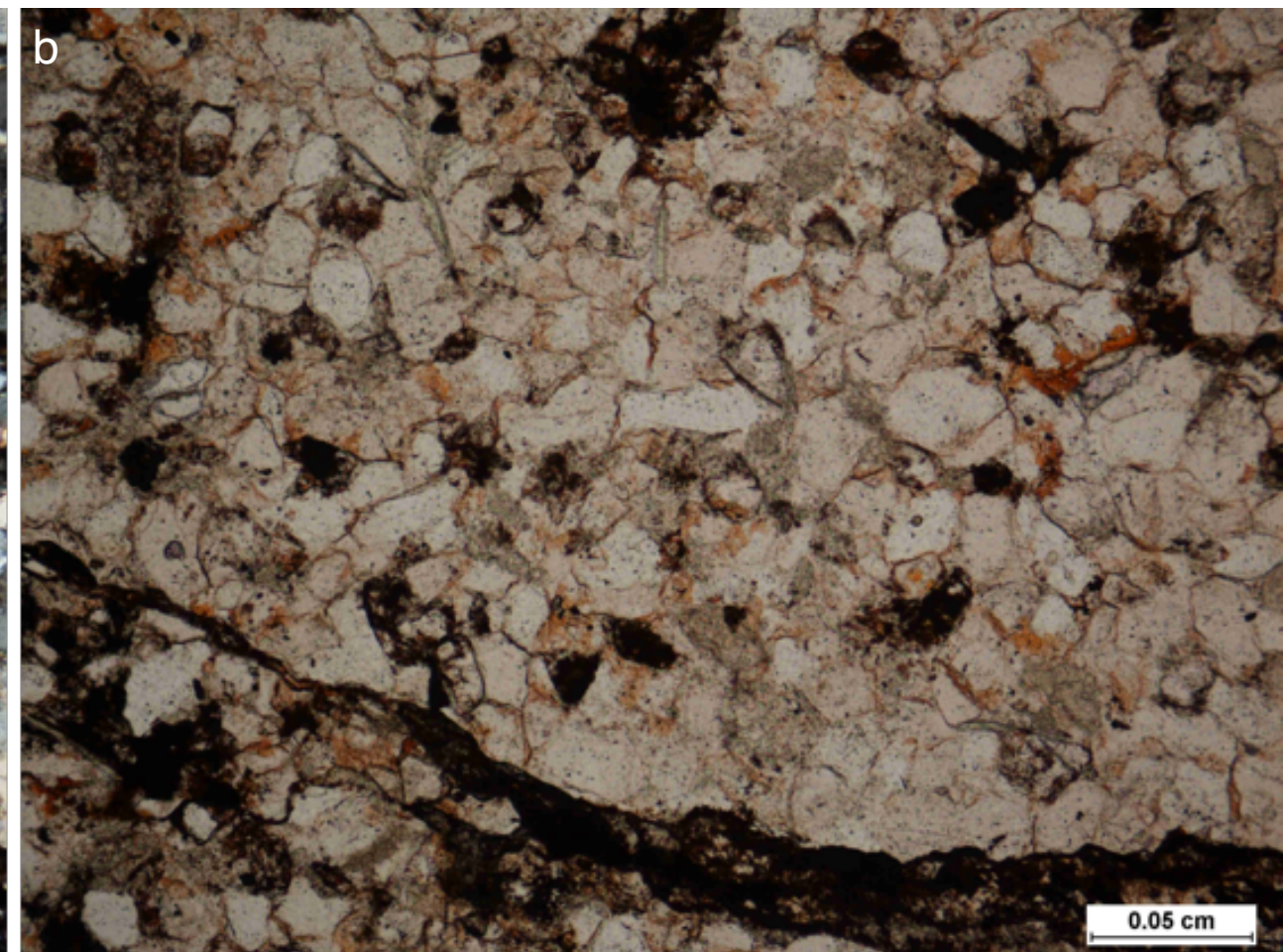
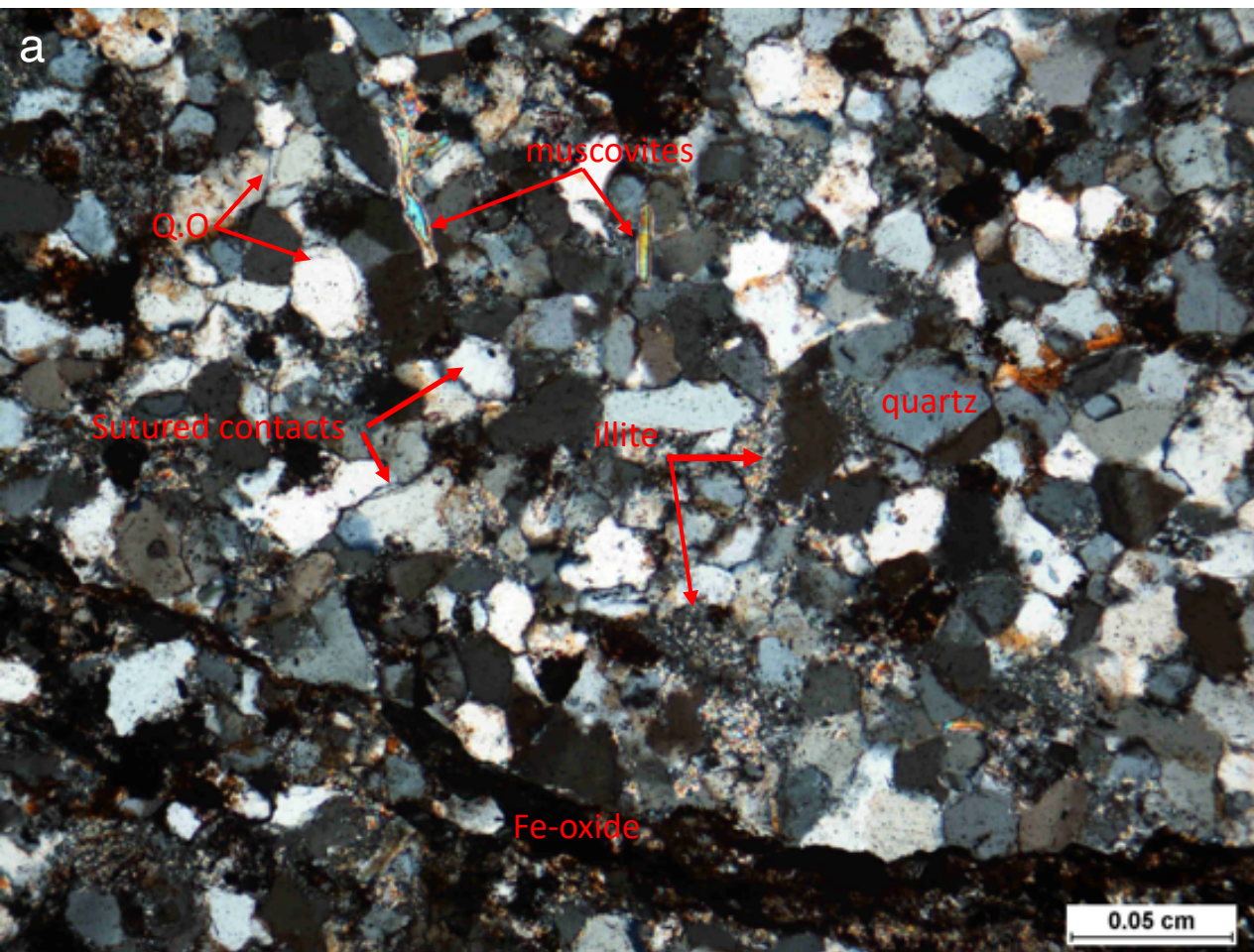
Appendix C. Thin sectioned cross polarized (a) and plain light (b) photographs for sample AG16 from the Wanimzi ironstone, showing well-sorted siltstones dominantly composed of sub-angular quartz clasts floating in an iron-oxide rich matrix (syn-depositional) in the Wanimzi Fe-rich deposit.





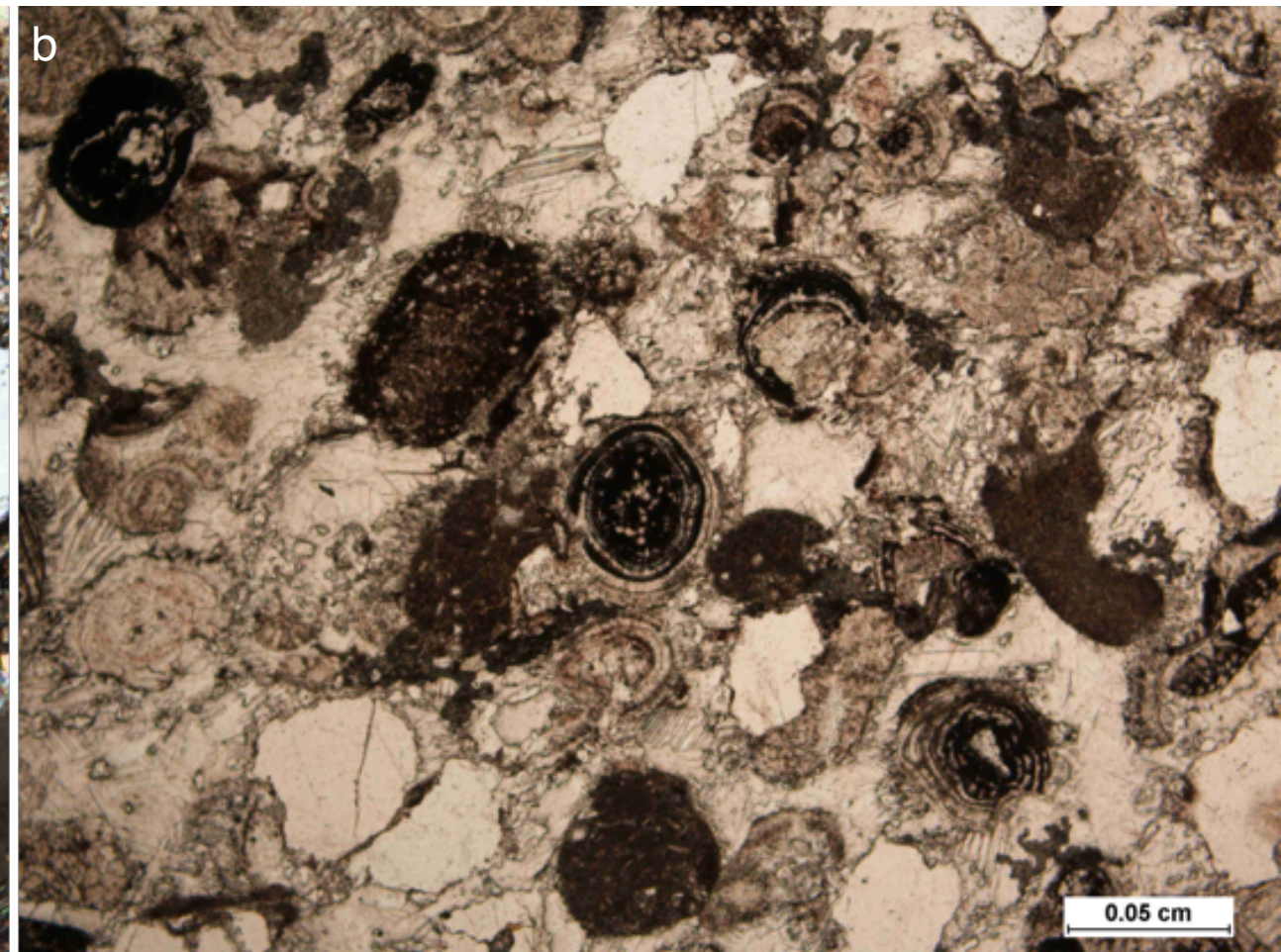
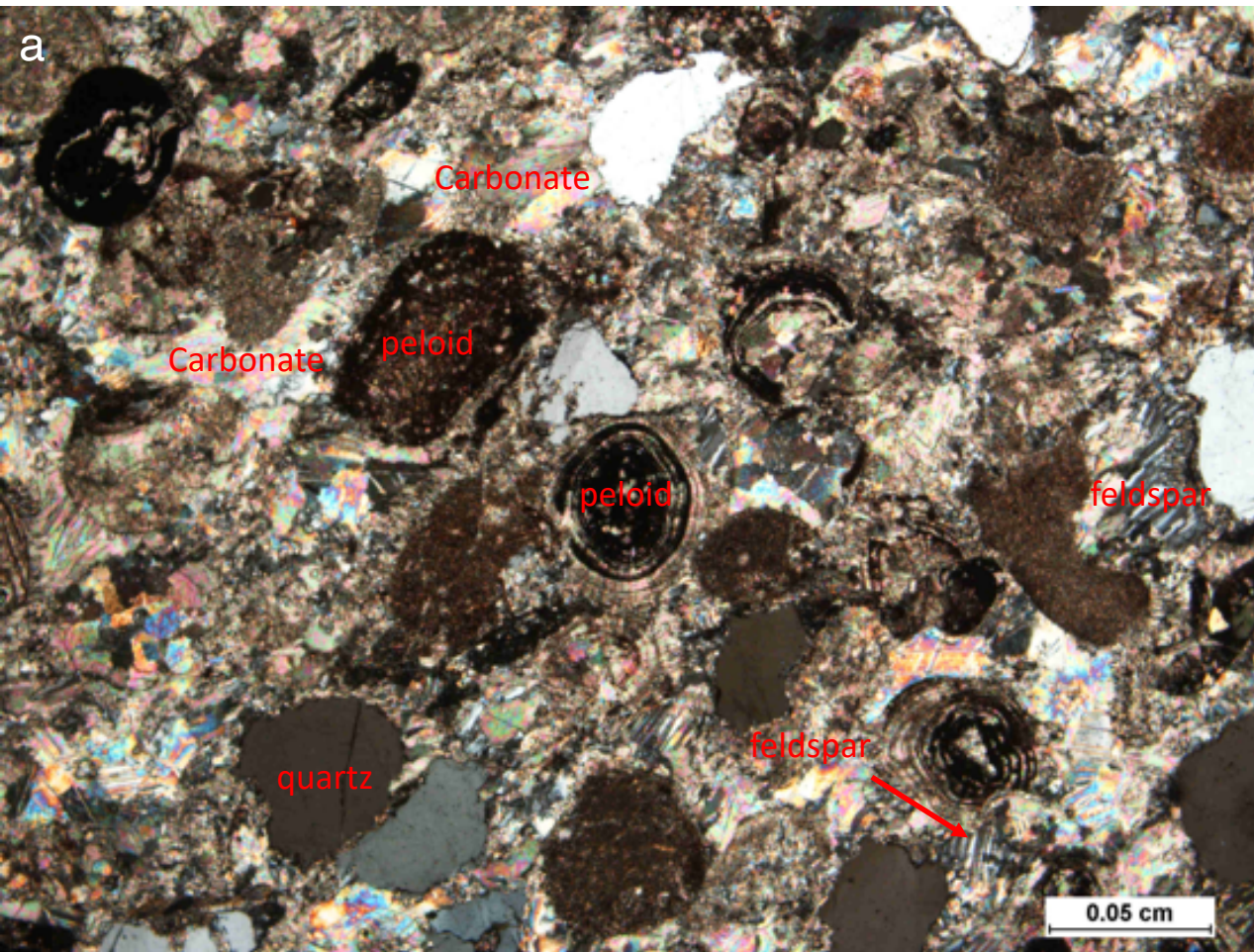
Appendix D. Thin sectioned cross polarized (a) and plain light (b) photographs for sample AG08 from the Wanimzi ironstone, showing poorly sorted coarse-grained sandstone consisting of rounded quartz grains surrounded by iron-oxide, illite, and carbonate cements





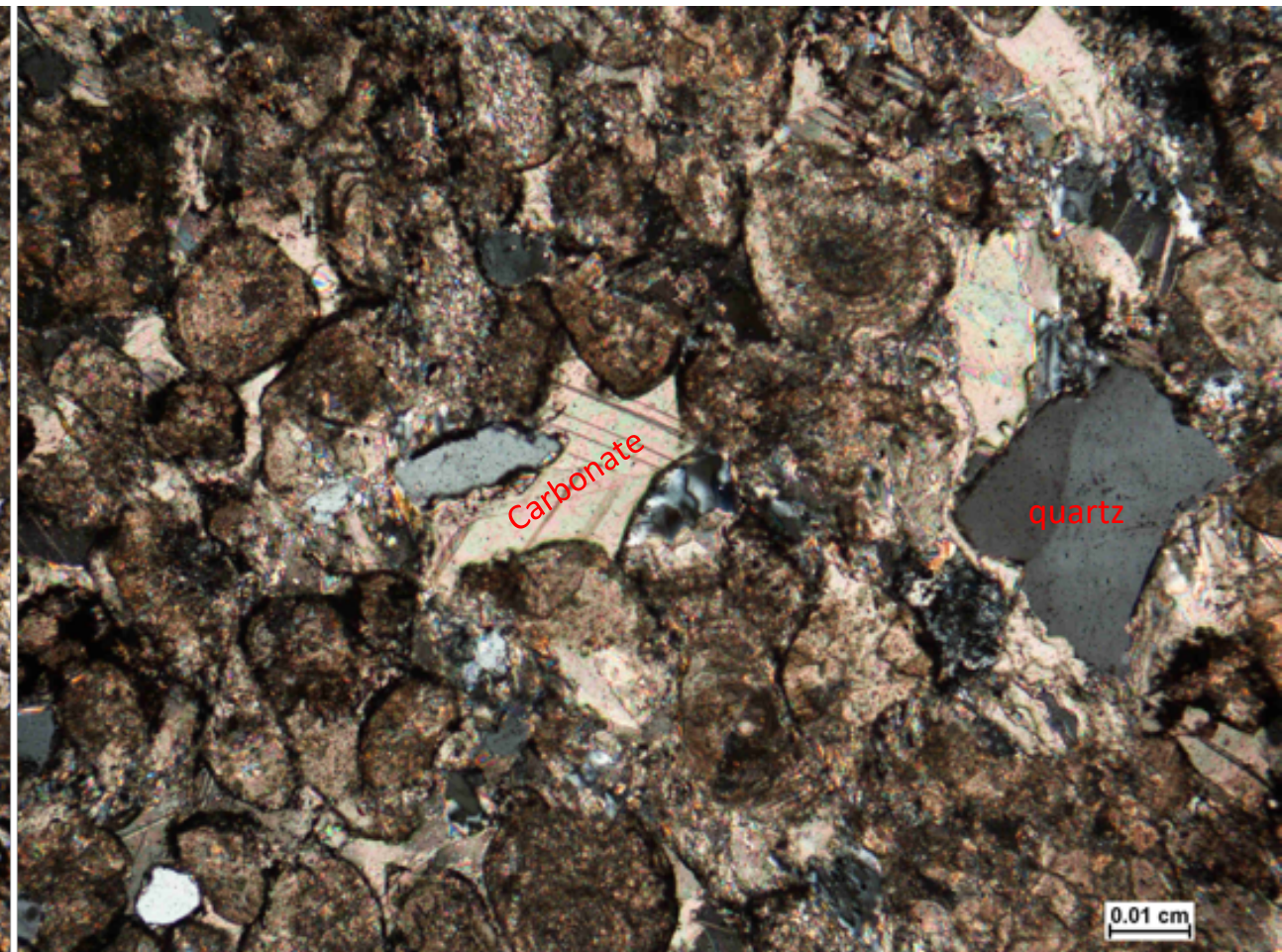
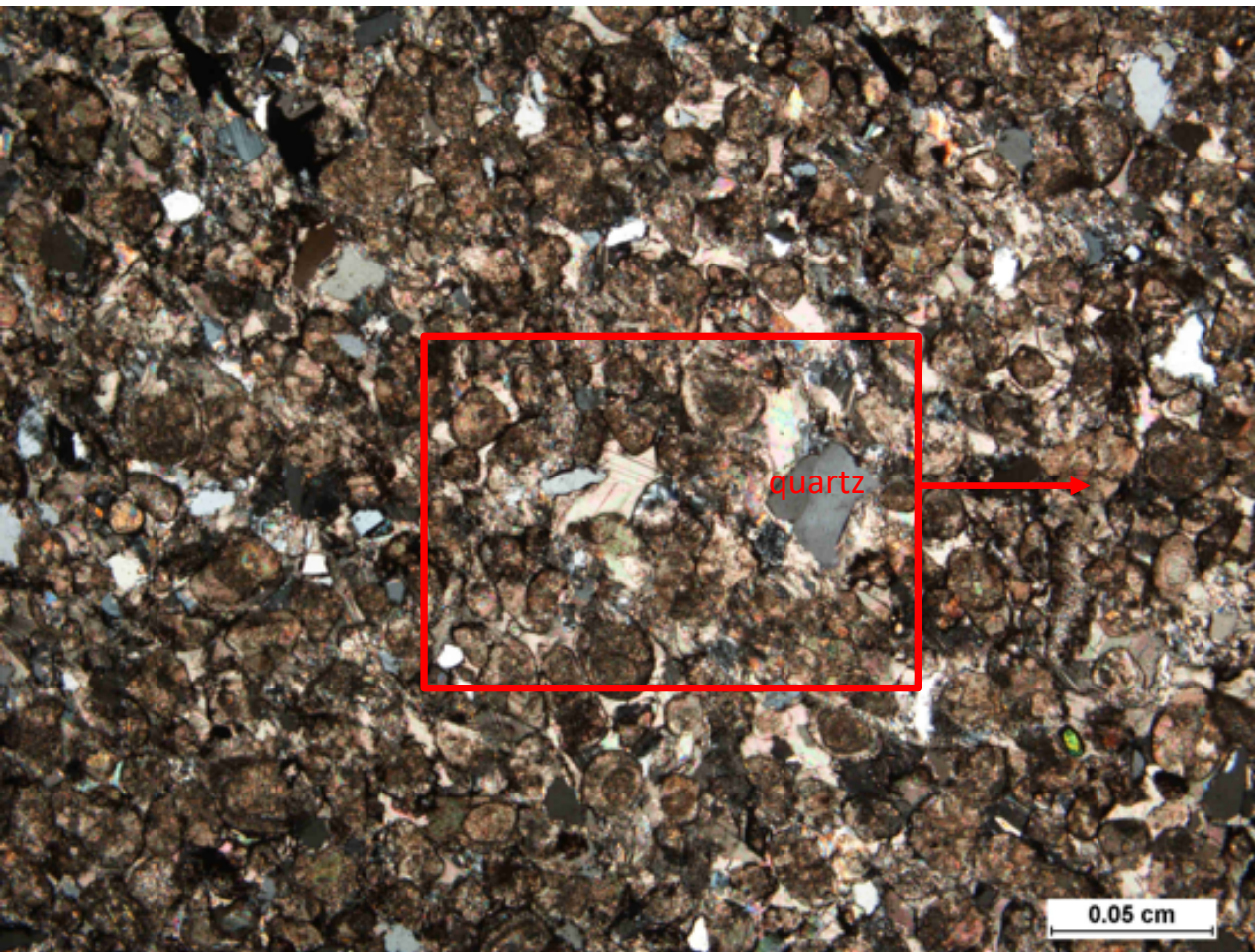
Appendix E. Moderately compacted silty sandstones dominated by moderately sorted angular to sub-angular detrital quartz grains (with sutured contacts) and mica flakes (mainly muscovites) in illite and iron-oxide cements for sample AG06 from the Wanimzi ironstone. Quartz overgrowths are observed in few instances. Thin sectioned cross polarized (a) and plain light (b) photographs, showing sutured clastic debris suggestive of Fe-rich cement. QO = quartz overgrowths





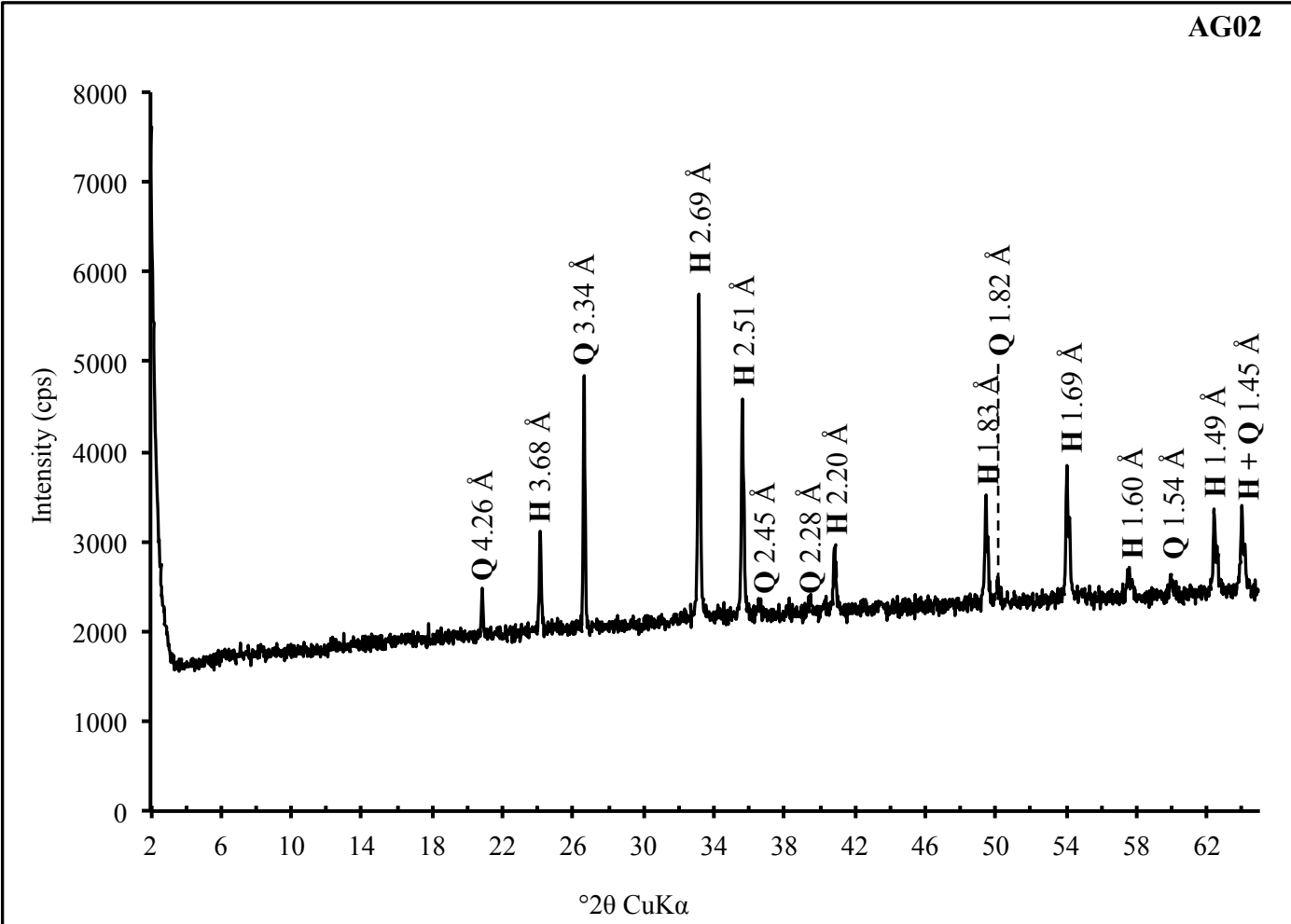
Appendix F. Thin sectioned cross polarized (a) and plain light (b) photographs for siliciclastic sample CA1 from the Tagdout Formation, showing rounded and ooidal clastic debris cemented in a carbonate-rich matrix. Peloids and microbially induced spherulite cemented in a calcite-rich matrix. Few quartz grains and altered feldspars are dispersed within the carbonate cement.





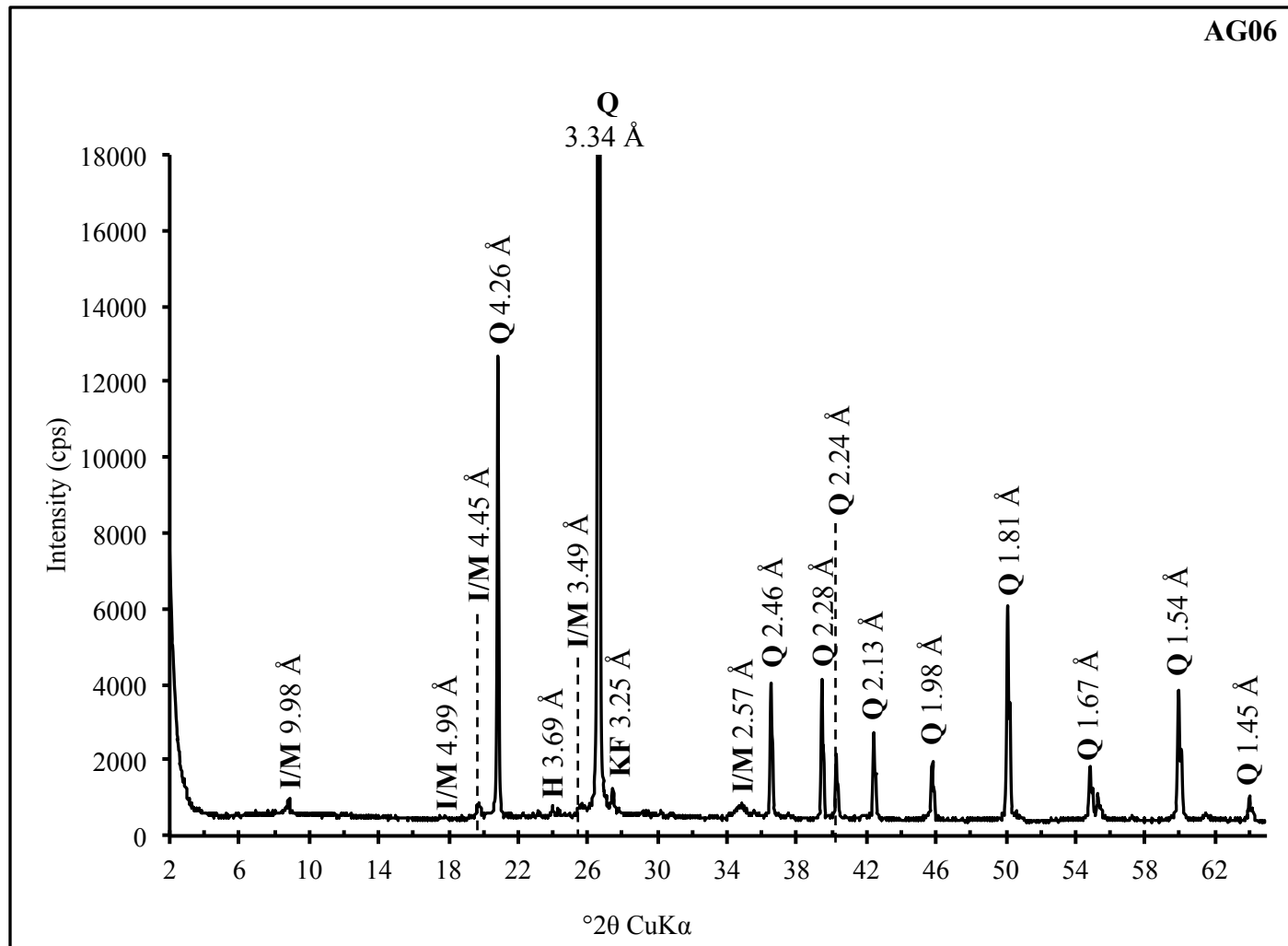
Appendix G. Thin sectioned cross polarized light (a) and plain light (b) photographs for siliciclastic carbonate sample CAB2 from the Taghdout Formation, showing peloidal clastic debris cemented in a carbonate-rich matrix





Keys:  
Q = quartz  
H = hematite

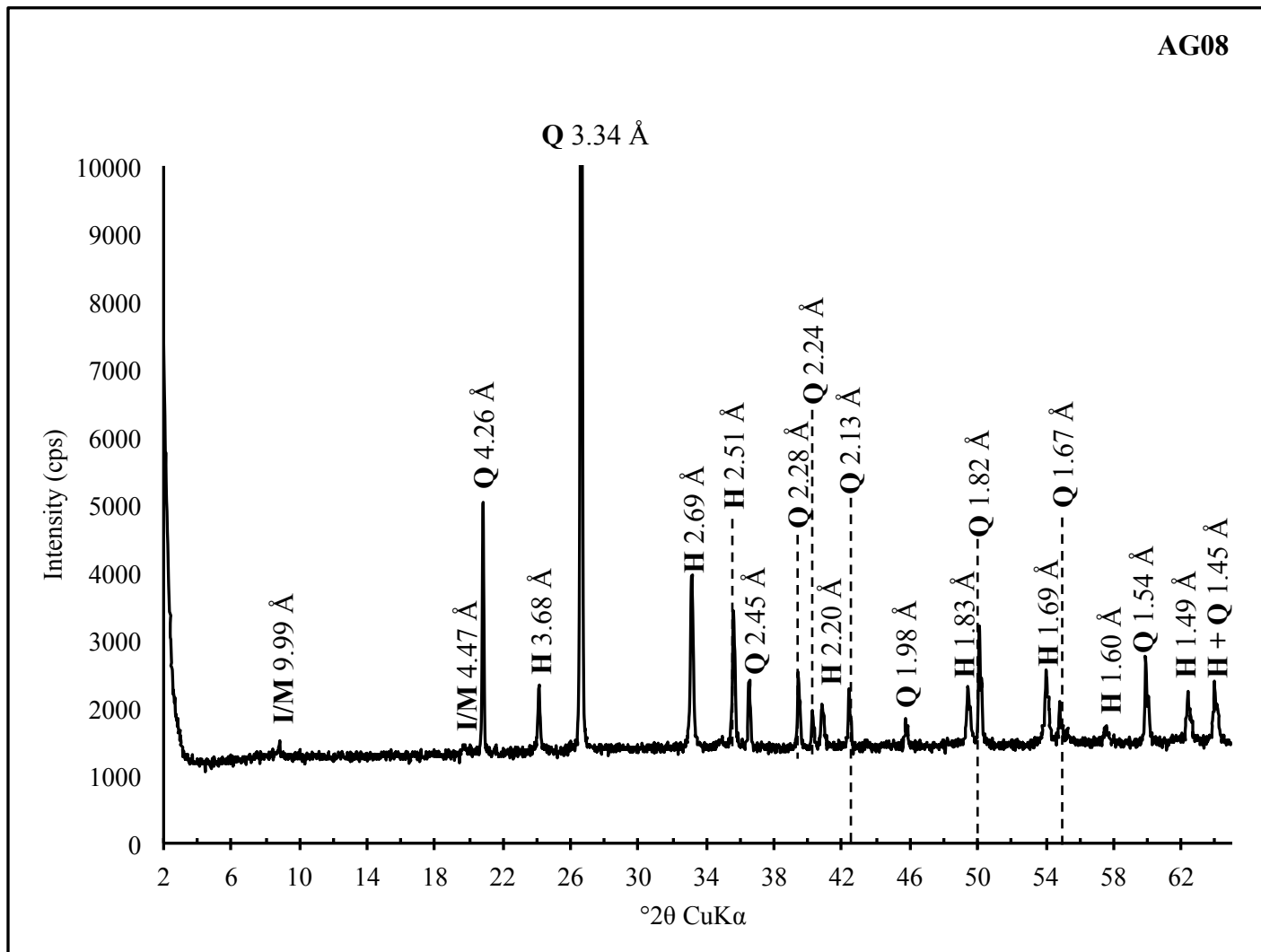
Appendix H. XRD mineralogical signal for sample AG02 from the Wanimzi ironstone



Keys:  
Q = quartz  
H = hematite  
I/M = illite/mica  
KF = K-feldspar

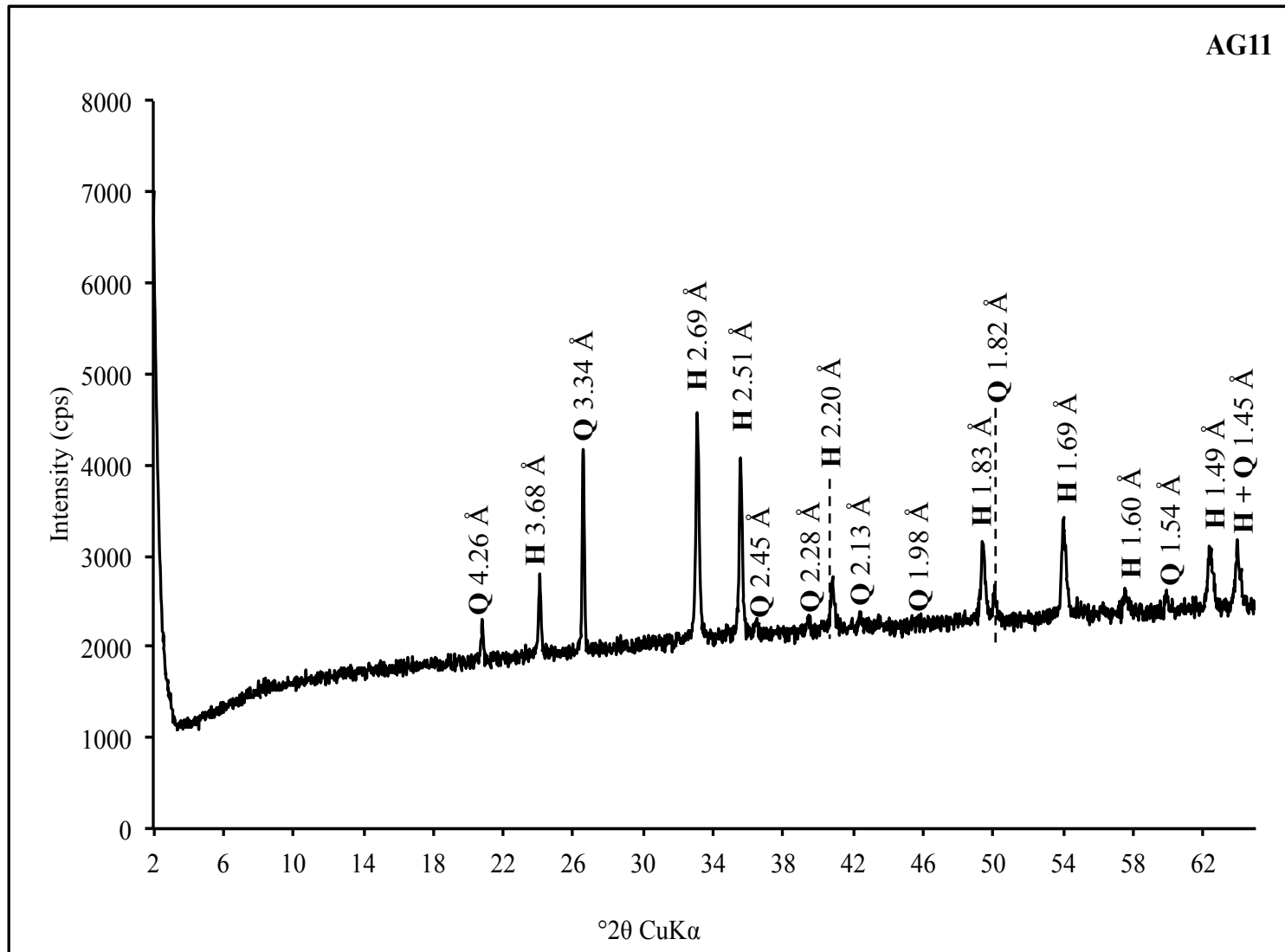
Appendix I. XRD mineralogical signal  
for sample AG06 from the Wanimzi  
ironstone





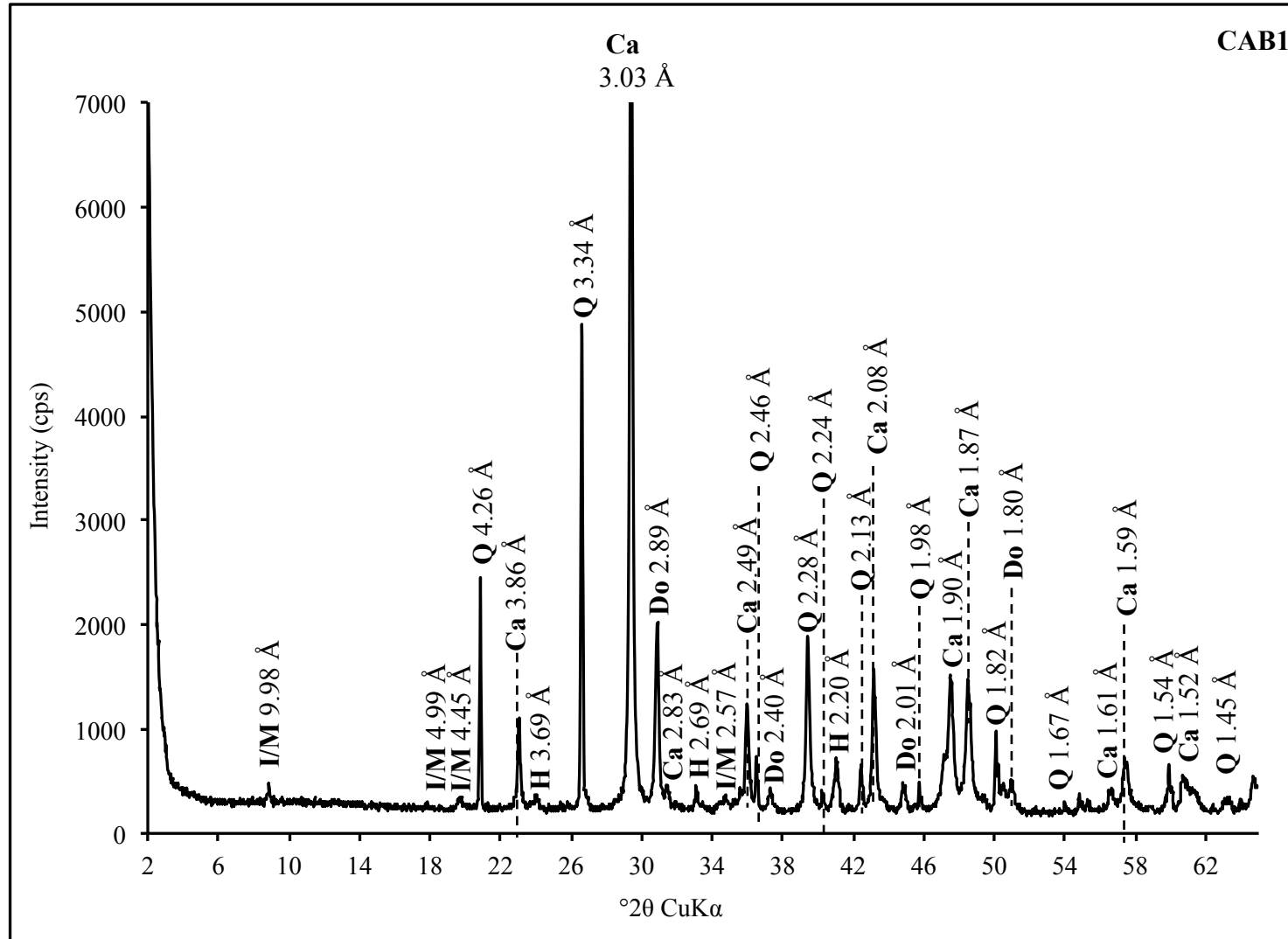
Keys:  
Q = quartz  
H = hematite  
I/M = illite/mica

Appendix J. XRD mineralogical signal for sample AG08 from the Wanimzi ironstone



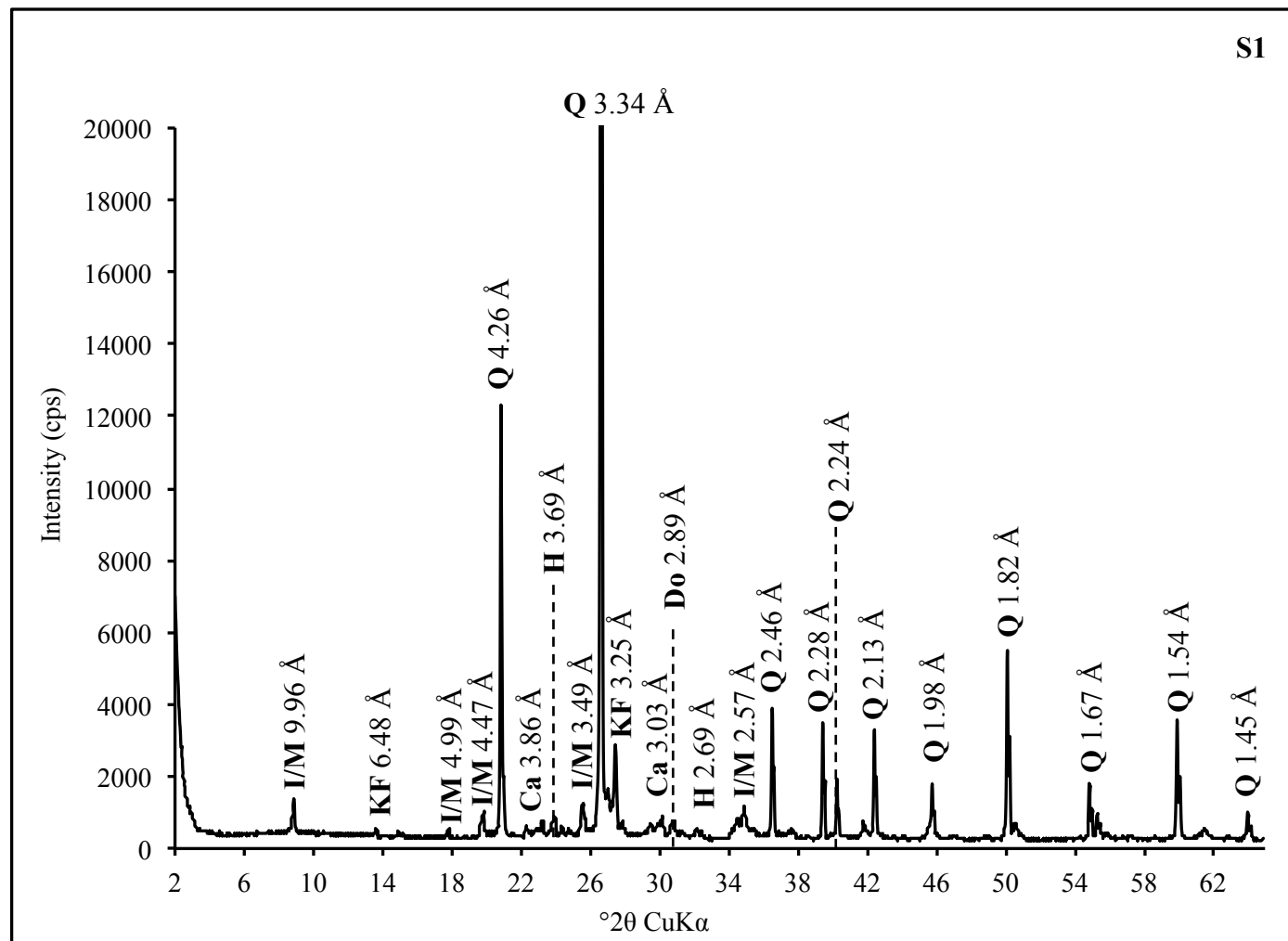
Keys:  
Q = quartz  
H = hematite

Appendix K. XRD mineralogical signal for sample AG11 from the Wanimzi ironstone



Keys:  
Q = quartz  
H = hematite  
I/M = illite/mica  
Ca = calcite  
Do = dolomite

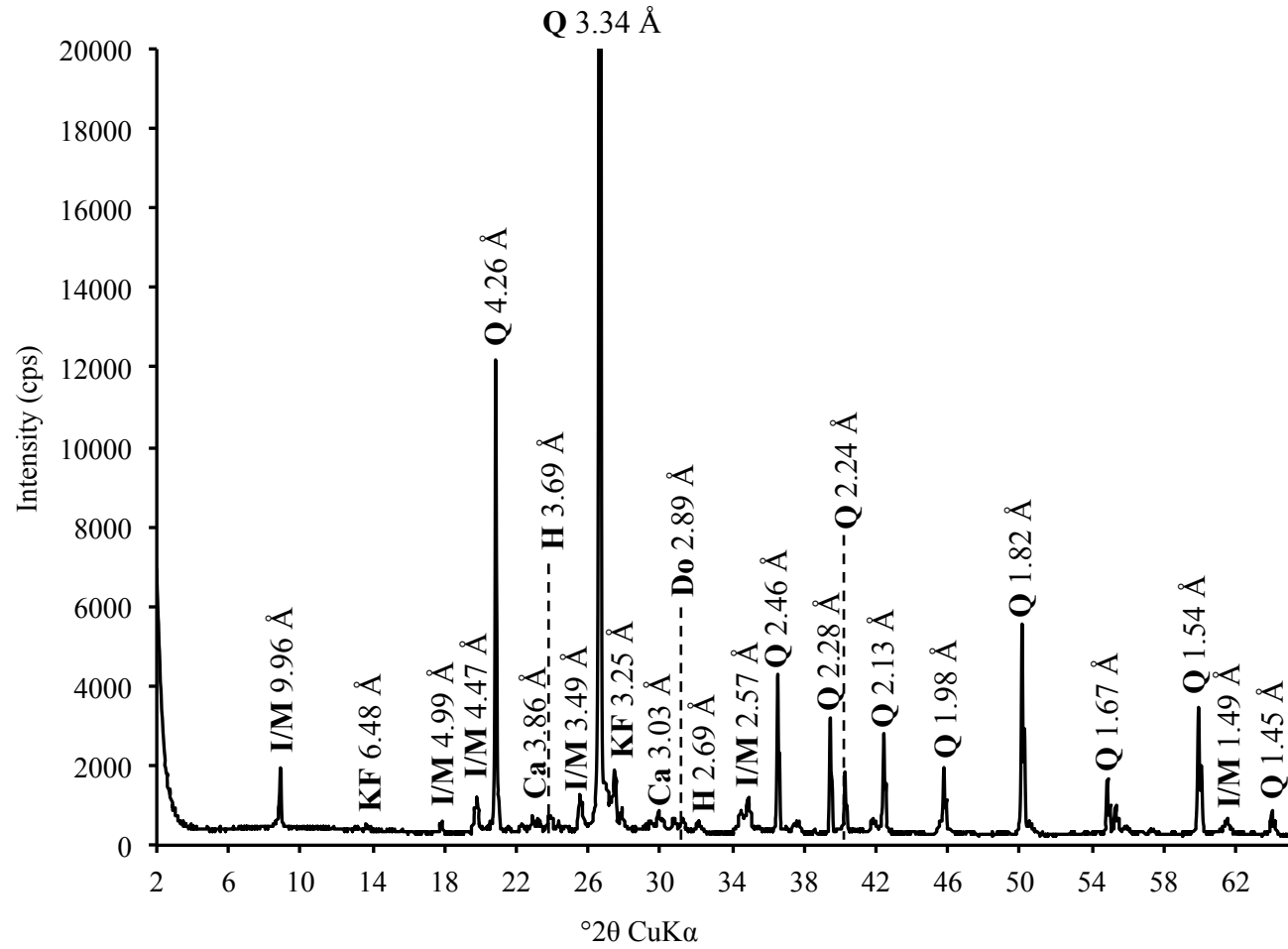
Appendix L. XRD mineralogical signal for sample CAB1 from the Taghdout siliclastic carbonates



Keys:  
Q = quartz  
H = hematite  
I/M = illite/mica  
Ca = calcite  
Do = dolomite  
KF = K-feldspar

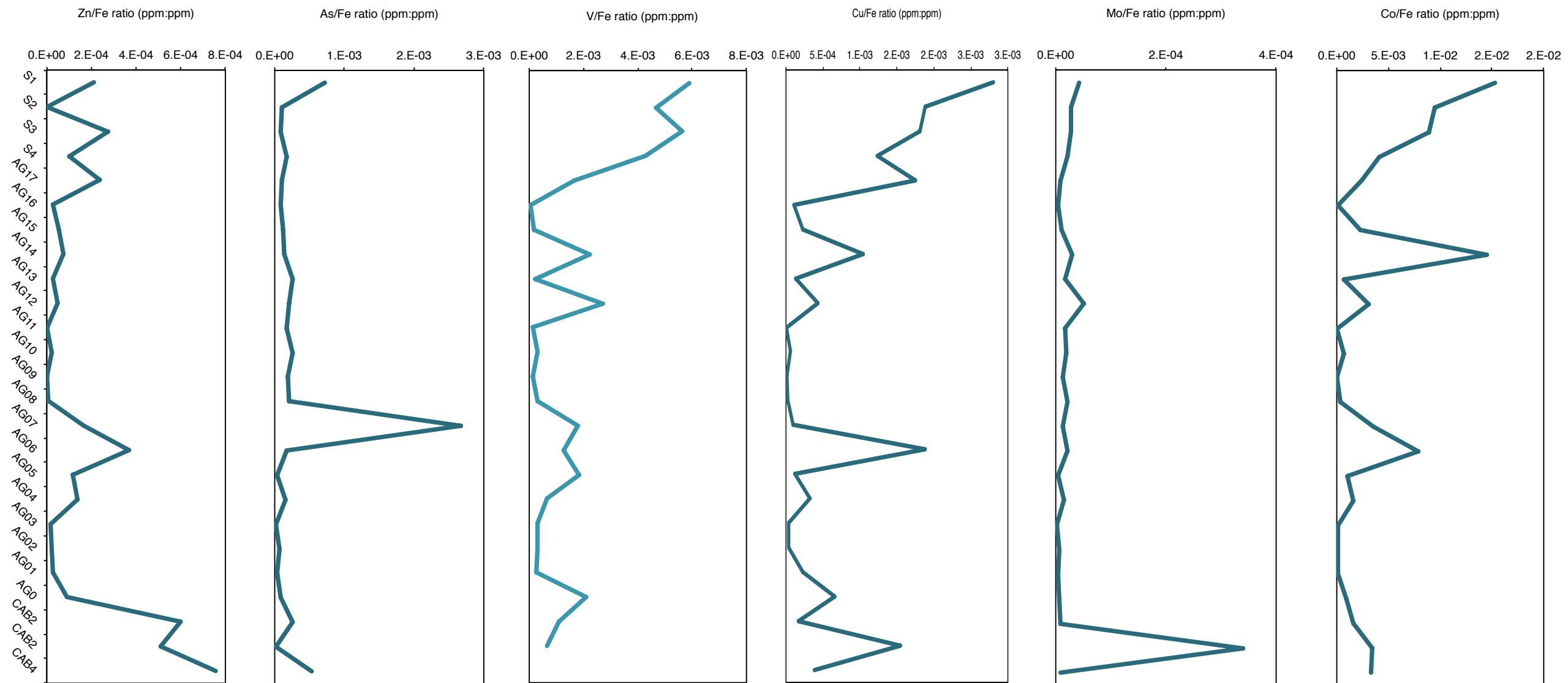
Appendix M. XRD mineralogical signal for sample S1  
from the siliciclastic stromatolites

S2

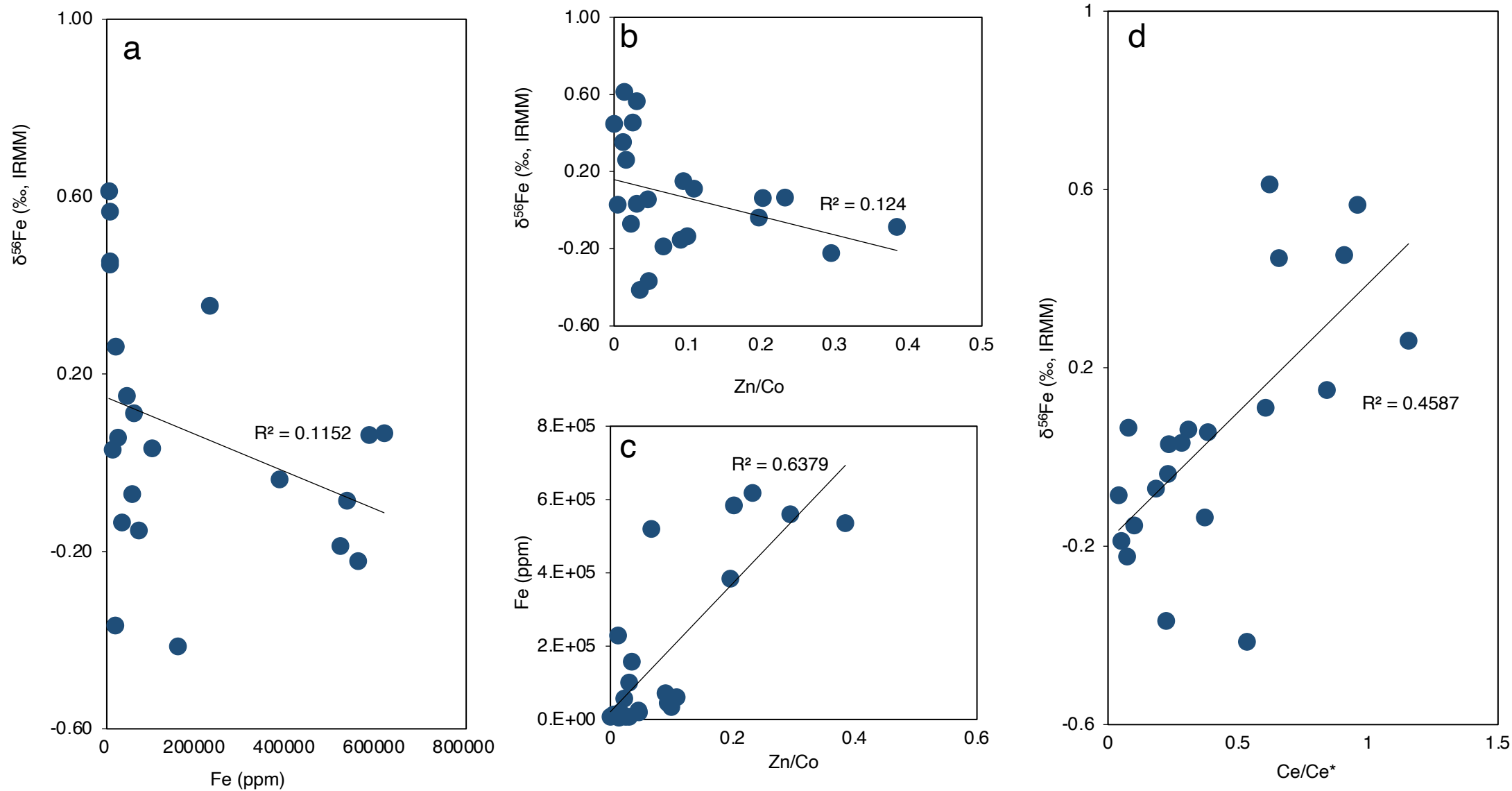


Keys:  
 Q = quartz  
 H = hematite  
 I/M = illite/mica  
 Ca = calcite  
 Do = dolomite  
 KF = K-feldspar

Appendix N. XRD mineralogical signal for sample S2 from the siliciclastic stromatolites



Appendix O. Concentrations of Zn, As, V, Cu, Mo and Cu normalized to Fe concentrations across the sampled succession



Appendix P. Cross plots between (a) Fe and  $\delta^{56}\text{Fe}$ , (b)  $\delta^{56}\text{Fe}$  and Zn/Co ratios, (c) Fe and Zn/Co and (d)  $\delta^{56}\text{Fe}$  and Ce/Ce'